

– For internal NASA use only –

---

# Lunar Meteoroid Ejecta Engineering Model

---

*Anthony M. DeStefano*  
NASA MSFC EV44

August 30, 2022

## Contents

<b>1 Executive Summary</b>	<b>1</b>
<b>2 Lunar Regolith Properties</b>	<b>2</b>
2.1 Porosity . . . . .	2
2.2 Density . . . . .	2
2.3 Strength . . . . .	5
2.4 Particle Size Distribution . . . . .	7
<b>3 Primary Flux Environment</b>	<b>11</b>
3.1 Space-Time Dependence of Environment . . . . .	11
3.1.1 Ephemeris Definition . . . . .	11
3.2 Sporadic Meteoroid Complex . . . . .	13
3.2.1 Angular Distribution . . . . .	13
3.2.2 Density Distribution . . . . .	18
3.2.3 Mass Distribution . . . . .	20
3.3 Near-Earth Objects . . . . .	20
3.3.1 Speed Distribution . . . . .	21
3.3.2 Mass Distribution . . . . .	21
3.4 Meteoroid Showers . . . . .	22
<b>4 Ejecta Flux from Impact Point</b>	<b>23</b>
4.1 Ejecta Distribution . . . . .	23
4.1.1 Speed Distribution . . . . .	23
4.1.2 Zenith Distribution . . . . .	23
4.1.2.1 Peak Zenith Angle $\alpha_{max}$ . . . . .	23
4.1.2.2 Rival & Mandeville (Gaussian Distribution) . . . . .	24
4.1.2.3 Raised Cosine Distribution . . . . .	25
4.1.3 Azimuth Distribution . . . . .	25

4.1.3.1	Rival & Mandeville . . . . .	25
4.1.3.2	Variation on Rival & Mandeville . . . . .	25
4.2	Mass/Particle Size Distribution . . . . .	26
4.2.1	NASA SP-8013 . . . . .	26
4.2.2	O'Keefe & Ahrens 1985 . . . . .	27
4.2.3	Mass Distribution with Speed Distribution Weighting . . . . .	29
4.3	Total Kinetic Energy . . . . .	30
4.4	Orbital Mechanics . . . . .	33
4.4.1	Crater on Surface to Asset at Surface . . . . .	34
4.4.1.1	Distance $D$ vs. $v_p$ and $\gamma_p$ . . . . .	34
4.4.1.2	Initial Speed $v_p$ vs. $D$ and $\gamma_p$ . . . . .	35
4.4.1.3	Initial Zenith Angle $\gamma_p$ vs. $D$ and $v_p$ . . . . .	35
4.4.1.4	Minimum Initial Zenith Angle $\gamma_{p,min}$ vs. $D$ . . . . .	35
4.4.1.5	Maximum Distance $D_{max}$ vs. $v_p$ . . . . .	35
4.4.1.6	Minimum Initial Speed $v_{p,min}$ vs. $D$ . . . . .	36
4.4.1.7	Optimal Initial Zenith Angle $\gamma_{p,opt}$ vs. $D$ . . . . .	36
4.4.1.8	Final Speed $v_s$ and Zenith Angle $\gamma_s$ . . . . .	36
4.4.1.9	Visualizing Ejecta in Phase Space . . . . .	37
4.4.2	Crater on Surface to Asset at or above Surface . . . . .	41
4.4.2.1	Maximum Radial Distance $r_{max}$ vs. $v_p$ and $\gamma_p$ . . . . .	41
4.4.2.2	Minimum Initial Speed $v_{p,min}$ vs. $\gamma_p$ and $r_s$ . . . . .	42
4.4.2.3	Initial Zenith Angle to reach Apoapsis $\gamma_{p,ap}$ vs. $v_p$ and $r_s$ . . . . .	42
4.4.2.4	Initial Zenith Angle to reach Apoapsis $\gamma_{p,ap}$ vs. $D$ and $r_s$ . . . . .	42
4.4.2.5	Initial Speed $v_p$ vs. $D$ , $\gamma_p$ , and $r_s$ . . . . .	42
4.4.2.6	Distance $D$ vs. $v_p$ , $\gamma_p$ , and $r_s$ . . . . .	43
4.4.2.7	Initial Zenith Angle $\gamma_p$ vs. $D$ , $v_p$ , and $r_s$ . . . . .	43
4.4.2.8	Minimum Initial Zenith Angle $\gamma_{p,min}$ vs. $D$ and $r_s$ . . . . .	44
4.4.2.9	Maximum Distance $D_{max}$ vs. $v_p$ and $r_s$ . . . . .	44
4.4.2.10	Minimum Initial Speed $v_{p,min}$ vs. $D$ and $r_s$ . . . . .	44
4.4.2.11	Optimal Initial Zenith Angle $\gamma_{p,opt}$ vs. $D$ and $r_s$ . . . . .	45
4.4.2.12	Final Speed $v_s$ vs. $v_p$ and $r_s$ . . . . .	45
4.4.2.13	Final Zenith Angle $\gamma_s$ vs. $v_p$ , $\gamma_p$ , and $r_s$ . . . . .	45
4.4.2.14	Final Radial Distance $r_s$ vs. $D$ , $v_p$ , and $\gamma_p$ . . . . .	45
4.4.2.15	Visualizing Ejecta in Phase Space . . . . .	46
4.5	Azimuthal Field-of-View . . . . .	54
4.5.1	Maximum Azimuthal FOV . . . . .	54
4.5.2	Effective Cylindrical Diameter . . . . .	54
4.5.3	Effective Crater-to-Asset Distance . . . . .	55
4.6	Selenographic Distance & Bearing . . . . .	57
4.7	Coriolis Force . . . . .	58
<b>5</b>	<b>Scaling Laws</b> . . . . .	<b>58</b>
5.1	Crater Size – Strength & Gravity Regime . . . . .	59
5.2	Mass Ejected from Crater . . . . .	59
5.2.1	Ejected Mass Distribution . . . . .	61
5.3	Scaling Law Parameters . . . . .	62

<b>6 Numerical Methods</b>	<b>63</b>
6.1 Asset Collision Algorithm . . . . .	63
6.2 Ejecta Speed-Zenith-Azimuth Sampling Algorithm . . . . .	68
6.2.1 Approximating Ejected Mass Fraction . . . . .	68
<b>7 Secondary Environment at Asset</b>	<b>69</b>
7.1 Numerical Results . . . . .	69
7.1.1 Latitude-Longitude Dependence . . . . .	69
7.1.2 Speed Distribution . . . . .	69
7.1.3 Angular Distribution . . . . .	69
7.1.4 Ejecta Size Distribution . . . . .	69
7.2 Analytical Results . . . . .	69
7.3 Benchmark Verification . . . . .	69
<b>References</b>	<b>70</b>

## List of Figures

1 A comparison of the regolith bulk density for a certain depth (blue), the depth-averaged bulk density (orange), and the volume-averaged bulk density (green). See also, Figure 9.16 of the Lunar Sourcebook [Heiken <i>et al.</i> , 1991]. . . . .	3
2 Relative error of using the density at a certain depth (blue) and using the depth-weighted average (orange) of the regolith bulk density. . . . .	5
3 The range of regolith shear strength as a function of depth below the lunar surface taken from Figure 9.26 of the Lunar Sourcebook. The average shear strength is also calculated (green). Dashed lines indicate extrapolated points beyond available data. The volume-averaged shear strength (red) assumes a parabolic-shaped crater of depth $z$ . . . . .	6
4 Geotechnical particle size distribution: middle curve showing the average distribution; left-hand and right-hand curves showing $\pm 1$ standard deviation [Carrier <i>III</i> , 2003]. Note, that the percent passing is normalized by mass and not particle number [see Carrier, 1973]. . . . .	7
5 Plots of the mass-weighted and number-weighted CDFs and PDFs derived from Carrier <i>III</i> [2003]. Top left: the digitized data from Figure 1 of Carrier <i>III</i> [2003] is shown with the log-normal distribution fit. Top right: The mass-weighted PDF $* dx$ is shown to indicate what particle size dominates the contribution of mass. Bottom left: The number-weighted CDF showing number of particles in 1 kg of regolith greater than a size $x$ . Bottom right: The number-weighted PDF is shown in units of $\text{mm}^{-1}$ . . . . .	9
6 Fluxes at the meridional plane (as a function of impact speed and angle from the horizon) of the low density population (a) and (b), and the high density population (c) and (d) impacting the Moon at the equator (a) and (c), and the north/south pole (b) and (d). . . . .	14

7	Fluxes at the meridional plane as a function of approaching angle for the low density population (a) and (b), and the high density population (c) and (d) impacting the Moon at the south pole in a Mollweide (a) and (c), and all-sky (b) and (d) projection. . . . .	15
8	Fluxes at the meridional plane as a function of approaching angle for the low density population (a) and (b), and the high density population (c) and (d) impacting the Moon at $-45^\circ$ latitude in a Mollweide (a) and (c), and all-sky (b) and (d) projection. . . . .	16
9	Fluxes at the meridional plane as a function of approaching angle for the low density population (a) and (b), and the high density population (c) and (d) impacting the Moon at the equator in a Mollweide (a) and (c), and all-sky (b) and (d) projection. . . . .	17
10	Meteoroid density distribution according to the MEM3 User Guide. The apex and toroidal meteoroid sources constitute the low-density population, while the helion/antihelion source constitutes the high-density population. Each set of densities follows a log-normal distribution [c.f. Figure 11, Moorhead <i>et al.</i> , 2019]. . . . .	18
11	Non-linear fit of the low density profile in Figure 10 with Eq. 3.2 in SciDAVis, giving the constants for $a \rightarrow A$ , $s \rightarrow \sigma$ , and $m \rightarrow \mu_\delta$ . . . . .	19
12	Non-linear fit of the high density profile in Figure 10 with Eq. 3.2 in SciDAVis, giving the constants for $a \rightarrow A$ , $s \rightarrow \sigma$ , and $m \rightarrow \mu_\delta$ . . . . .	19
13	The Grün interplanetary meteoroid flux as a function of limiting particle mass [Moorhead <i>et al.</i> , 2019, Figure 1], normalized to 1 for a limiting mass equal to or greater than $1\mu\text{g}$ . . . . .	20
14	Mass-limited speed distribution at the lunar surface. . . . .	21
15	Meteor shower flux (variable lines) and sporadic meteoroid flux (horizontal lines) over the course of 2021. Fluxes are quoted to four limiting particle kinetic energies; these kinetic energies correspond to particles with diameters of 0.04 cm, 0.1 cm, 0.3 cm, and 1 cm, assuming a density of $1 \text{ g cm}^{-3}$ and a speed of $20 \text{ km s}^{-1}$ , [see Figure 1, Moorhead <i>et al.</i> , 2020]. . . . .	22
16	Average cumulative lunar ejecta flux-mass distribution for each of three ejecta velocity intervals [Cour-Palais, 1969]. . . . .	28
17	The total ejecta kinetic energy $E_{tot,ej}$ (Equation (4.35)) over impactor energy $E_{imp} = \frac{1}{2}mU^2$ vs. effective impactor to crater radius $\frac{n_1 a}{n_2 R}$ for a lunar regolith target (using SFA in Table 6) with regolith surface bulk density $\rho = 1.3 \text{ g/cc}$ and varying impactor densities. . . . .	32
18	The total ejecta kinetic energy $E_{tot,ej}$ (Equation (4.35)) over impactor energy $E_{imp} = \frac{1}{2}mU^2$ vs. effective impactor to crater radius $\frac{n_1 a}{n_2 R}$ for a lunar regolith target (using WCB in Table 6) with regolith surface bulk density $\rho = 1.3 \text{ g/cc}$ and varying impactor densities. . . . .	32

- 19 The initial speed  $v_p$  vs. initial zenith angle  $\gamma_p$  as a function of distance  $D$  is shown with a distance contour line at  $0.003\pi r_m$  with a point-asset altitude of  $0r_m$  (on the lunar surface). The contour line's color depicts the final incoming zenith angle  $\gamma_s$  where the thickness of the line gives the ratio of the final and initial speeds  $v_s/v_p$ . For a point-asset at the surface, this ratio will always be 1. The intersection of the distance contour line and the black dotted line gives the optimal zenith angle  $\gamma_{p,opt}$  (Equation (4.69)), i.e. the slowest initial speed to reach the contour line distance of  $0.003\pi r_m$ . Since the point-asset is on the lunar surface, there is no minimum bound on the speed (denoted by the black dashed line). . . . . 37
- 20 The initial speed  $v_p$  vs. initial zenith angle  $\gamma_p$  as a function of distance  $D$  is shown with a distance contour line at  $0.032\pi r_m$  with a point-asset altitude of  $0r_m$  (on the lunar surface). The contour line's color depicts the final incoming zenith angle  $\gamma_s$  where the thickness of the line gives the ratio of the final and initial speeds  $v_s/v_p$ . For a point-asset at the surface, this ratio will always be 1. The intersection of the distance contour line and the black dotted line gives the optimal zenith angle  $\gamma_{p,opt}$  (Equation (4.69)), i.e. the slowest initial speed to reach the contour line distance of  $0.032\pi r_m$ . Since the point-asset is on the lunar surface, there is no minimum bound on the speed (denoted by the black dashed line). . . . . 38
- 21 The initial speed  $v_p$  vs. initial zenith angle  $\gamma_p$  as a function of distance  $D$  is shown with a distance contour line at  $0.318\pi r_m$  with a point-asset altitude of  $0r_m$  (on the lunar surface). The contour line's color depicts the final incoming zenith angle  $\gamma_s$  where the thickness of the line gives the ratio of the final and initial speeds  $v_s/v_p$ . For a point-asset at the surface, this ratio will always be 1. The intersection of the distance contour line and the black dotted line gives the optimal zenith angle  $\gamma_{p,opt}$  (Equation (4.69)), i.e. the slowest initial speed to reach the contour line distance of  $0.318\pi r_m$ . Since the point-asset is on the lunar surface, there is no minimum bound on the speed (denoted by the black dashed line). . . . . 39
- 22 The initial speed  $v_p$  vs. initial zenith angle  $\gamma_p$  as a function of distance  $D$  is shown with a distance contour line at  $1.592\pi r_m$  (past the antipode) with a point-asset altitude of  $0r_m$  (on the lunar surface). The contour line's color depicts the final incoming zenith angle  $\gamma_s$  where the thickness of the line gives the ratio of the final and initial speeds  $v_s/v_p$ . For a point-asset at the surface, this ratio will always be 1. The intersection of the distance contour line and the black dotted line gives the optimal zenith angle  $\gamma_{p,opt}$  (Equation (4.69)), i.e. the slowest initial speed to reach the contour line distance of  $1.592\pi r_m$ . Since the point-asset is on the lunar surface, there is no minimum bound on the speed (denoted by the black dashed line). . . . . 40

- 23 The initial speed  $v_p$  vs. initial zenith angle  $\gamma_p$  as a function of distance  $D$  is shown with a distance contour line at  $0.003\pi r_m$  with a point-asset altitude of  $0.01r_m$ . The contour line's color depicts the final incoming zenith angle  $\gamma_s$  where the thickness of the line gives the ratio of the final and initial speeds  $v_s/v_p$ . The intersection of the distance contour line and the black dotted line gives the optimal zenith angle  $\gamma_{p,opt}$  (Equation (4.69)), i.e. the slowest initial speed to reach the contour line distance of  $0.003\pi r_m$ . The black dashed line gives the minimum achievable initial speed  $v_{p,min}$  for a particular initial zenith angle (Equation (4.68)). The intersection of the distance contour line and  $v_{p,min}$  occurs when the final incoming zenith angle  $\gamma_s = 90^\circ$  (i.e., parallel to the local horizon) and marks a branch cut to another branch. The branch to the left of the branch cut are all ejecta hitting the point-asset above the local horizon, whereas the branch to the right are all ejecta hitting below the local horizon. . . . . 46
- 24 The initial speed  $v_p$  vs. initial zenith angle  $\gamma_p$  as a function of distance  $D$  is shown with a distance contour line at  $0.032\pi r_m$  with a point-asset altitude of  $0.01r_m$ . The contour line's color depicts the final incoming zenith angle  $\gamma_s$  where the thickness of the line gives the ratio of the final and initial speeds  $v_s/v_p$ . The intersection of the distance contour line and the black dotted line gives the optimal zenith angle  $\gamma_{p,opt}$  (Equation (4.69)), i.e. the slowest initial speed to reach the contour line distance of  $0.032\pi r_m$ . The black dashed line gives the minimum achievable initial speed  $v_{p,min}$  for a particular initial zenith angle (Equation (4.68)). The intersection of the distance contour line and  $v_{p,min}$  occurs when the final incoming zenith angle  $\gamma_s = 90^\circ$  (i.e., parallel to the local horizon) and marks a branch cut to another branch. The branch to the left of the branch cut are all ejecta hitting the point-asset above the local horizon, whereas the branch to the right are all ejecta hitting below the local horizon. . . . . 47
- 25 The initial speed  $v_p$  vs. initial zenith angle  $\gamma_p$  as a function of distance  $D$  is shown with a distance contour line at  $0.318\pi r_m$  with a point-asset altitude of  $0.01r_m$ . The contour line's color depicts the final incoming zenith angle  $\gamma_s$  where the thickness of the line gives the ratio of the final and initial speeds  $v_s/v_p$ . The intersection of the distance contour line and the black dotted line gives the optimal zenith angle  $\gamma_{p,opt}$  (Equation (4.69)), i.e. the slowest initial speed to reach the contour line distance of  $0.318\pi r_m$ . The black dashed line gives the minimum achievable initial speed  $v_{p,min}$  for a particular initial zenith angle (Equation (4.68)). The intersection of the distance contour line and  $v_{p,min}$  occurs when the final incoming zenith angle  $\gamma_s = 90^\circ$  (i.e., parallel to the local horizon) and marks a branch cut to another branch. The branch to the left of the branch cut are all ejecta hitting the point-asset above the local horizon, whereas the branch to the right are all ejecta hitting below the local horizon. . . . . 48

- 26 The initial speed  $v_p$  vs. initial zenith angle  $\gamma_p$  as a function of distance  $D$  is shown with a distance contour line at  $1.592\pi r_m$  with a point-asset altitude of  $0.01r_m$ . The contour line's color depicts the final incoming zenith angle  $\gamma_s$  where the thickness of the line gives the ratio of the final and initial speeds  $v_s/v_p$ . The intersection of the distance contour line and the black dotted line gives the optimal zenith angle  $\gamma_{p,opt}$  (Equation (4.69)), i.e. the slowest initial speed to reach the contour line distance of  $1.592\pi r_m$ . The black dashed line gives the minimum achievable initial speed  $v_{p,min}$  for a particular initial zenith angle (Equation (4.68)). The intersection of the distance contour line and  $v_{p,min}$  occurs when the final incoming zenith angle  $\gamma_s = 90^\circ$  (i.e., parallel to the local horizon) and marks a branch cut to another branch. The branch to the left of the branch cut are all ejecta hitting the point-asset above the local horizon, whereas the branch to the right are all ejecta hitting below the local horizon. . . . . 49
- 27 The initial speed  $v_p$  vs. initial zenith angle  $\gamma_p$  as a function of distance  $D$  is shown with a distance contour line at  $0.003\pi r_m$  with a point-asset altitude of  $0.1r_m$ . The contour line's color depicts the final incoming zenith angle  $\gamma_s$  where the thickness of the line gives the ratio of the final and initial speeds  $v_s/v_p$ . The intersection of the distance contour line and the black dotted line gives the optimal zenith angle  $\gamma_{p,opt}$  (Equation (4.69)), i.e. the slowest initial speed to reach the contour line distance of  $0.003\pi r_m$ . The black dashed line gives the minimum achievable initial speed  $v_{p,min}$  for a particular initial zenith angle (Equation (4.68)). The intersection of the distance contour line and  $v_{p,min}$  occurs when the final incoming zenith angle  $\gamma_s = 90^\circ$  (i.e., parallel to the local horizon) and marks a branch cut to another branch. The branch to the left of the branch cut are all ejecta hitting the point-asset above the local horizon, whereas the branch to the right are all ejecta hitting below the local horizon. . . . . 50
- 28 The initial speed  $v_p$  vs. initial zenith angle  $\gamma_p$  as a function of distance  $D$  is shown with a distance contour line at  $0.032\pi r_m$  with a point-asset altitude of  $0.1r_m$ . The contour line's color depicts the final incoming zenith angle  $\gamma_s$  where the thickness of the line gives the ratio of the final and initial speeds  $v_s/v_p$ . The intersection of the distance contour line and the black dotted line gives the optimal zenith angle  $\gamma_{p,opt}$  (Equation (4.69)), i.e. the slowest initial speed to reach the contour line distance of  $0.032\pi r_m$ . The black dashed line gives the minimum achievable initial speed  $v_{p,min}$  for a particular initial zenith angle (Equation (4.68)). The intersection of the distance contour line and  $v_{p,min}$  occurs when the final incoming zenith angle  $\gamma_s = 90^\circ$  (i.e., parallel to the local horizon) and marks a branch cut to another branch. The branch to the left of the branch cut are all ejecta hitting the point-asset above the local horizon, whereas the branch to the right are all ejecta hitting below the local horizon. . . . . 51

29	The initial speed $v_p$ vs. initial zenith angle $\gamma_p$ as a function of distance $D$ is shown with a distance contour line at $0.318\pi r_m$ with a point-asset altitude of $0.1r_m$ . The contour line's color depicts the final incoming zenith angle $\gamma_s$ where the thickness of the line gives the ratio of the final and initial speeds $v_s/v_p$ . The intersection of the distance contour line and the black dotted line gives the optimal zenith angle $\gamma_{p,opt}$ (Equation (4.69)), i.e. the slowest initial speed to reach the contour line distance of $0.318\pi r_m$ . The black dashed line gives the minimum achievable initial speed $v_{p,min}$ for a particular initial zenith angle (Equation (4.68)). The intersection of the distance contour line and $v_{p,min}$ occurs when the final incoming zenith angle $\gamma_s = 90^\circ$ (i.e., parallel to the local horizon) and marks a branch cut to another branch. The branch to the left of the branch cut are all ejecta hitting the point-asset above the local horizon, whereas the branch to the right are all ejecta hitting below the local horizon. . . . .	52
30	The initial speed $v_p$ vs. initial zenith angle $\gamma_p$ as a function of distance $D$ is shown with a distance contour line at $1.592\pi r_m$ with a point-asset altitude of $0.1r_m$ . The contour line's color depicts the final incoming zenith angle $\gamma_s$ where the thickness of the line gives the ratio of the final and initial speeds $v_s/v_p$ . The intersection of the distance contour line and the black dotted line gives the optimal zenith angle $\gamma_{p,opt}$ (Equation (4.69)), i.e. the slowest initial speed to reach the contour line distance of $1.592\pi r_m$ . The black dashed line gives the minimum achievable initial speed $v_{p,min}$ for a particular initial zenith angle (Equation (4.68)). The intersection of the distance contour line and $v_{p,min}$ occurs when the final incoming zenith angle $\gamma_s = 90^\circ$ (i.e., parallel to the local horizon) and marks a branch cut to another branch. The branch to the left of the branch cut are all ejecta hitting the point-asset above the local horizon, whereas the branch to the right are all ejecta hitting below the local horizon. . . . .	53
31	A bird's eye view of the asset (circle of radius $a$ ) and the crater location (point $C$ ) projected on the surface of the Moon. The FOV the asset encompasses from the point of view of the crater is $2\beta_{max}$ . . . . .	54
32	A bird's eye view of the asset (circle of radius $a$ ) and the crater location (point $C$ ) projected on the surface of the Moon. The special case shown occurs when the antipode of the crater is inside the asset and there is no restriction on the FOV angle $\beta_i$ . . . . .	55
33	The ejecta speed $v/U$ (Equation (5.3)) vs. location in the crater $x/a$ for a lunar regolith target (using SFA in Table 6) with regolith surface bulk density $\rho = 1.3$ g/cc and an impactor density of 4.0 g/cc (e.g., MEM high density population). Each curve has a set effective impactor to crater radius $\frac{n_1 a}{n_2 R}$ . . . . .	60

34	The ejecta speed $v/U$ (Equation (5.3)) vs. location in the crater $x/a$ for a lunar regolith target (using SFA in Table 6) with regolith surface bulk density $\rho = 1.3$ g/cc and an impactor density of 1.0 g/cc (e.g., MEM low density population). Each curve has a set effective impactor to crater radius $\frac{n_1 a}{n_2 R}$ . . . . .	60
35	The ejecta speed $v/U$ (Equation (5.3)) vs. effective impactor to crater radius $\frac{n_1 a}{n_2 R}$ for a lunar regolith target (using SFA and WCB in Table 6) with regolith surface bulk density $\rho = 1.3$ g/cc and an impactor density of 1.0 and 4.0 g/cc (e.g., MEM low and high density population). . . . .	61
36	A matrix of plots showing the ejecta hitting a cylindrical asset (in a plane intersecting the cylinder's symmetry axis) on the surface for various asset sizes and crater-to-asset distances. Each plot gives three colors for the ejecta hitting the side (blue), bottom (red), and the top (green) as a function of initial ejecta speed $v_p$ vs. initial ejecta zenith angle $\gamma_p$ . . . . .	65
37	A matrix of plots showing the ejecta hitting a cylindrical asset (in a plane intersecting the cylinder's symmetry axis) with a height above the surface of $0.01r_m$ for various asset sizes and crater-to-asset distances. Each plot gives three colors for the ejecta hitting the side (blue), bottom (red), and the top (green) as a function of initial ejecta speed $v_p$ vs. initial ejecta zenith angle $\gamma_p$ . . . . .	66
38	A matrix of plots showing the ejecta hitting a cylindrical asset (in a plane intersecting the cylinder's symmetry axis) with a height above the surface of $0.1r_m$ for various asset sizes and crater-to-asset distances. Each plot gives three colors for the ejecta hitting the side (blue), bottom (red), and the top (green) as a function of initial ejecta speed $v_p$ vs. initial ejecta zenith angle $\gamma_p$ . . . . .	67

## List of Tables

1	Porosity for various depths. . . . .	2
2	The change of the shear strength of the lunar soil with depth. . . . .	6
3	Digitized data points from Figure 4, see <i>Carrier III</i> [2003]. . . . .	8
4	Cone angles of upstream and downstream of impact derived from Figure 18 of <i>Gault and Wedekind</i> [1978]. . . . .	24
5	A compilation of indices of the various particle size distribution descriptions. Values that are in bold are the index that was originally used in the corresponding source. . . . .	26
6	Summary of constants used in the <i>Housen and Holsapple</i> [2011] ejecta model. . . . .	62

## Listings

- |   |   |    |
|---|---|----|
| 1 | An example email that is sent to JPL Horizons to compute an ephemeris file that is centered on the Moon at a location of 90° longitude, −65° latitude, and 0.6 km above the surface for 11 years. . . . . | 11 |
| 2 | Python script to convert JPL Horizons ephemeris file type to be read into the Meteoroid Engineering Model. . . . .  | 12 |

## 1 Executive Summary

## 2 Lunar Regolith Properties

### 2.1 Porosity

The lunar regolith porosity is related to the amount of free space between individual grains. The greater the porosity, the more void space is present. Table 3.4.2.3.4-1 of the DSNE gives values of the porosity as a function of depth down to 60 cm derived from Apollo core measurements (copied from Table 9.5 of the Lunar Sourcebook, *Heiken et al.* [1991]) and shown here in Table 1.

Table 1: Porosity for various depths.

Depth Range (cm)	Average Porosity, n (%)
0 – 15	52 ± 2
0 – 30	49 ± 2
30 – 60	44 ± 2
0 – 60	46 ± 2

### 2.2 Density

The bulk density ( $\rho$ ) of the lunar regolith is defined as the mass of material in a given volume, which relates the particle density ( $\rho_p$ ) and porosity ( $n$ ) to the bulk density as (see Section 3.4.2.3.1 of the DSNE or Chapter 9 of the Lunar Sourcebook)

$$\rho = \rho_p(1 - n). \quad (2.1)$$

The DSNE suggests using  $\rho_p = 3.1 \text{ g/cm}^3$  for the average particle density over the entire Moon. Otherwise, the typical highlands particle density is  $\rho_p = 2.75 \pm 0.1 \text{ g/cm}^3$  whereas the typical mare particle density is  $\rho_p = 3.35 \pm 0.1 \text{ g/cm}^3$ .

The bulk density<sup>1</sup> as a function of depth has been characterized multiple ways (Figure 1). An empirical hyperbolic fit to in situ Apollo data takes the form

$$\rho(z) = 1.92 \frac{z + 12.2}{z + 18}, \quad (2.2)$$

where  $z$  is the depth in cm and  $\rho$  is in units of  $\text{g/cm}^3$ . Bulk density increases with depth. At the surface ( $z = 0$ ), the density is  $1.30 \text{ g/cm}^3$ , and approaches  $1.92 \text{ g/cm}^3$  at the limits reached by the Apollo drill core samples, about  $z = 3 \text{ m}$ . In order to get an up-to-depth average of the bulk density, take

$$\rho_{avg,depth}(z) = \frac{1}{z} \int_0^z dz' \rho(z'), \quad (2.3)$$

---

<sup>1</sup>Follows the average particle density of  $3.1 \text{ g/cm}^3$  for all depths with a porosity depth dependence following Table 1, see the *porosity of lunar soil* paragraph on page 492 in the Lunar Sourcebook.

which gives (compare with the equation for  $d_m$  on page 494 of the Lunar Sourcebook)

$$\rho_{avg,depth}(z) = 1.92 \left[ 1 - \frac{5.8 \ln \left( \frac{z+18}{18} \right)}{z} \right]. \quad (2.4)$$

For example, the average bulk density of the regolith with a depth range of 0 – 60 cm would be  $\rho_{avg,depth}(60) = 1.65 \text{ g/cm}^3$ .

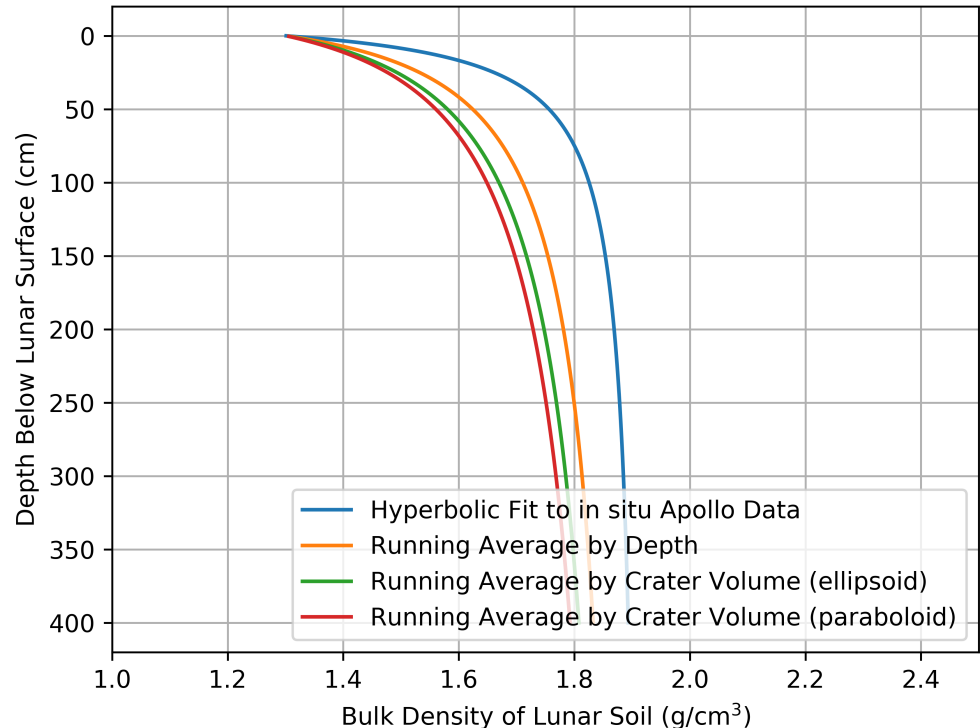


Figure 1: A comparison of the regolith bulk density for a certain depth (blue), the depth-averaged bulk density (orange), and the volume-averaged bulk density (green). See also, Figure 9.16 of the Lunar Sourcebook [[Heiken et al., 1991](#)].

For a higher-fidelity estimate of the average bulk density sampled by an impact crater, a volume-average can be used instead of a depth-average, given by

$$\rho_{avg,volume}(z) = \frac{\int dV \rho(z')}{\int dV}. \quad (2.5)$$

Expanding the integral in a cylindrical coordinate system and assuming an ellipsoidal

crater shape, Equation (2.5) becomes

$$\rho_{avg,ellipsoid}(z) = \frac{\int_0^z \int_0^R \sqrt{1-z'^2/z^2} \int_0^{2\pi} d\phi r dr dz' \rho(z')}{\int_0^z \int_0^R \sqrt{1-z'^2/z^2} \int_0^{2\pi} d\phi r dr dz'} \quad (2.6)$$

$$= \frac{1.92}{4z^3} \left[ z(6ab - 6b^2 - 3az + 3bz + 4z^2) + 6(a-b)(b^2 - z^2) \ln \left( \frac{b}{z+b} \right) \right], \quad (2.7)$$

for the volume-averaged density in g/cm<sup>3</sup> with  $z$  in cm, where  $a = 12.2$  and  $b = 18$ . Comparing to the earlier example, the average bulk density of the regolith with a depth range of 0 – 60 cm would be  $\rho_{avg,ellipsoid}(60) = 1.60$  g/cm<sup>3</sup>; ~ 3% less than  $\rho_{avg,depth}(60) = 1.65$  g/cm<sup>3</sup>.

Instead of an ellipsoidal shape, if a paraboloid crater shape is assumed, Equation (2.5) becomes

$$\rho_{avg,paraboloid}(z) = \frac{\int_0^z \int_0^R \sqrt{1-z'/z} \int_0^{2\pi} d\phi r dr dz' \rho(z')}{\int_0^z \int_0^R \sqrt{1-z'/z} \int_0^{2\pi} d\phi r dr dz'} \quad (2.8)$$

$$= \frac{1.92}{z/2} \left[ b - a + \frac{z}{2} - \frac{(a-b)(b+z) \ln \left( \frac{b}{z+b} \right)}{z} \right], \quad (2.9)$$

using the same values for  $a$  and  $b$  as before. Again, comparing to the prior depth average example, the average bulk density of the regolith with a depth range of 0 – 60 cm would be  $\rho_{avg,paraboloid}(60) = 1.58$  g/cm<sup>3</sup>; ~ 4% less than  $\rho_{avg,depth}(60) = 1.65$  g/cm<sup>3</sup>. The expression given in Equation (2.9) is useful for computing the ejected mass from a crater<sup>2</sup>, given a crater depth  $z$ .

The expressions for the regolith density at a certain depth  $z$ , weighted by depth, and weighted by crater volume (ellipsoid and paraboloid) are given by Equations (2.2), (2.4), and (2.7), (2.9), respectively (Figure 1). The relative error between the different methods are shown in Figure 2. The crater volume is approximated as a half-ellipsoid with two of the dimensions scaled by the crater radius  $R$  and one dimension scaled by the crater depth  $z$ , sliced such that the half-ellipsoid is symmetric about the surface normal for Equation (2.7). On the other hand, a paraboloid-shaped crater is used for Equation (2.9). For a given crater, more of the volume is near the surface so that more weight is given by bulk densities that originate near the surface. In contrast, the depth-averaged bulk density takes the bulk density at each depth equally. This results in the volume-averaged bulk density to be slightly less than the depth-averaged bulk density, as shown in Figure 1. In addition, comparing an ellipsoidal crater vs. a parabolic crater, the parabolic crater (typically used in literature, see [Singer et al. \[2020\]](#)) exhibits the softest increase of the average bulk density as a function of depth.

The lunar meteoroid ejecta model currently uses a constant regolith density for all depths for simplicity. The higher fidelity expressions shown above are for future reference if it is found that the regolith density has an important effect on the final environment.

<sup>2</sup>In an iterative fashion, since the crater radius depends on the regolith density.

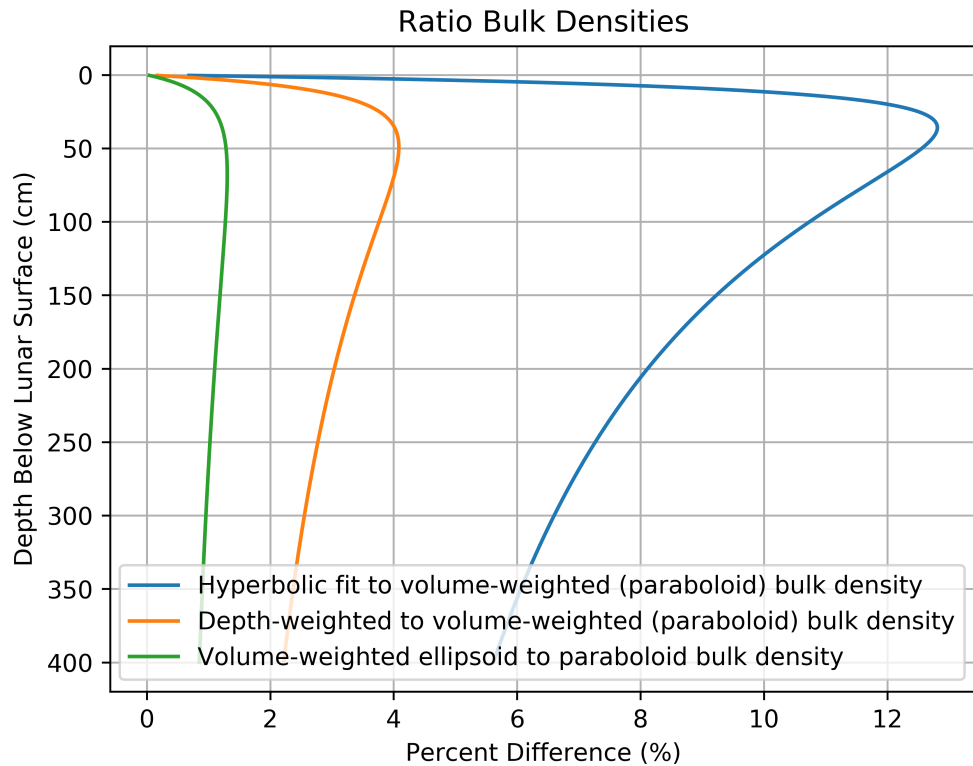


Figure 2: Relative error of using the density at a certain depth (blue) and using the depth-weighted average (orange) of the regolith bulk density.

## 2.3 Strength

The regolith includes fine-grained material from the lunar surface down to  $\sim 10$  m depth. The large-scale, coarse grained ejecta that is ballistically transported resides from 10 m to about 2 km below the surface (Fig 4.22 of the Lunar Sourcebook, [Heiken et al. \[1991\]](#)).

The strength of the regolith can be measured in different ways, depending on the use. In the case of modeling impacts, the shear strength [see Section 3 of [Housen and Holsapple, 2011](#)] of loose regolith and tensile strength of solid rock can be used. Since all of the impacts studied in this model will create craters less than 2 km, the shear strength was used for both loose regolith and large scale ejecta material. The shear strength of the lunar soil increases with depth, as depicted by both Figure 9.26 of the Lunar Sourcebook (reproduced in Figure 3) and Table 12 of [Slyuta \[2014\]](#), shown in Table 2.

The average shear strength (green curve) in Figure 3 can be expressed by the

Table 2: The change of the shear strength of the lunar soil with depth.

Depth (cm)	Shear strength (kPa)
5	0.1 – 2.5
50	1 – 3.5
100	2 – 4
200	4 – 8

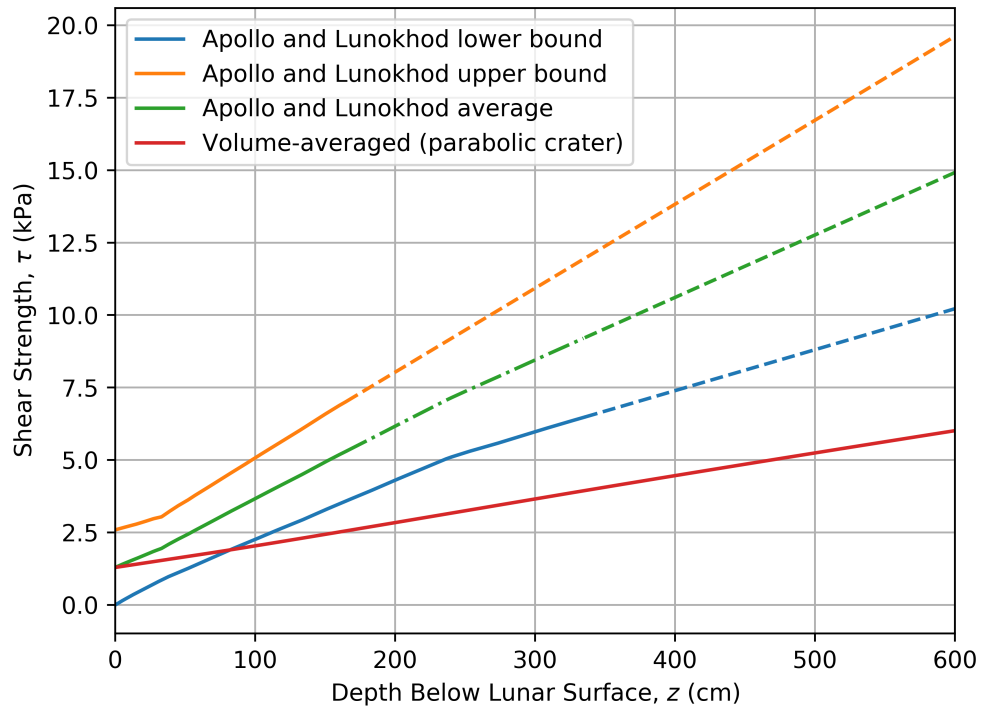


Figure 3: The range of regolith shear strength as a function of depth below the lunar surface taken from Figure 9.26 of the Lunar Sourcebook. The average shear strength is also calculated (green). Dashed lines indicate extrapolated points beyond available data. The volume-averaged shear strength (red) assumes a parabolic-shaped crater of depth  $z$ .

piece-wise form

$$\tau(z) = \begin{cases} \frac{z}{45.55} + 1.288, & 0 \leq z < 50 \text{ cm} \\ \frac{z}{40.21} + 1.144, & 50 \text{ cm} \leq z < 250 \text{ cm} \\ \frac{z}{46.06} + 1.942, & z \geq 250 \text{ cm} \end{cases} . \quad (2.10)$$

Assuming the crater has a parabolic shape and that the effective shear strength is the

volume-average (similar approach to Equation (2.5)), Equation (2.10) becomes

$$\tau(z) = \begin{cases} \frac{z}{136.65} + 1.288, & 0 \leq z < 50 \text{ cm} \\ \frac{z}{120.63} + 1.144 + \frac{7.163}{z} - \frac{118.33}{z^2}, & 50 \text{ cm} \leq z < 250 \text{ cm} \\ \frac{z}{138.18} + 1.942 - \frac{194.81}{z} + \frac{16902}{z^2}, & z \geq 250 \text{ cm} \end{cases}, \quad (2.11)$$

as shown by the red curve in Figure 3.

## 2.4 Particle Size Distribution

The cumulative distribution function (CDF) of the regolith particle sizes<sup>3</sup> are fit to several Apollo samples, as shown in Figure 4. An impact may modify and reorganize preexisting particle size distributions depending on the ejected speed (see Section 4.2). For this section, however, the unmodified regolith size distribution is given for reference. The digitized data from Figure 4 is shown in Table 3.

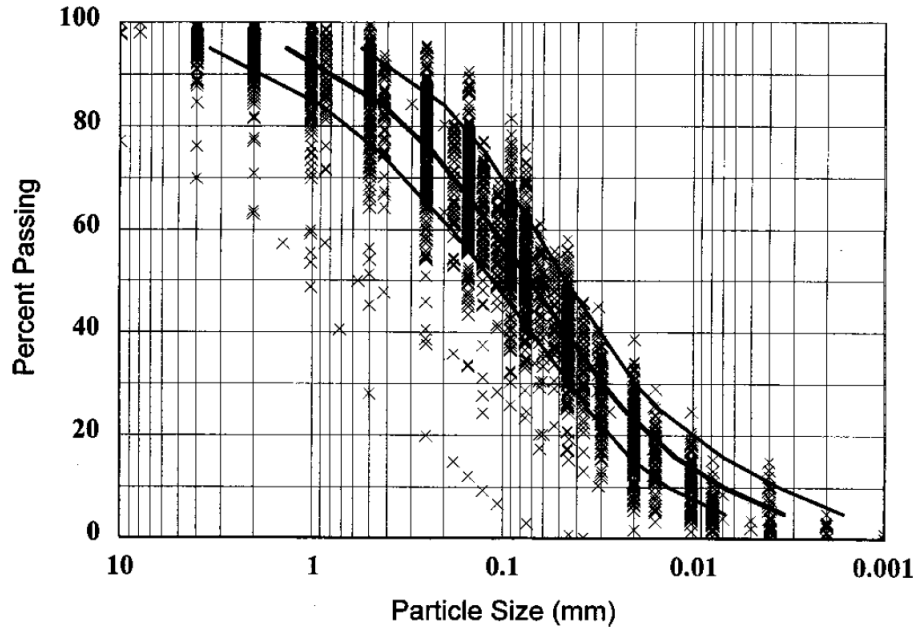


Figure 4: Geotechnical particle size distribution: middle curve showing the average distribution; left-hand and right-hand curves showing  $\pm 1$  standard deviation [Carrier III, 2003]. Note, that the percent passing is normalized by mass and not particle number [see Carrier, 1973].

<sup>3</sup>In the context here, particle size is defined as the particle diameter of a spherical-shaped particle. Other sections may define size by the radius.

Table 3: Digitized data points from Figure 4, see *Carrier III [2003]*.

Particle Diameter (mm)	Cumulative Percent by Mass
0.003380248352585	5.17682028091534
0.003794441295246	6.09401642297017
0.00451292465605	7.2776812909626
0.0053674729594	8.4354410787182
0.006383732464611	9.71063723021409
0.007592176031253	11.2086170717467
0.009029116435596	12.9190185712213
0.010737989052827	14.65100763756
0.012769865152208	16.6247774527757
0.015185144104918	19.116648872728
0.018057261192048	21.6025237463292
0.02136872870221	24.2948870610798
0.025044648784976	27.0334149904509
0.029494364580794	29.8741284657866
0.033098954040892	32.8807708128992
0.037145453042138	35.6150479687852
0.042499223173782	38.2089250804786
0.048155933590968	41.1181012805662
0.054042887826956	43.8970091889745
0.060942690951498	46.6685810695819
0.068720899309714	49.7075873197331
0.077869796000019	52.4248808897808
0.087812953450079	55.0874612212659
0.098550426314892	57.6779504306929
0.112206724061769	60.6265864834011
0.127759476997186	63.3415731364729
0.145465039759366	66.2037864789212
0.168035843630453	69.131911259623
0.19411176280305	71.9484525505802
0.222083419318477	74.7285290349147
0.259044020108005	77.2129935126797
0.30803890584547	79.7150699642405
0.366294873918129	82.3305792671413
0.435590409221425	84.5720349114709
0.518029785192508	86.3256115446736
0.616085725364177	87.9108051563369
0.732705596850257	89.4631856663669
0.871382022892136	91.1718601604924
1.03629488039837	92.9535006306183
1.23245384670266	94.5235829454768

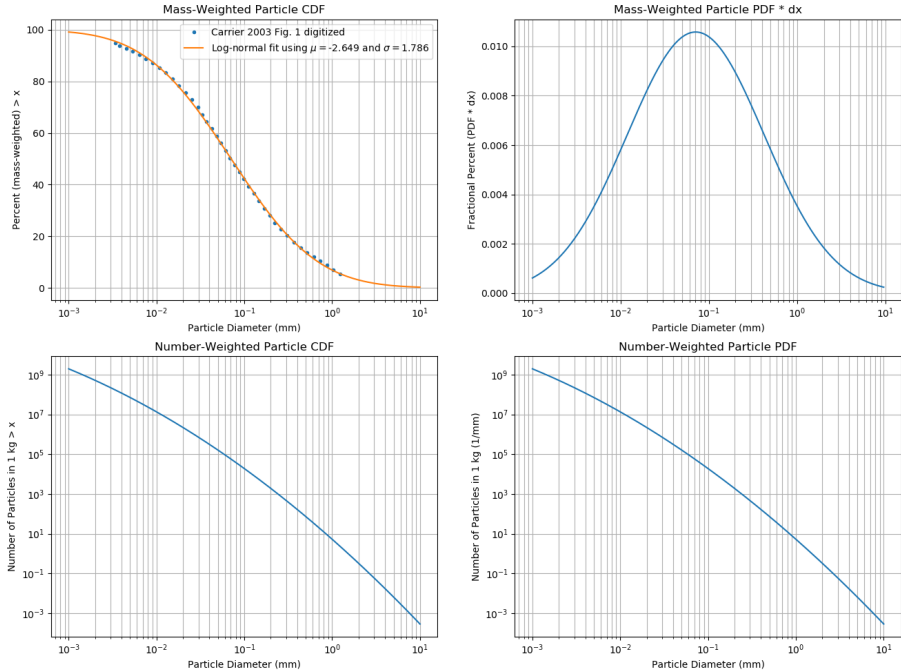


Figure 5: Plots of the mass-weighted and number-weighted CDFs and PDFs derived from [Carrier III \[2003\]](#). Top left: the digitized data from Figure 1 of [Carrier III \[2003\]](#) is shown with the log-normal distribution fit. Top right: The mass-weighted PDF  $\ast dx$  is shown to indicate what particle size dominates the contribution of mass. Bottom left: The number-weighted CDF showing number of particles in 1 kg of regolith greater than a size  $x$ . Bottom right: The number-weighted PDF is shown in units of  $\text{mm}^{-1}$ .

[Carrier III \[2003\]](#) specifically called out that the mass-weighted CDF can be modeled by a log-normal distribution. This assumption is made below. By definition, a log-normal distribution is given by

$$F_{\text{kg}}(> x) = 1 - F_{\text{kg}}(< x) = \frac{1}{2} \left[ 1 - \text{erf} \left( \frac{\ln x - \mu}{\sqrt{2}\sigma} \right) \right], \quad (2.12)$$

where  $x$  is the particle diameter size in units of mm,  $\mu$  is the expected value of  $\ln x$ , and  $\sigma$  is the standard deviation of  $\ln x$ .

The PDF is then given by

$$f_{\text{kg}}(x) = \frac{1}{\sigma\sqrt{2\pi}} \frac{1}{x} \exp \left[ -\frac{(\ln x - \mu)^2}{2\sigma^2} \right]. \quad (2.13)$$

In order to have the number-weighted PDF and CDF, we begin with  $f_{kg}(x)$  and divide by the mass of a given particle size (diameter), [e.g., Equation (7) of [Koschny and Grün, 2001](#)]

$$m(x) = \frac{\pi}{6} \rho x^3, \quad (2.14)$$

so that we have (assuming  $F_{kg}$  represents the CDF for 1 kg of regolith)

$$f_{number}(x) = \frac{f_{kg}(x)}{m(x)} = \frac{6}{\pi \rho} \frac{1\text{kg}}{1\text{mm}^3} \frac{1}{\sigma \sqrt{2\pi}} \frac{1}{x^4} \exp\left[-\frac{(\ln x - \mu)^2}{2\sigma^2}\right], \quad (2.15)$$

for the number-weighted PDF. To arrive at the number-weighted CDF, integration over  $f_{number}(x)$  is done such that

$$F_{number}(> x) = \int_x^\infty dx' f_{number}(x'). \quad (2.16)$$

Solving the integral, the number-weighted CDF is given by

$$F_{number}(> x) = \frac{6}{\pi \rho} \frac{1\text{kg}}{1\text{mm}^3} \frac{1}{\sigma \sqrt{2\pi}} \left[ 1 - \operatorname{erf}\left(\frac{\ln x - \mu + 3\sigma^2}{\sqrt{2}\sigma}\right) \right] \exp\left(-3\mu + \frac{9\sigma^2}{2}\right), \quad (2.17)$$

which is the number of particles of diameter  $x$  or greater in 1 kg of regolith. For  $F_{number}(< x)$ , flip the minus sign to a plus sign on the error function<sup>4</sup>.

Fitting the mass-weighted CDF  $F(< x)$  to Figure 4, the following parameters are obtained:

$$\mu = -2.649, \quad (2.18)$$

$$\sigma = 1.786, \quad (2.19)$$

where the mean, median, and mode particle size (weighted by mass) is

$$x_{\text{mean}} = \exp\left(\mu + \frac{\sigma^2}{2}\right) = 34.8\mu\text{m}, \quad (2.20)$$

$$x_{\text{median}} = \exp(\mu) = 7.07\mu\text{m}, \quad (2.21)$$

$$x_{\text{mode}} = \exp(\mu - \sigma^2) = 0.291\mu\text{m}. \quad (2.22)$$

If the mean, median, and mode particle size weighted by number are needed, then the modified parameters are

$$\mu^* = \mu - 3\sigma^2 = -12.22, \quad (2.23)$$

$$\sigma^* = \sigma = 1.786, \quad (2.24)$$

giving the following (now weighted by number):

$$x_{\text{mean}}^* = \exp\left(\mu^* + \frac{\sigma^{*2}}{2}\right) = 2.43\text{ nm}, \quad (2.25)$$

$$x_{\text{median}}^* = \exp(\mu^*) = 0.494\text{ nm}, \quad (2.26)$$

$$x_{\text{mode}}^* = \exp(\mu^* - \sigma^{*2}) = 0.0203\text{ nm}. \quad (2.27)$$

---

<sup>4</sup>Note that  $\operatorname{erfc}(x) = 1 - \operatorname{erf}(x)$ .

Note that these set of averages are outside the range of the data provided in *CARRIER III* [2003] and are only valid if the log-normal distribution holds for these very small particles. This regime is on the order of several atomic nuclei large.

As an example, if the number of particles greater than  $1 \mu\text{g}$  per 1 kg of regolith are needed, then use Equation (2.17) (assuming a regolith density of  $\rho = 3.1 \text{ g / cm}^3$  such that  $x(1\mu\text{g}) = 8.509\mu\text{m}$ )

$$F_{\text{number}}(> x = 8.509\mu\text{m}) = 3.146 \times 10^7 \text{ # of particles per 1 kg of regolith.} \quad (2.28)$$

## 3 Primary Flux Environment

### 3.1 Space-Time Dependence of Environment

The primary environment that is responsible for creating ejecta by impacting the lunar surface varies in both location on the Moon as well as in time. For a time-averaged background environment, the sporadic meteoroid complex (Section 3.2) and near-Earth object (Section 3.3) populations are used as input to the ejecta model over a 19-year time span. Short-term environments may also be generated that have the option to include the meteor showers (Section 3.4, forward work). Time-varying environments can also be generated by providing consecutive ephemeris definitions in time. If a single time frame is used, it is thought of as the average environment over that time frame.

The location and time span of the primary environment is defined by an ephemeris, or trajectory file, discussed in Section 3.1.1.

#### 3.1.1 Ephemeris Definition

The ephemeris definitions of locations on the Moon are generated by using the service provided by JPL Horizons at [ssd.jpl.nasa.gov/horizons/](http://ssd.jpl.nasa.gov/horizons/). One way to query their system is to send an email that defines the particular inputs desired, e.g., see Listing 1, which makes it easier to streamline generating many ephemeris files quickly.

Listing 1: An example email that is sent to JPL Horizons to compute an ephemeris file that is centered on the Moon at a location of  $90^\circ$  longitude,  $-65^\circ$  latitude, and 0.6 km above the surface for 11 years.

```

1 To: Horizons Ephemeris System <horizons@ssd.jpl.nasa.gov>
2 Subject: JOB
3
4
5 !$$SOF
6 COMMAND= '301'
7 CENTER= 'coord@301'
8 COORD_TYPE= 'GEODETIC'
9 SITE_COORD= '90.0,-65.0,0.6'
10 MAKE_EPHEM= 'YES'
11 TABLE_TYPE= 'VECTORS'
12 START_TIME= '2020-01-01'
```

```

13 STOP_TIME= '2039-01-01
14 STEP_SIZE= '10000'
15 OUT_UNITS= 'KM-S'
16 REF_PLANE= 'ECLIPTIC'
17 REF_SYSTEM= 'J2000'
18 VECT_CORR= 'NONE'
19 VEC_LABELS= 'NO'
20 VEC_DELTA_T= 'NO'
21 CSV_FORMAT= 'NO'
22 OBJ_DATA= 'YES'
23 VEC_TABLE= '3'
24 !$$EOF

```

In order to convert the ephemeris file received from JPL Horizons to a file type that the Meteoroid Engineering Model (MEM) program can read, a Python script is used as shown in Listing 2.

Listing 2: Python script to convert JPL Horizons ephemeris file type to be read into the Meteoroid Engineering Model.

```

1 # Title : ephemeris_parser.py
2 # Project: Lunar Meteoroid Ejecta DSNE Environment
3 # Description: Convert JPL Horizons ephemeris data to MEM readable input
4 # Author: Anthony M. DeStefano
5 # Company: NASA/MSFC/EV44
6 # E-mail: anthony.m.destefano@nasa.gov
7 # Office phone: 256-544-3094
8 # Date last edited: 3/10/2020
9
10 import glob
11
12 offset = 58 # size of header
13 cycle = 4   # number of rows for a set of data (same JD timestamp)
14
15 for filepath in glob.iglob('Horizons*.txt'):
16     print(filepath)
17     with open(filepath) as fp:
18         with open('MEM_input_' + filepath, 'w') as out_file:
19             out_file.write('#\n#\n#\n#\n#-----JD-----X-----\n#\n#\n#\n#\n#-----Y-----Z-----VX-----VY-----VZ\n')
20             for cnt, line in enumerate(fp):
21                 # skip footer info
22                 if line == '$$EOE\n':
23                     break
24                 # skip header info
25                 if cnt > offset-1:
26                     # Read Julian Date
27                     if (cnt - offset) % cycle == 0:
28                         out_file.write(line[:17])
29                     # Read position and velocity vector (two sets of 3
30                     components)
31                     elif (cnt - offset) % cycle != 3:
32                         for val in line.split():
33                             # need -1 to flip vector from origin on the lunar
surface to origin to Moon's center
out_file.write('_' + str(-1.0*float(val)))

```

```

34      # Skip the last vector and print a new line
35      else:
36          out_file.write( '\n' )

```

Several ephemeris files can be used to define local primary environments on the Moon by specifying different latitude-longitude coordinates. As an example, 5-degree increments can be used in latitude going from the north pole<sup>5</sup> ( $+90^\circ$ ) to the south pole ( $-90^\circ$ ) and 90-degrees increments can be used in longitude to define the meridian ( $0^\circ$ ), eastern limb ( $+90^\circ$ ), far side ( $+180^\circ$ ), and the western limb ( $+270^\circ$ ) locations.

## 3.2 Sporadic Meteoroid Complex

The primary flux of sporadic meteoroids onto the surface of the Moon changes depending on the selenographic location on the Moon. Because of this effect, ephemeris data<sup>6</sup> was generated for different latitudes and longitudes on the Moon in 5-degree increments from pole to pole, and in 90-degree increments in longitude. A time frame of 19 years was chosen, or a Metonic cycle, which takes into account many different Sun-Earth-Moon geometries. The Meteoroid Engineering Model (MEM) [Moorhead et al., 2019] is used to generate the sporadic meteoroids, i.e., the background flux.

As an example, in Figure 6, the speed-angle flux distribution is shown at the equator and at the poles for the low and high density MEM populations. Note that the fluxes in the northern and southern hemispheres are symmetric about the equator. It can be seen from Figure 6 that the impact angles and speeds are highly dependent on the impact latitude on the Moon and hence warrant a more sophisticated approach to computing the secondary fluxes. It cannot be assumed that most impacts are at 45 degrees or are not highly oblique.

Other time frames may be simulated, such a week, a month, or a year, and can also vary as a function of time. In the current model output, a 19-year averaged flux is used.

### 3.2.1 Angular Distribution

The angular distribution of the primary fluxes can be viewed in a Mollweide and all-sky (polar) projection for both the low- and high-density components of the sporadic meteoroids. Three specific latitudinal regions are depicted in Figures 7, 8, and 9 for the south pole,  $-45^\circ$  latitude, and the equator, respectively, at the central meridian ( $0^\circ$  longitude).

The fluxes from the low- and high-density components seem to originate from opposing locations in the sky [e.g., see Figure 2.2 of Moorhead et al., 2019]. The shift is due to the high-density population meteoroids coming from mainly the ecliptic plane (helion and anti-helion sources) while the low-density population tends to come from higher inclinations (toroidal and apex sources).

The figures that follow show a departure from a purely isotropic flux source and the effect on the impact angle on the planetary surface. As shown in Pierazzo and

<sup>5</sup>The poles must not be exactly  $\pm 90^\circ$ , but offset slightly to avoid errors in the JPL Horizons system.

<sup>6</sup>Horizons Ephemeris System <horizons@ssd.jpl.nasa.gov>.

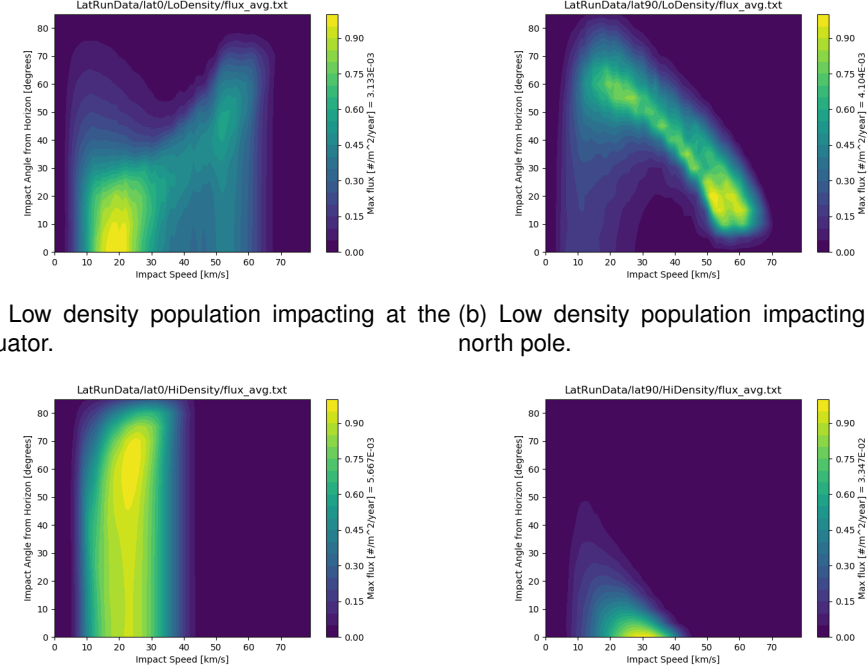
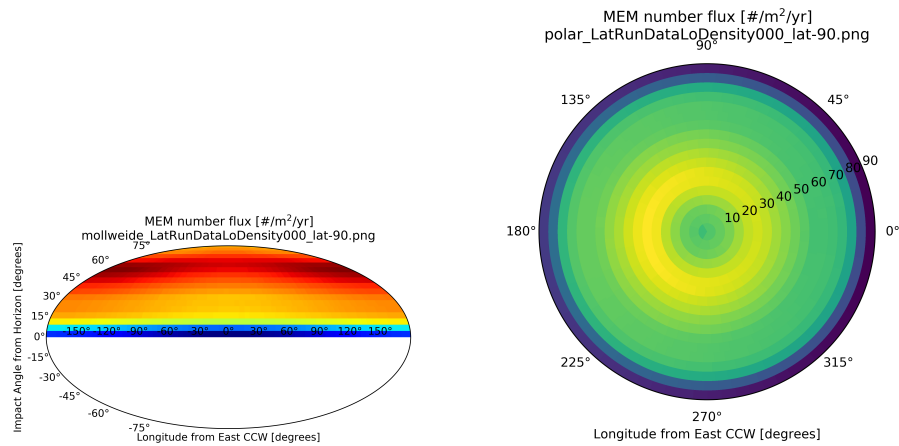


Figure 6: Fluxes at the meridional plane (as a function of impact speed and angle from the horizon) of the low density population (a) and (b), and the high density population (c) and (d) impacting the Moon at the equator (a) and (c), and the north/south pole (b) and (d).

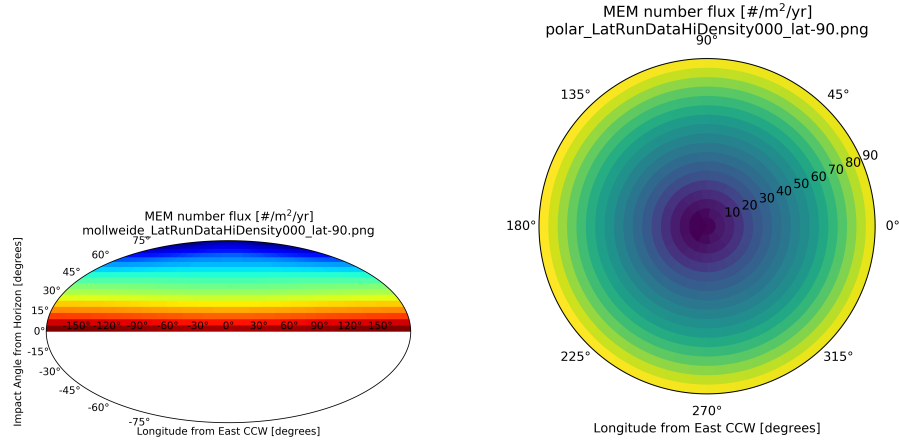
[Melosh \[2000\]](#), the probability of hitting a planetary body, regardless of the target's gravitational field, is given by

$$dP = 2 \sin \alpha \cos \alpha d\alpha, \quad (3.1)$$

where  $\alpha$  is the angle from zenith. This equation shows that the most probable impact angle is at  $45^\circ$ , which is not supported by the sporadic meteoroid fluxes, implying a non-isotropic origin – known to be the helion/anti-helion, toroidal, and apex sources.

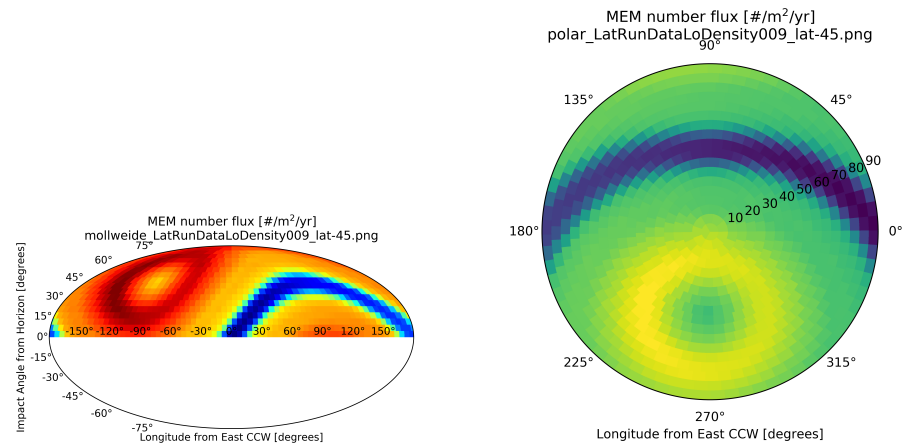


(a) Mollweide view of the low density population impacting at the south pole. (b) All-sky view of the low density population impacting at the south pole.

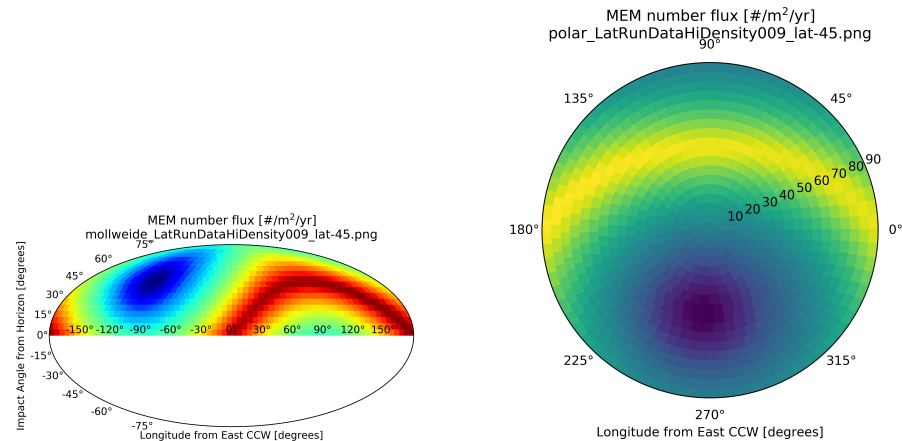


(c) Mollweide view of the high density population impacting at the south pole. (d) All-sky view of the high density population impacting at the south pole.

Figure 7: Fluxes at the meridional plane as a function of approaching angle for the low density population (a) and (b), and the high density population (c) and (d) impacting the Moon at the south pole in a Mollweide (a) and (c), and all-sky (b) and (d) projection.

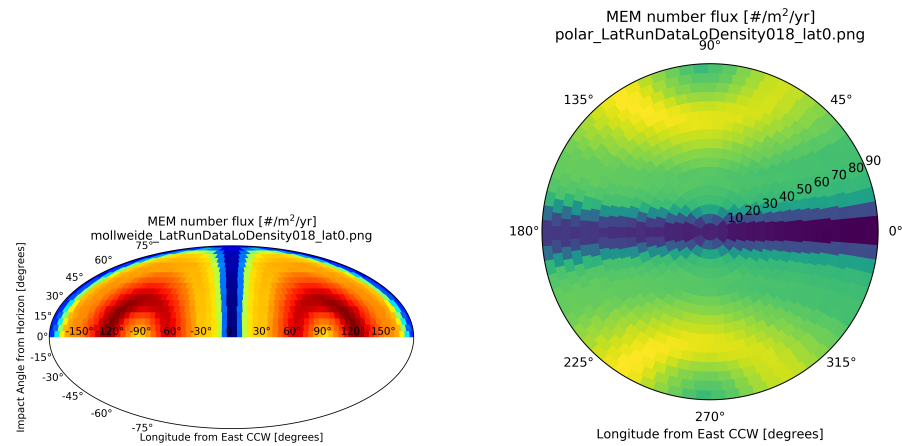


(a) Mollweide view of the low density population impacting at  $-45^\circ$  latitude. (b) All-sky view of the low density population impacting at  $-45^\circ$  latitude.

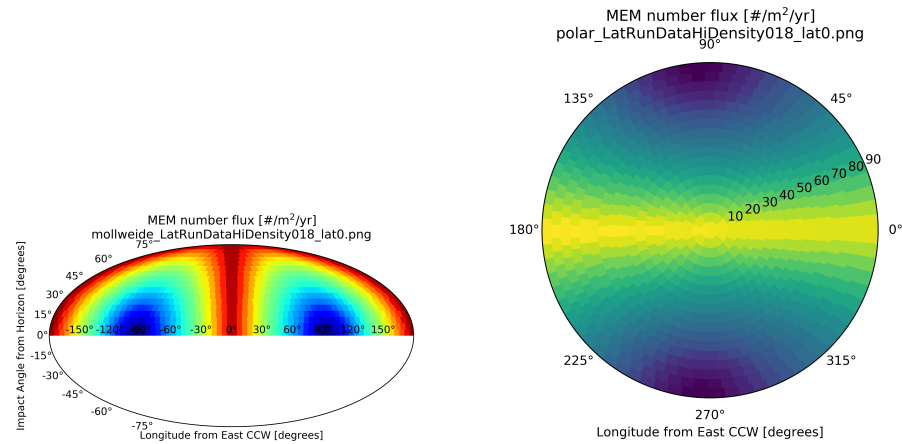


(c) Mollweide view of the high density population impacting at  $-45^\circ$  latitude. (d) All-sky view of the high density population impacting at the  $-45^\circ$  latitude.

Figure 8: Fluxes at the meridional plane as a function of approaching angle for the low density population (a) and (b), and the high density population (c) and (d) impacting the Moon at  $-45^\circ$  latitude in a Mollweide (a) and (c), and all-sky (b) and (d) projection.



(a) Mollweide view of the low density population impacting at the equator. (b) All-sky view of the low density population impacting at the equator.



(c) Mollweide view of the high density population impacting at the equator. (d) All-sky view of the high density population impacting at the equator.

Figure 9: Fluxes at the meridional plane as a function of approaching angle for the low density population (a) and (b), and the high density population (c) and (d) impacting the Moon at the equator in a Mollweide (a) and (c), and all-sky (b) and (d) projection.

### 3.2.2 Density Distribution

The meteoroid density has two components, a low and a high density contribution, as shown in Figure 10. The meteoroid density components can be written in terms of log-normal distributions

$$F_\delta(x) = \frac{A}{\sigma\sqrt{2\pi}x} \exp\left[-\frac{(\ln x - \mu_\delta)^2}{2\sigma^2}\right], \quad (3.2)$$

where the fit parameters for the low and high density components are shown in Figures 11 and 12.

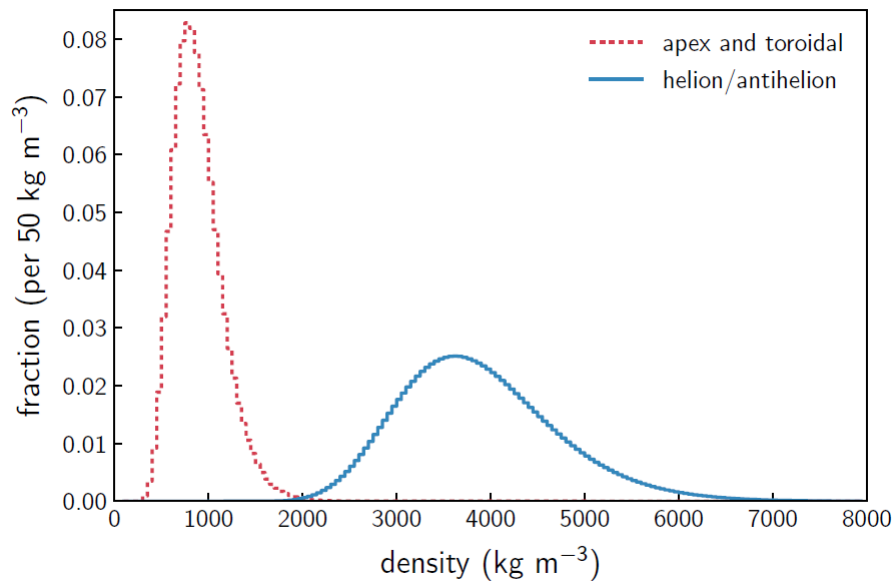


Figure 10: Meteoroid density distribution according to the MEM3 User Guide. The apex and toroidal meteoroid sources constitute the low-density population, while the helion/antihelion source constitutes the high-density population. Each set of densities follows a log-normal distribution [c.f. Figure 11, [Moorhead et al., 2019](#)].

```
[1/2/2020 5:16:00 PM      Plot: "Graph5"]
Non-linear fit of dataset: Table3_2, using function: log10(a/((10^x)*s*2.506628275)*exp(-(x*ln(10)-m)^2/(2*s^2)))
Y standard errors: Unknown
Scaled Levenberg-Marquardt algorithm with tolerance = 0.0001
From x = 2.097 to x = 3.902
a = 53.839135327051 +/- 0.82189223780795
s = 0.294917539134767 +/- 0.000210957288819632
m = 6.7346464600191 +/- 0.00131007263737737
-----
Chi^2 = 0.305039664208057
R^2 = 0.999894109124399
-----
Iterations = 0
Status = success
```

Figure 11: Non-linear fit of the low density profile in Figure 10 with Eq. 3.2 in SciDAVis, giving the constants for  $a \rightarrow A$ ,  $s \rightarrow \sigma$ , and  $m \rightarrow \mu_\delta$ .

```
[1/2/2020 5:19:18 PM      Plot: "Graph6"]
Non-linear fit of dataset: Table4_2, using function: log10(a/((10^x)*s*2.506628275)*exp(-(x*ln(10)-m)^2/(2*s^2)))
Y standard errors: Unknown
Scaled Levenberg-Marquardt algorithm with tolerance = 0.0001
From x = 2.096910013 to x = 3.901730692
a = 39.742506482046 +/- 1.58430260083343
s = 0.221066131940955 +/- 0.00039359322394943
m = 8.26026111215463 +/- 0.00352064330966803
-----
Chi^2 = 5.98458401110512
R^2 = 0.999293469696896
-----
Iterations = 0
Status = iteration is not making progress towards solution
```

Figure 12: Non-linear fit of the high density profile in Figure 10 with Eq. 3.2 in SciDAVis, giving the constants for  $a \rightarrow A$ ,  $s \rightarrow \sigma$ , and  $m \rightarrow \mu_\delta$ .

### 3.2.3 Mass Distribution

From the MEM3 User Guide, the  $g(m)$  flux of meteoroids larger than a limiting mass  $m$  is obtained, originally from [Grün et al. \[1985\]](#). The Grün interplanetary flux equation is given by

$$g(m) = (c_4 m^{\gamma_4} + c_5)^{\gamma_5} + c_6 (m + c_7 m^{\gamma_6} + c_8 m^{\gamma_7})^{\gamma_8} + c_9 (m + c_{10} m^{\gamma_9})^{\gamma_{10}}, \quad (3.3)$$

where the constants are  $c_4 = 2.2 \times 10^3$ ,  $c_5 = 15$ ,  $c_6 = 1.3 \times 10^{-9}$ ,  $c_7 = 10^{11}$ ,  $c_8 = 10^{27}$ ,  $c_9 = 1.3 \times 10^{-16}$ ,  $c_{10} = 10^6$ ; and the exponents are  $\gamma_4 = 0.306$ ,  $\gamma_5 = -4.38$ ,  $\gamma_6 = 2$ ,  $\gamma_7 = 4$ ,  $\gamma_8 = -0.36$ ,  $\gamma_9 = 2$ , and  $\gamma_{10} = -0.85$ . Equation 3.3 is applied to MEM's mass range and is shown in Figure 13.

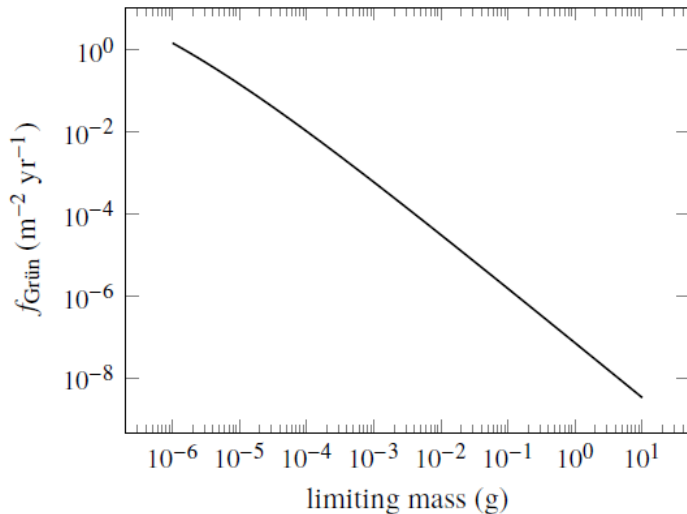


Figure 13: The Grün interplanetary meteoroid flux as a function of limiting particle mass [[Moorhead et al., 2019](#), Figure 1], normalized to 1 for a limiting mass equal to or greater than  $1\mu\text{g}$ .

## 3.3 Near-Earth Objects

The near-Earth objects (NEOs) described in this model consist of the small asteroids and comets between about 0.1 m and 1000 m diameter onto the lunar surface [[Moorhead, 2020](#)]. The speed and mass distributions (Sections 3.3.1 and 3.3.2) were based on [Brown et al. \[2002\]](#) and the Center for Near Earth Object Studies (CNEOS)<sup>7</sup>, respectively. Both of the data sources are kinetic-energy-limited and correspond to the impact flux at the Earth's atmosphere, translated to fluxes onto the lunar surface [[Moorhead, 2020](#)].

<sup>7</sup><https://cneos.jpl.nasa.gov/fireballs/>

### 3.3.1 Speed Distribution

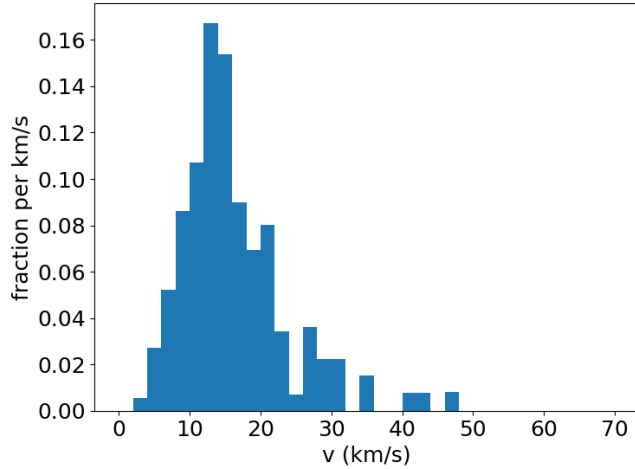


Figure 14: Mass-limited speed distribution at the lunar surface.

The speed distribution of NEO's is shown in Figure 14. The values (fraction of flux per bin) in each bin are midpoint values, where the bins have a size of  $2 \text{ km s}^{-1}$ . Note also that because the flux is a power law, this speed distribution is independent of limiting mass.

### 3.3.2 Mass Distribution

The mass-limited flux at the lunar surface can be shown to be [see, *Moorhead, 2020*]

$$g_{\mathbb{C}}(m) = 2.89 \times 10^{-11} \text{ m}^{-2} \text{ yr}^{-1} \cdot m^{-0.9}, \quad (3.4)$$

where  $m$  is the mass of the impactor in kg. Since the mass-limited flux has a power-law index greater than  $-1$ , a maximum impactor size should be defined. An example of quantifying the largest size could be by computing the size that would have an  $n$ -% chance of hitting the Moon in  $Y$  years. If  $n = 5\%$  and  $Y = 10$  years, then the largest size would be

$$\begin{aligned} m_{max,kg} &= \left( \frac{2.89 \times 10^{-11} \text{ m}^{-2} \text{ yr}^{-1} \cdot 3.793 \times 10^{13} \text{ m}^{-2} \cdot 10 \text{ yr}}{0.05} \right)^{1/0.9} \\ &= 2.4 \times 10^5 \text{ kg}. \end{aligned} \quad (3.5)$$

If the NEO density is assumed to be  $3.0 \text{ g/cm}^3$  (which is the assumption used throughout the model), then this corresponds to a diameter of  $5.3 \text{ m}$ .

### 3.4 Meteoroid Showers

The primary fluxes that originate from meteoroid showers can also produce ejecta. However, each different meteoroid shower has its own strength, duration, and time of year at which they occur. A prediction of the meteoroid shower fluxes as a function of time are compared to the sporadic meteoroids at different limiting energies, shown in Figure 15 [Moorhead et al., 2020].

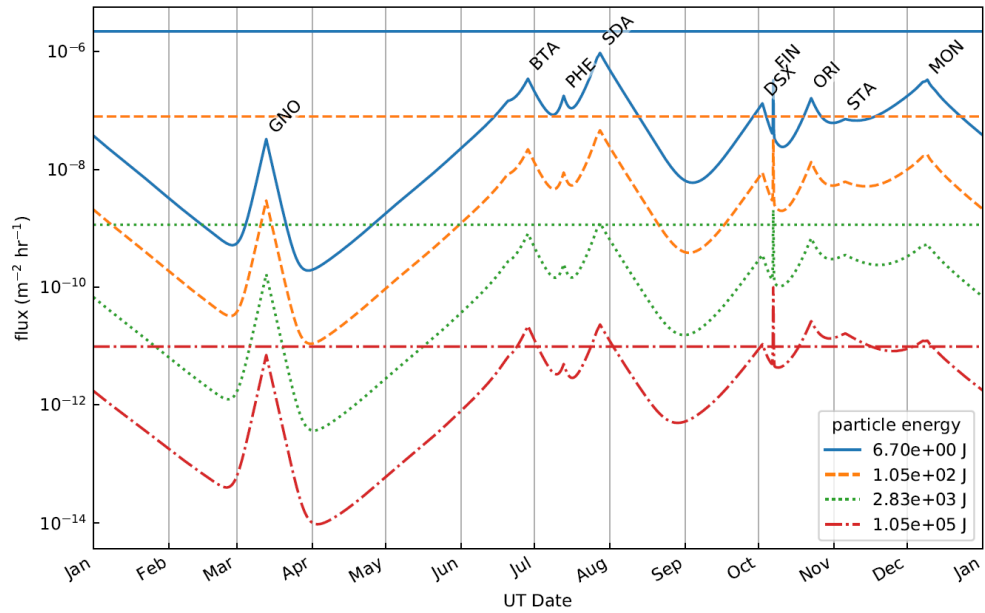


Figure 15: Meteor shower flux (variable lines) and sporadic meteoroid flux (horizontal lines) over the course of 2021. Fluxes are quoted to four limiting particle kinetic energies; these kinetic energies correspond to particles with diameters of 0.04 cm, 0.1 cm, 0.3 cm, and 1 cm, assuming a density of  $1 \text{ g cm}^{-3}$  and a speed of  $20 \text{ km s}^{-1}$ , [see Figure 1, Moorhead et al., 2020].

At this time, it is assumed that the ejecta produced by meteoroid showers is small compared to the ejecta produced by the sporadic meteoroids. Further investigation may be warranted, however, short-term ejecta environments may need to include meteoroid showers during a particularly strong shower. These operational environments would be created on an as-need basis for lunar surface EVAs, similar to forecasts for meteoroid showers for ISS EVAs.

## 4 Ejecta Flux from Impact Point

The ejected mass from an impact is distributed at different speeds (Section 4.1.1), angles (Sections 4.1.2 and 4.1.3), and sizes (Section 4.2). The speed and size of the ejecta is assumed to be dependent on each other – the larger the ejected particle the slower, on average, the particle that is ejected. The impactor impact angle and azimuth determines the zenith and azimuth distribution of the ejecta. For more oblique impacts, the ejecta is projected less from normal and more towards the horizon, in addition to having a stronger component downstream with respect to the impactor azimuth in terms of the ejecta azimuth distribution.

### 4.1 Ejecta Distribution

#### 4.1.1 Speed Distribution

The speed distribution of the ejecta is determined by the scaling laws [[Housen and Holsapple, 2011](#)] that are assumed in this model (see Section 5). As an approximation, the speed distribution can be described by a power-law distribution with an index that depends on the target material. However, a more complete speed distribution is used that not only includes a power-law regime, but includes proper cut-offs for the slowest speeds and fastest speeds.

#### 4.1.2 Zenith Distribution

##### 4.1.2.1 Peak Zenith Angle $\alpha_{max}$

The ejecta zenith distribution is typically peaked at some zenith angle  $\alpha_{max}$  that falls off at other angles. The peak zenith angle  $\alpha_{max}$  can have different dependencies on the impactor properties.

**Constant Zenith Peak:** The simplest case is a constant,  $\alpha_{max} = \alpha_0$ , typically taken as  $\alpha_0 = \pi/4$ . For relatively close impact distances, an ejected angle of 45° gives the most efficient ejecta – the ejecta travels further for a given speed.

**Impact Angle Dependent Zenith Peak:** To include more information into the ejecta blanket from the impactor is to have the zenith peak as a function of the impact angle,  $\alpha_{max} = \alpha_{max}(\alpha_i)$ , where  $\alpha_i$  is the impact angle of the impactor. For simplicity, the peak zenith angle can be taken as the downstream for all azimuth, given in Equation (4.1).

**Impact Angle & Azimuth Dependent Zenith Peak:** An increased fidelity peak zenith angle also include information about the impactor azimuth angle,  $\alpha_{max} = \alpha_{max}(\alpha_i, \beta_i)$ , where  $\beta_i$  is the impact azimuth.

The peak zenith angle can be modeled after experiments of oblique impacts following Figure 18 of [Gault and Wedekind \[1978\]](#) as a proxy to the model of  $\alpha_{max}$ . Using

a third-order polynomial for both fits to the downstream and upstream angles given in Table 4, the peak zenith angles downstream and upstream are given by

$$\alpha_{max}(\beta - \beta_i = 0) = 0.0003\alpha_i^3 - 0.036\alpha_i^2 + 1.5206\alpha_i + 20, \text{ downstream} \quad (4.1)$$

$$\alpha_{max}(\beta - \beta_i = \pi) = -0.00042\alpha_i^3 + 0.0236\alpha_i^2 + 0.129\alpha_i + 20, \text{ upstream} \quad (4.2)$$

in units of degrees, where  $\beta$  is the ejecta azimuth. When both the impact and ejecta azimuth angles are in the same direction (i.e.,  $\beta - \beta_i = 0$ ), this is downstream.

Table 4: Cone angles of upstream and downstream of impact derived from Figure 18 of *Gault and Wedekind [1978]*.

Impact Zenith Angle	Upstream Zenith Angle	Downstream Zenith Angle
0	20	20
15	24	35
30	35	45
45	28	40
60	13	54
75	-35	66

#### 4.1.2.2 Rival & Mandeville (Gaussian Distribution)

One example of a peaked distribution is given in *Rival and Mandeville [1999]*, shown below for reference:

$$F(\alpha) = \frac{1}{\sigma\sqrt{2\pi}} \exp\left[-\frac{(\alpha - \alpha_{max})^2}{2\sigma^2}\right], \quad (4.3)$$

where  $\alpha_{max}$  is defined as

$$\alpha_{max} = \begin{cases} \frac{\alpha_{max60} - \alpha_{max0}}{\pi/3} \alpha_i + \alpha_{max0} & \text{for } \alpha_i \leq \pi/3 = 60^\circ \\ \alpha_{max60} & \text{for } \alpha_i > \pi/3 = 60^\circ \end{cases}, \quad (4.4)$$

for  $\alpha_i$  the impact zenith angle, and [see *Miller, 2017*]

$$\alpha_{max0} = \frac{\pi}{6} = 30^\circ, \quad (4.5)$$

$$\alpha_{max60} = \frac{4\pi}{9} = 80^\circ, \quad (4.6)$$

$$\sigma = \frac{\pi}{60} = 3^\circ, \quad (4.7)$$

where the peak ejecta angle is shifted from  $30^\circ$  of zenith for a normal impact to  $80^\circ$  of zenith for oblique impacts ( $> 60^\circ$ ).

One difficulty with this zenith distribution is the normalization, assuming ejecta is only created from  $0 < \alpha < \pi/2$ . A Gaussian distribution is usually integrated from  $-\infty$  to  $+\infty$ , so a finite integration introduces error functions.

#### 4.1.2.3 Raised Cosine Distribution

A more focused zenith distribution that is easier to normalize can be described by a raised cosine distribution, given as

$$F(\alpha) = \begin{cases} \frac{1}{2s} [1 + \cos\left(\frac{\alpha-\mu}{s}\pi\right)], & \text{for } \mu - s \leq \alpha \leq \mu + s \\ 0, & \text{otherwise} \end{cases}, \quad (4.8)$$

This distribution is symmetric about the peak  $\mu$ , with a spread  $s$ . It is assumed that  $\mu - s \geq 0$  and  $\mu + s \leq \pi/2$ , otherwise the normalization term would be dependent on the peak, in addition to the spread.

#### 4.1.3 Azimuth Distribution

The azimuth distribution is often dependent on the impactor azimuth such that there are more ejecta downstream for oblique impacts. Normal impacts are expected to produce a symmetric azimuth distribution. For highly oblique impacts ( $\alpha_i > \pi/3$ ) there is often seen a *butterfly pattern* [Shuvalov, 2011]. However, over a large number of oblique impacts of various sizes, it is plausible to assume that the direct downstream direction dominates the azimuth distribution.

##### 4.1.3.1 Rival & Mandeville

An example azimuth distribution can be found in *Rival and Mandeville* [1999], given by

$$G(\beta) = \begin{cases} \frac{1}{2\pi} \left[ 1 + \frac{3\alpha_i}{2\pi - 3\alpha_i} \cos(\beta - \beta_i) \right] & \text{for } \alpha_i \leq \pi/3 = 60^\circ \\ \frac{1}{\sigma' \sqrt{2\pi}} \exp\left[-\frac{(\beta - \beta_i)^2}{2\sigma'^2}\right] & \text{for } \alpha_i > \pi/3 = 60^\circ \end{cases}, \quad (4.9)$$

where

$$\sigma' = \frac{\pi}{36} = 5^\circ, \quad (4.10)$$

for  $\beta_i$  the impact azimuth angle  $+ \pi$ .

##### 4.1.3.2 Variation on Rival & Mandeville

In order to have a periodic and easy-to-normalize function, the oblique regime is modified from Equation (4.9) to give

$$G(\beta) = \begin{cases} \frac{1}{2\pi} \left[ 1 + \frac{3\alpha_i}{2\pi - 3\alpha_i} \cos(\beta - \beta_i) \right] & \text{for } \alpha_i \leq \pi/3 = 60^\circ \\ \frac{1 + \cos(\beta - \beta_i)}{2\pi} & \text{for } \alpha_i > \pi/3 = 60^\circ \end{cases}. \quad (4.11)$$

An alteration of Equation (4.11) on the oblique case could be to use a raised cosine distribution with a spread of  $s = 3\sigma'$ .

## 4.2 Mass/Particle Size Distribution

The mass or particle size distribution of ejecta can be approximated in a few different ways. For the purpose of comparing to various sources, there are four possible ways to describe the particle size distribution, give by [Koschny and Grün, 2001]

$$m_{cum}(\leq d) = k_1 d^\alpha, \quad (4.12)$$

$$N_{cum}(\geq m) = k_2 m^{-\beta}, \quad (4.13)$$

$$N_{cum}(\geq d) = k_3 d^\gamma, \quad (4.14)$$

$$m_{cum}(\leq m) = k_4 m^\delta, \quad (4.15)$$

with  $N_{cum}$  the cumulative number,  $m_{cum}$  the cumulative mass,  $d$  the particle diameter, and  $m$  the particle mass.

The various transformations between the four possible descriptions are:

$$\beta = -\gamma/3, \quad (4.16)$$

$$\alpha = 3(1 - \beta), \quad (4.17)$$

$$\alpha = \gamma + 3, \quad (4.18)$$

$$\delta = \alpha/3. \quad (4.19)$$

Table IV of [Koschny and Grün, 2001] gives examples of the exponent  $\alpha$ , summarized here in Table 5.

Table 5: A compilation of indices of the various particle size distribution descriptions. Values that are in bold are the index that was originally used in the corresponding source.

Target Material	Source	$\alpha$	$\beta$	$-\gamma$
Basalt	Koschny and Grün [2001]	<b>0.56, 0.96</b>	0.81, 0.68	2.44, 2.04
Granite	"	<b>0.44</b>	0.85	2.56
Gabbro	"	<b>1.41</b>	0.53	1.59
Alumina	"	<b>1.08</b>	0.64	1.92
Water ice	"	<b>1.3</b>	0.57	1.7
Porous ice-silicate	"	<b>1.8</b>	0.4	1.2
Compact ice-silicate	"	<b>1.4±0.3</b>	0.53±0.1	1.6±0.3
Basalt	Cour-Palais [1969]	-0.6	<b>1.2</b>	3.6
Sandstone	Buhl et al. [2014]	0.26-0.46	0.85-0.91	<b>2.54-2.74</b>
Apollo Samples	Carrier III [2003]	-0.55	1.18	<b>3.55<sup>a</sup></b>
Basalt + others	O'Keefe and Ahrens [1985]	<b>0.42-0.53</b>	0.82-0.86	2.47-2.58

<sup>a</sup> valid for diameters from  $10^{-6}$  m to  $10^{-1}$  m.

### 4.2.1 NASA SP-8013

The Meteoroid Environment Model - 1969 Near Earth to Lunar Surface [Cour-Palais, 1969], or NASA SP-8013, contains both the primary meteoroid environment as well

as the lunar ejecta environment. The latter is given in terms of cumulative number flux of secondary ejecta greater than mass  $m$  (i.e., in the form of Equation (4.13)), shown in Figure 16 (Figure 10 of [Cour-Palais \[1969\]](#)).

Each of the three velocity intervals have a power-law index of  $-\beta = -1.2$ , corresponding to  $\alpha = -0.6$  (see Table 5). Qualitatively, the larger the power-law index  $\alpha$  is, the greater number of larger particles are present in the size distribution [e.g., [Koschny and Grün, 2001](#); [Bierhaus et al., 2018](#)]. For a negative  $\alpha$ , this implies an absence of larger sized particles in the SP-8013 model compared to what is shown in [Koschny and Grün \[2001\]](#).

The power-law index of  $-\beta = -1.2$  is a simplification of [Zook \[1967\]](#), which is what the SP-8013 is based on for lunar ejecta. Figure 5 of [Zook \[1967\]](#) displays three different velocity ranges with  $\beta = 1$  for  $0 \leq v \leq 100$  m/s,  $\beta = 1$  for  $100 \leq v \leq 250$  m/s, and  $\beta = 1.16$  for  $250 \leq v \leq 1000$  m/s.

It is interesting to point out that the particle size distribution shown in Figure 16 has a similar power-law index with the regolith particle size distribution of diameters from  $10^{-6}$  m to  $10^{-1}$  m of [Carrier III \[2003\]](#), see Table 5. Since the regolith particle size distribution is a log-normal distribution, the power-law index for larger diameters will be even more steep, and therefore a more negative  $\alpha$ , meaning there is an absence of larger stones or boulders in the top layers of regolith sampled from Apollo.

#### 4.2.2 O'Keefe & Ahrens 1985

A conclusion from [Sachse et al. \[2015\]](#) states that *the assumption that the size of the fragments and the speed at the moment of ejection are uncorrelated* should be dropped. In practice, larger ejected particles typically have slower speeds while smaller ejected particles have faster speeds. This observation is not seen in the previous size distribution model of NASA SP-8013<sup>8</sup>, so another model is sought after.

The particle size distribution discussed in [O'Keefe and Ahrens \[1985\]](#) gives a way to introduce a speed-dependent particle size distribution. The cumulative amount of mass of ejecta fragments of mass greater than  $m$  is given by (Equation (11) of [O'Keefe and Ahrens \[1985\]](#)), note  $\beta_{OK85} \equiv \alpha$  as in Table 5,

$$f(m, m_{bv}(v)) = 1 - \left( \frac{m}{m_{bv}} \right)^{\frac{\beta_{OK85}}{3}}, \quad (4.20)$$

where the mass of the largest fragment ejected at a given ejected velocity  $v$  is

$$\frac{m_{bv}(v)}{m_b} = \left( \frac{v}{v_{min}} \right)^{-\delta_{OK85}}. \quad (4.21)$$

The speed index  $\delta_{OK85}$  is related to the power-law index of the CDF of mass exceeding a certain speed of ejecta (e.g.,  $3\mu$  from [Housen and Holsapple \[2011\]](#)) and the CDF of mass not exceeding a certain diameter, i.e.  $\alpha$ , given by

$$\delta_{OK85} = \frac{9\mu}{\alpha}. \quad (4.22)$$

---

<sup>8</sup>It is important to note that [Zook \[1967\]](#) did include a speed dependent size distribution in their model (they looked at three variations, ultimately using a piece-wise power-law model), however, [Cour-Palais \[1969\]](#) in SP-8013 simplified the size distribution to be constant for each of the speed ranges.

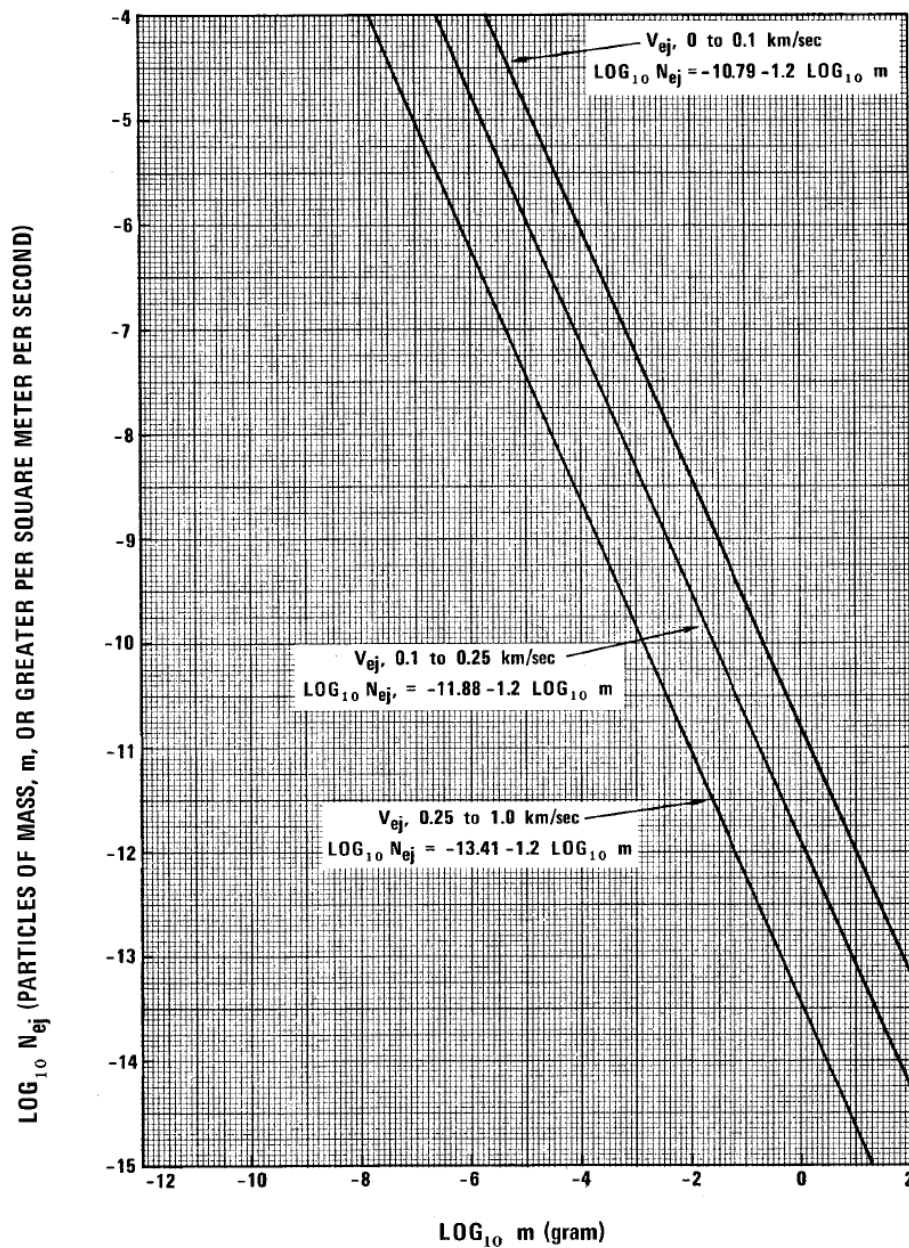


Figure 16: Average cumulative lunar ejecta flux-mass distribution for each of three ejecta velocity intervals [[Cour-Palais, 1969](#)].

The minimum velocity  $v_{min}$  is defined as the minimum speed at which an ejected particle can reach the rim of a crater from the bottom of the crater,

$$v_{min} = 2\sqrt{\frac{gR}{K}}, \quad (4.23)$$

where  $g$  is the lunar gravitational constant,  $R$  is the crater radius (see Section 5.1), and  $K$  is the crater diameter-to-depth ratio which typically varies between 5 and 20.

The maximum fragmentation mass is given in *O'Keefe and Ahrens* [1985] as

$$m_b = 0.2M_{tot}^{0.8}, \quad (4.24)$$

where  $M_{tot}$  is the total mass ejected from the crater by an impactor in grams, see Section 5.2. On the other hand, *Koschny and Grün* [2001] have a more conservative estimate on the maximum fragmentation mass with

$$m_b = 0.01M_{tot}. \quad (4.25)$$

#### 4.2.3 Mass Distribution with Speed Distribution Weighting

Starting with the definition described by *O'Keefe and Ahrens* [1985] of the cumulative ejecta mass distribution as a function of the ejecta speed  $f(m, m_{bv}(v))$  (Equation (4.20)), the ejecta mass distribution is found by taking the derivative with respect to the mass,

$$-\frac{df(m, m_{bv}(v))}{dm} = \frac{\beta}{3m_{bv}} \left( \frac{m}{m_{bv}} \right)^{\frac{\beta}{3}-1}. \quad (4.26)$$

The complete ejecta mass distribution for a given impact is computed by taking the ejecta mass distribution for a given ejecta speed (Equation (4.26)) and convoluting it with the ejected mass per speed (i.e., the speed distribution, Equation (5.3)),

$$f_c(m_{ej}) = - \int_{v_{min}}^{v_{max}(m_{ej})} dv \frac{df}{dm} \frac{dM}{dv}, \quad (4.27)$$

where the upper limit is (specifying  $m_{ej}$  as the ejecta mass as opposed to the impactor mass  $m_{imp}$ )

$$v_{max}(m_{ej}) = \min \left[ v_{min}(m_{ej}/m_b)^{-1/\delta}, v_{max} \right], \quad (4.28)$$

and making the change of variables to the location from the center of the crater  $x$  from the speed  $v$ , (note,  $x = n_2 R y$ )

$$f_C(m) = \int_{x(v_{max}(m))}^{x(v_{min})} dx \frac{df}{dm} \frac{dM}{dx}, \quad (4.29)$$

$$\begin{aligned} &= A_C \left( \frac{m_{ej}}{m_b} \right)^{\frac{\beta}{3}-1} \int_{\frac{x(v_{max}(m))}{n_2 R}}^{\frac{x(v_{min})}{n_2 R}} dy y^{-\frac{\beta\delta}{3\mu}+2} (1-y)^{\frac{\beta\delta p}{3}}, \\ &= A_C \left( \frac{m_{ej}}{m_b} \right)^{\frac{\beta}{3}-1} \left\{ \beta \left[ \frac{x(v_{min})}{n_2 R}; -\frac{\beta\delta}{3\mu} + 3, \frac{\beta\delta p}{3} + 1 \right] \right. \\ &\quad \left. - \beta \left[ \frac{x(v_{max}(m_{ej}))}{n_2 R}; -\frac{\beta\delta}{3\mu} + 3, \frac{\beta\delta p}{3} + 1 \right] \right\}, \end{aligned} \quad (4.30)$$

where the constants with respect to  $m_{ej}$  are

$$A_C = \frac{3k\beta}{4\pi} \frac{m_{imp}}{m_b} \left( \frac{\rho}{\delta} \right)^{-\frac{\beta\delta\nu}{\mu}+1} \left( \frac{C_1 U}{v_{min}} \right)^{\frac{\beta\delta}{3}} \left( \frac{a}{n_2 R} \right)^{\frac{\beta\delta}{3\mu}-3}, \quad (4.31)$$

with  $\beta(z; a, b)$  as the incomplete beta function,  $a$  is the projectile radius,  $R$  is the crater radius (Equation (5.1) or (5.2)), and the scaling law parameters  $n_1$ ,  $n_2$ ,  $p$ ,  $\mu$ ,  $\nu$ ,  $k$ , and  $C_1$  are found in Table 6. Additional constants  $\beta$  and  $\delta$  can be found in Section 4.2.2.

### 4.3 Total Kinetic Energy

The kinetic energy of the impactor gets converted into many forms during the cratering process; heat, light, compression, phase changing, and kinetic energy to the ejecta. In this section, the total energy imparted to the ejecta is computed.

The total kinetic energy of the ejecta  $E_{tot,ej}$  can be calculated by taking the second moment of the ejecta mass distribution as

$$E_{tot,ej} = \frac{1}{2} \int_0^{v_{max}} dv \left( -\frac{dM}{dv} \right) v^2, \quad (4.32)$$

where the ejecta mass distribution  $dM/dv$  is defined as Equation (5.9) and explicitly given in Equation (5.12), and the ejecta speed  $v$  in terms of the crater parameters (Equation (5.3)).

Changing variables from ejecta speed  $v$  to location in the crater  $x$ , the total ejecta

kinetic energy is<sup>9</sup>

$$E_{tot,ej} = \frac{1}{2} \int_{n_2 R}^{n_1 a} dx \left( -\frac{dM}{dx} \right) v(x)^2, \quad (4.33)$$

$$= \frac{3}{2} M_{tot} v_{max}^2 \frac{\left(1 - \frac{n_1 a}{n_2 R}\right)^{-2p}}{1 - \left(\frac{n_1 a}{n_2 R}\right)^3} \int_{n_1 a}^{n_2 R} \frac{dx}{n_2 R} \left(\frac{x}{n_1 a}\right)^{-\frac{2}{\mu}} \left(\frac{x}{n_2 R}\right)^2 \left(1 - \frac{x}{n_2 R}\right)^{2p},$$

$$= \frac{3}{2} M_{tot} v_{max}^2 \frac{\left(1 - \frac{n_1 a}{n_2 R}\right)^{-2p} \left(\frac{n_1 a}{n_2 R}\right)^{\frac{2}{\mu}}}{1 - \left(\frac{n_1 a}{n_2 R}\right)^3} \beta \left( \frac{x}{n_2 R}; -\frac{2}{\mu} + 3, 2p + 1 \right) \Big|_{x=n_1 a}^{x=n_2 R},$$

$$= \frac{3}{2} M_{tot} v_{max}^2 \frac{\left(1 - \frac{n_1 a}{n_2 R}\right)^{-2p} \left(\frac{n_1 a}{n_2 R}\right)^{\frac{2}{\mu}}}{1 - \left(\frac{n_1 a}{n_2 R}\right)^3} \beta \left( 1 - \frac{n_1 a}{n_2 R}; 2p + 1, -\frac{2}{\mu} + 3 \right), \quad (4.34)$$

where  $M_{tot}$  is the total mass ejected from the crater (Equation (5.6)),  $v_{max}$  is the maximum ejecta speed for the particular crater (Equation (5.5)),  $a$  is the projectile radius,  $R$  is the crater radius (Equation (5.1) or (5.2)), and the scaling law parameters  $n_1$ ,  $n_2$ ,  $p$ ,  $\mu$ ,  $\nu$ ,  $k$ , and  $C_1$  are found in Table 6. Also note,  $\beta(z; a, b)$  is the incomplete beta function<sup>10,11</sup>. The total ejecta energy can also be written in terms of the impactor mass  $m$  and normal component of the impactor speed  $U$

$$E_{tot,ej} = \frac{9kC_1^2}{8\pi} \left(\frac{\rho}{\delta}\right)^{-\frac{2\nu}{\mu}+1} \left(\frac{a}{n_2 R}\right)^{\frac{2}{\mu}-3} \beta \left( 1 - \frac{n_1 a}{n_2 R}; 2p + 1, -\frac{2}{\mu} + 3 \right) m U^2, \quad (4.35)$$

where  $\rho$  is the target bulk density and  $\delta$  is the impactor density.

An example of Equation (4.35) is shown in Figures 17 and 18. The effect of the choice of surrogate material for the regolith can be seen in the differences between these two figures. The Weakly cemented basalt in Figure 18 compared with the sand fly ash in Figure 17 has about a factor of 8 less kinetic energy transferred from the impactor to the ejected material. The work of [Hartmann \[1985\]](#) (Table II) provides experimental estimates of the estimated fraction of impact energy in ejecta.

---

<sup>9</sup>Note,  $\beta(1 - x; b, a) = \beta(1; a, b) - \beta(x; a, b)$ .

<sup>10</sup><https://functions.wolfram.com/GammaBetaErf/Beta3/>

<sup>11</sup>Do not use the regularized incomplete beta function implementations. Use the Gauss hypergeometric function  ${}_2F_1$  representation instead to avoid issues when the second parameter is a negative integer.

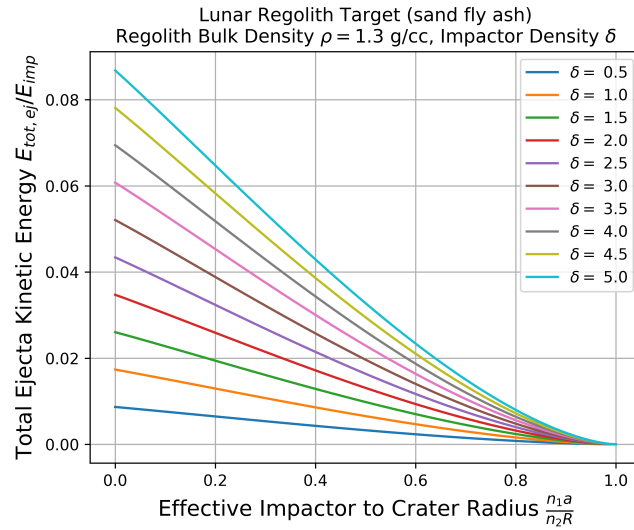


Figure 17: The total ejecta kinetic energy  $E_{tot,ej}$  (Equation (4.35)) over impactor energy  $E_{imp} = \frac{1}{2}mU^2$  vs. effective impactor to crater radius  $\frac{n_1a}{n_2R}$  for a lunar regolith target (using SFA in Table 6) with regolith surface bulk density  $\rho = 1.3$  g/cc and varying impactor densities.

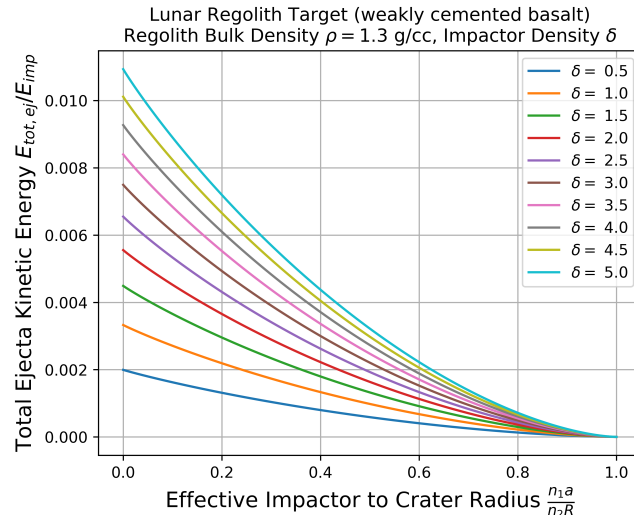


Figure 18: The total ejecta kinetic energy  $E_{tot,ej}$  (Equation (4.35)) over impactor energy  $E_{imp} = \frac{1}{2}mU^2$  vs. effective impactor to crater radius  $\frac{n_1a}{n_2R}$  for a lunar regolith target (using WCB in Table 6) with regolith surface bulk density  $\rho = 1.3$  g/cc and varying impactor densities.

## 4.4 Orbital Mechanics

Particles that are ejected from the crater are assumed to follow projectile motion in a monopolar gravitational field with no external forces. The equations of motion<sup>12</sup> the ejecta particles trace are defined by the semi-major axis  $a$  and eccentricity  $e$  given by

$$a = \frac{1}{\frac{2}{r} - \frac{v^2}{GM}}, \quad (4.36)$$

$$e^2 = \left( \frac{rv^2}{GM} - 1 \right)^2 \sin^2 \gamma + \cos^2 \gamma, \quad (4.37)$$

for  $r$  the orbit position from the gravitating body's center,  $v$  the orbit speed,  $\gamma$  the local zenith angle with respect to the local horizon,  $G = 6.67408 \times 10^{-11} \text{ m}^3 \text{kg}^{-1} \text{s}^{-2}$  the gravitational constant, and  $M = 7.34767 \times 10^{22} \text{ kg}$  the mass of the Moon.

The escape speed of the Moon is defined as

$$v_{esc} = \sqrt{\frac{2GM}{r_m}}, \quad (4.38)$$

where  $r_m = 1.7374 \times 10^6 \text{ m}$  is the radius of the Moon, so that  $v_{esc} = 2.376 \text{ km s}^{-1}$ . Inserting Equation (4.38) into Equations (4.36) and (4.37) gives

$$a = \frac{r_m/2}{\frac{r_m}{r} - \frac{v^2}{v_{esc}^2}}, \quad (4.39)$$

$$e^2 = \left( \frac{2rv^2}{r_m v_{esc}^2} - 1 \right)^2 \sin^2 \gamma + \cos^2 \gamma. \quad (4.40)$$

If the definitions of  $a$  and  $e$  are at a point on the surface of the Moon,  $r = r_m$ , then Equations (4.39) and (4.40) become

$$a = \frac{r_m/2}{1 - \frac{v_p^2}{v_{esc}^2}}, \quad (4.41)$$

$$e^2 = \left( \frac{2v_p^2}{v_{esc}^2} - 1 \right)^2 \sin^2 \gamma_p + \cos^2 \gamma_p. \quad (4.42)$$

The position  $r$  of the ejected particle in its orbit is given by

$$r = \frac{a(1 - e^2)}{1 + e \cos \beta}, \quad (4.43)$$

where  $\beta$  is the true anomaly or angle from the periapsis point. An angle of  $\beta = 0$  would be a particle at the periapsis and an angle of  $\beta = \pi$  would be a particle at the apoapsis point.

---

<sup>12</sup>E.g., see <http://www.braeunig.us/space/orbmech.htm>.

In terms of the true anomaly  $\beta$ , the local zenith angle of the particle is given by

$$\tan \gamma = \frac{1 + e \cos \beta}{e \sin \beta}. \quad (4.44)$$

In the following two sections, the initial/final speeds  $v_p$  and  $v_s$ , the final zenith angle  $\gamma_s$ , and the final position in the orbit at the asset  $r_s$  will be computed. Section 4.4.1 will be a special case where the final impact point at the asset is at the surface of the Moon and Section 4.4.2 will assume a more general case of an arbitrary position on or above the Moon for the asset.

#### 4.4.1 Crater on Surface to Asset at Surface

The position in the orbit from the crater is the same radius is that of the asset at the surface, which says that the angle of periapsis at the crater impact is  $\beta_p$  and at the asset is  $\beta_s = -\beta_p$ . Therefore, the selenographic distance between the two points is

$$\frac{D}{r_m} = \beta_s - \beta_p, \quad (4.45)$$

$$= 2(\pi - \beta_p), \quad (4.46)$$

and solving for  $\beta_p$ ,

$$\beta_p = \pi - \frac{D}{2r_m}. \quad (4.47)$$

##### 4.4.1.1 Distance $D$ vs. $v_p$ and $\gamma_p$

Solving Equation (4.43) for  $\cos \beta_p$  and also  $\sin \beta_p$ , making use of  $a$  and  $e$  defined at the crater point (Equations (4.41) and (4.42)):

$$e \cos \beta_p = 2 \frac{v_p^2}{v_{esc}^2} \sin^2 \gamma_p - 1, \quad (4.48)$$

$$e \sin \beta_p = 2 \frac{v_p^2}{v_{esc}^2} \sin \gamma_p \cos \gamma_p. \quad (4.49)$$

Therefore, taking the tangent<sup>13</sup> and plugging in Equation (4.47), (c.f., Equation (1) of Vickery [1986])

$$\tan \left( \frac{D}{2r_m} \right) = \frac{2 \frac{v_p^2}{v_{esc}^2} \sin \gamma_p \cos \gamma_p}{1 - 2 \frac{v_p^2}{v_{esc}^2} \sin^2 \gamma_p}. \quad (4.50)$$

The distance at which the ejecta reaches apoapsis can be found by substituting  $D = 2D_{ap}$  into Equation (4.50).

---

<sup>13</sup>Note,  $\tan(\pi - \eta) = -\tan \eta$ .

#### 4.4.1.2 Initial Speed $v_p$ vs. $D$ and $\gamma_p$

The initial speed  $v_p$  can be solved for, giving

$$\frac{v_p}{v_{esc}} = \frac{1}{\sqrt{1 - \cos(2\gamma_p) + \sin(2\gamma_p) \cot\left(\frac{D}{2r_m}\right)}}. \quad (4.51)$$

#### 4.4.1.3 Initial Zenith Angle $\gamma_p$ vs. $D$ and $v_p$

The initial zenith angle  $\gamma_p$  can also be solved for by expanding  $\cos(2\gamma_p)$  and  $\sin(2\gamma_p)$  in terms of  $\cot \gamma_p$ ,

$$1 - \cos(2\gamma_p) = \frac{2}{1 + \cot^2 \gamma_p}, \quad (4.52)$$

$$\sin(2\gamma_p) = \frac{2 \cot \gamma_p}{1 + \cot^2 \gamma_p}, \quad (4.53)$$

such that

$$\cot \gamma_p = \frac{v_p^2}{v_{esc}^2} \cot\left(\frac{D}{2r_m}\right) \pm \sqrt{\frac{v_p^4}{v_{esc}^4} \cot^2\left(\frac{D}{2r_m}\right) + 2 \frac{v_p^2}{v_{esc}^2} - 1}. \quad (4.54)$$

The plus case gives  $\gamma_p \leq \gamma_{p,opt}$  and the minus case gives  $\gamma_p \geq \gamma_{p,opt}$ .

#### 4.4.1.4 Minimum Initial Zenith Angle $\gamma_{p,min}$ vs. $D$

To find the minimum initial zenith angle  $\gamma_{p,min}$ , the initial speed approaches the escape speed  $v_p \rightarrow v_{esc}$  in Equation (4.54) and simplifying (taking the positive case),

$$\gamma_{p,min} = \frac{D}{4r_m}. \quad (4.55)$$

#### 4.4.1.5 Maximum Distance $D_{max}$ vs. $v_p$

The maximum distance  $D_{max}$  a particle can travel at a given speed and optimal zenith angle is found by taking the discriminant in Equation (4.54) and setting it equal to zero such that

$$\tan\left(\frac{D_{max}}{2r_m}\right) = \pm \frac{v_p^2/v_{esc}^2}{\sqrt{1 - 2v_p^2/v_{esc}^2}} \quad (4.56)$$

where the direct path is the positive case, and the indirect path is the negative case with modding the tangent argument by  $\pi$ .

#### 4.4.1.6 Minimum Initial Speed $v_{p,min}$ vs. $D$

The minimum speed  $v_{p,min}$  at which to travel a certain distance is found by solving for  $v_p$  in Equation (4.56), giving

$$\frac{v_{p,min}^2}{v_{esc}^2} = + \tan\left(\frac{D}{2r_m}\right) \tan\left(\frac{\pi}{4} - \frac{D}{4r_m}\right), \quad (4.57)$$

for  $D \leq \pi r_m$ . For further distances, the limiting minimum speed is  $v_{p,min}/v_{esc} = \sqrt{2}/2$ .

#### 4.4.1.7 Optimal Initial Zenith Angle $\gamma_{p,opt}$ vs. $D$

The optimal initial zenith angle  $\gamma_{p,opt}$  follows as<sup>14</sup>

$$\gamma_{p,opt} = \frac{\pi}{4} + \frac{D}{4r_m}, \quad (4.58)$$

for  $D \leq \pi r_m$ . For further distances, the limiting optimal angle is  $\gamma_{p,opt} = \pi/2$ . At very small distances  $D \ll r_m$ , the optimal angle is  $\sim 45^\circ$  as expected.

#### 4.4.1.8 Final Speed $v_s$ and Zenith Angle $\gamma_s$

Due to the symmetry of the orbit points, the final speed and zenith angle<sup>15</sup> are given by

$$v_s = v_p, \quad (4.59)$$

$$\gamma_s = \gamma_p. \quad (4.60)$$

---

<sup>14</sup>Note that  $\arctan(\cot(\theta)) = \pi/2 - \theta$  for  $0 \leq \theta \leq \pi$ .

<sup>15</sup>The final zenith angle is taken as the observed incoming angle, not the angle at which the ejecta is going. This introduces a different of  $\pi$  radians.

#### 4.4.1.9 Visualizing Ejecta in Phase Space

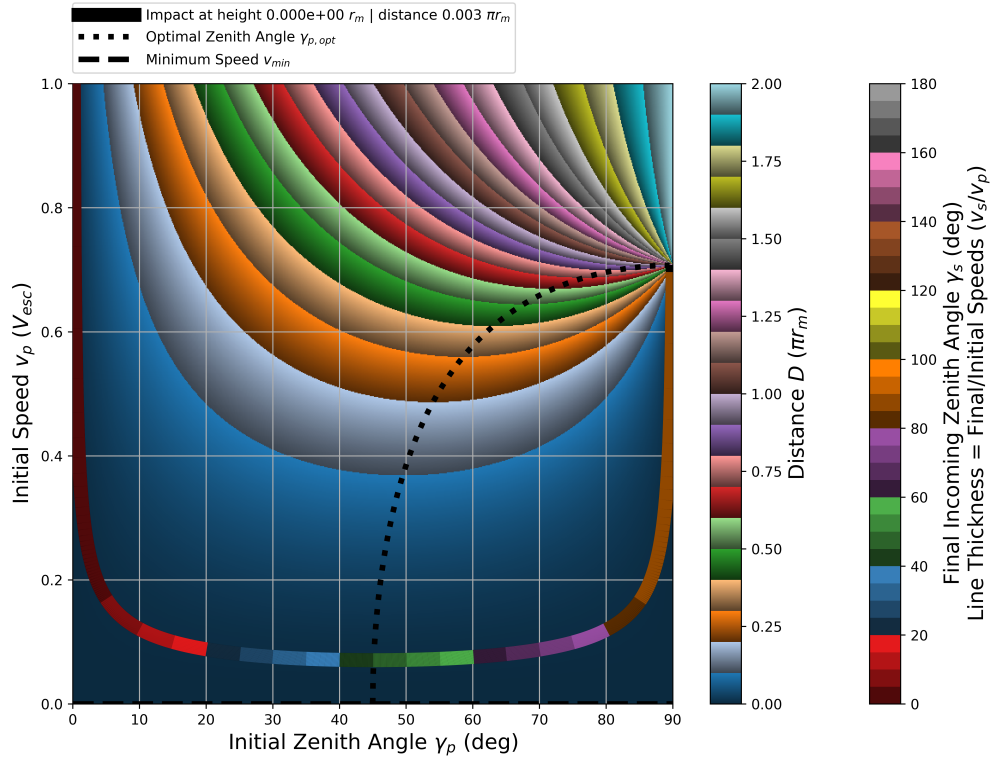


Figure 19: The initial speed  $v_p$  vs. initial zenith angle  $\gamma_p$  as a function of distance  $D$  is shown with a distance contour line at  $0.003\pi r_m$  with a point-asset altitude of  $0r_m$  (on the lunar surface). The contour line's color depicts the final incoming zenith angle  $\gamma_s$  where the thickness of the line gives the ratio of the final and initial speeds  $v_s/v_p$ . For a point-asset at the surface, this ratio will always be 1. The intersection of the distance contour line and the black dotted line gives the optimal zenith angle  $\gamma_{p,opt}$  (Equation (4.69)), i.e. the slowest initial speed to reach the contour line distance of  $0.003\pi r_m$ . Since the point-asset is on the lunar surface, there is no minimum bound on the speed (denoted by the black dashed line).

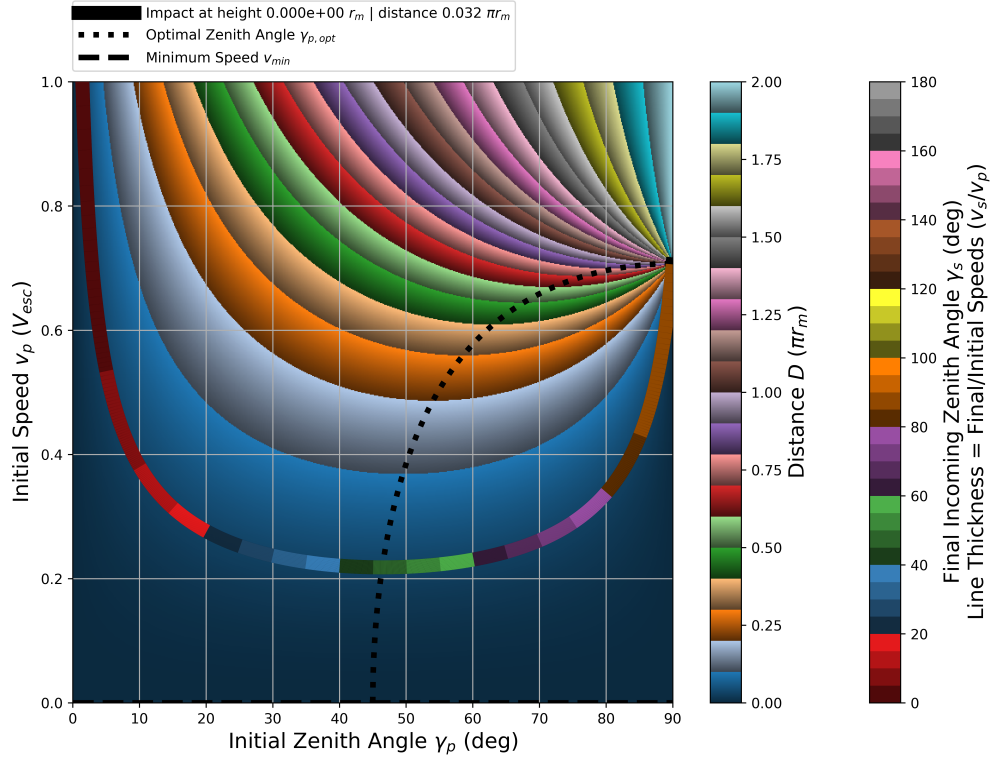


Figure 20: The initial speed  $v_p$  vs. initial zenith angle  $\gamma_p$  as a function of distance  $D$  is shown with a distance contour line at  $0.032\pi r_m$  with a point-asset altitude of  $0r_m$  (on the lunar surface). The contour line's color depicts the final incoming zenith angle  $\gamma_s$  where the thickness of the line gives the ratio of the final and initial speeds  $v_s/v_p$ . For a point-asset at the surface, this ratio will always be 1. The intersection of the distance contour line and the black dotted line gives the optimal zenith angle  $\gamma_{p,\text{opt}}$  (Equation (4.69)), i.e. the slowest initial speed to reach the contour line distance of  $0.032\pi r_m$ . Since the point-asset is on the lunar surface, there is no minimum bound on the speed (denoted by the black dashed line).

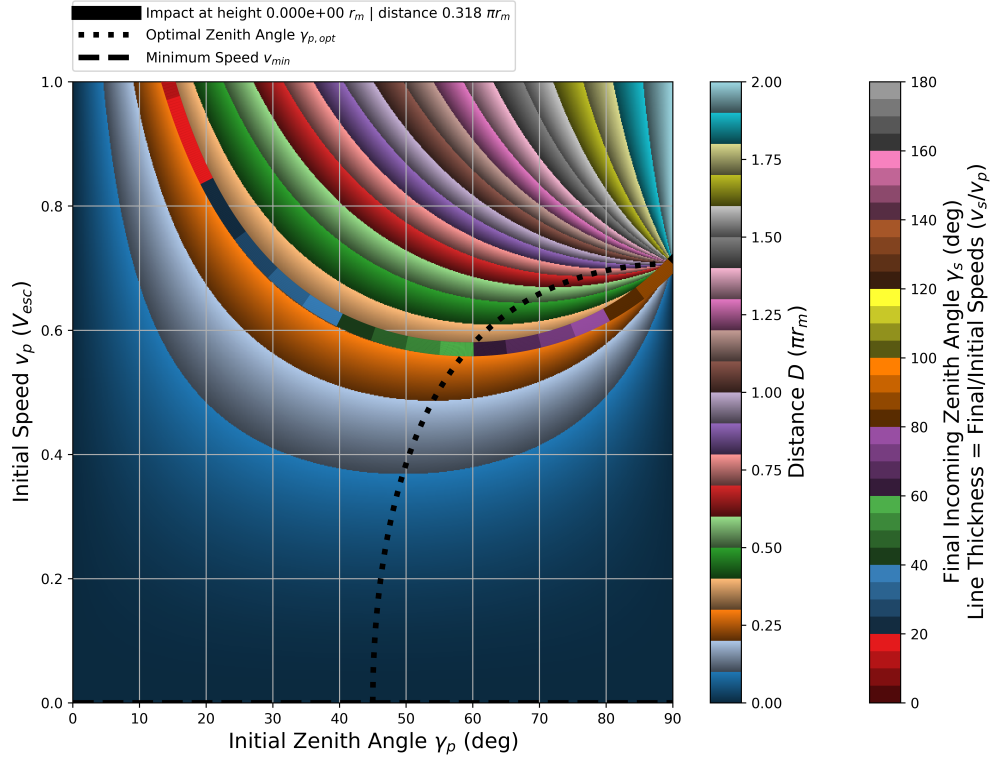


Figure 21: The initial speed  $v_p$  vs. initial zenith angle  $\gamma_p$  as a function of distance  $D$  is shown with a distance contour line at  $0.318\pi r_m$  with a point-asset altitude of  $0r_m$  (on the lunar surface). The contour line's color depicts the final incoming zenith angle  $\gamma_s$  where the thickness of the line gives the ratio of the final and initial speeds  $v_s/v_p$ . For a point-asset at the surface, this ratio will always be 1. The intersection of the distance contour line and the black dotted line gives the optimal zenith angle  $\gamma_{p,\text{opt}}$  (Equation (4.69)), i.e. the slowest initial speed to reach the contour line distance of  $0.318\pi r_m$ . Since the point-asset is on the lunar surface, there is no minimum bound on the speed (denoted by the black dashed line).

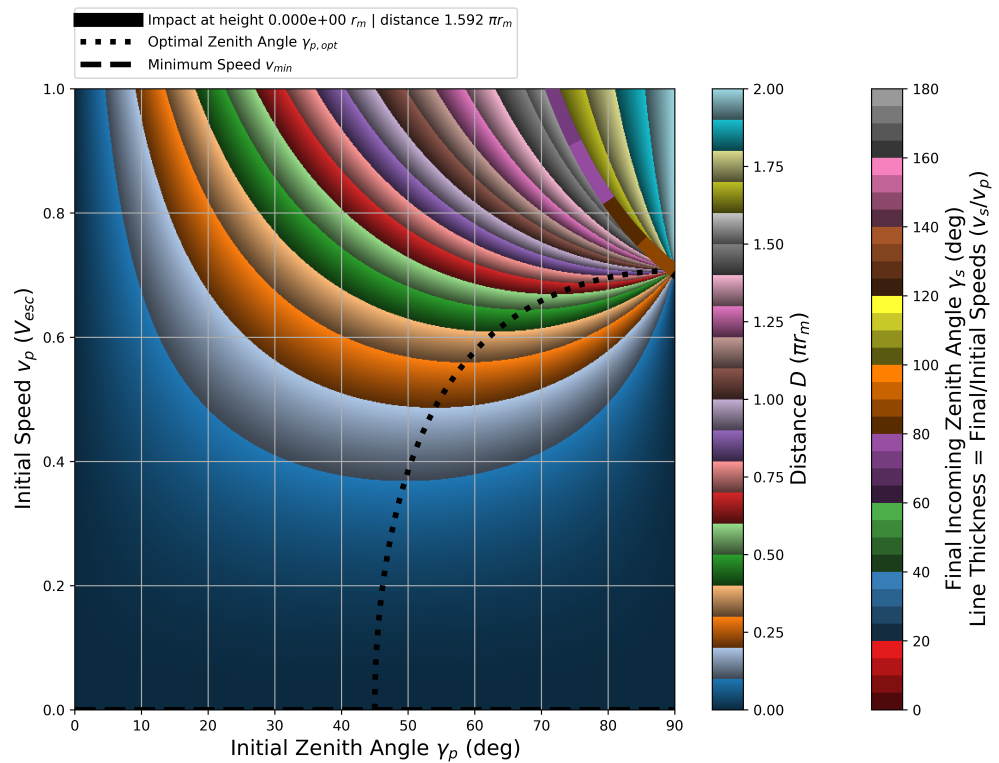


Figure 22: The initial speed  $v_p$  vs. initial zenith angle  $\gamma_p$  as a function of distance  $D$  is shown with a distance contour line at  $1.592\pi r_m$  (past the antipode) with a point-asset altitude of  $0r_m$  (on the lunar surface). The contour line's color depicts the final incoming zenith angle  $\gamma_s$  where the thickness of the line gives the ratio of the final and initial speeds  $v_s/v_p$ . For a point-asset at the surface, this ratio will always be 1. The intersection of the distance contour line and the black dotted line gives the optimal zenith angle  $\gamma_{p,\text{opt}}$  (Equation (4.69)), i.e. the slowest initial speed to reach the contour line distance of  $1.592\pi r_m$ . Since the point-asset is on the lunar surface, there is no minimum bound on the speed (denoted by the black dashed line).

#### 4.4.2 Crater on Surface to Asset at or above Surface

In general, it is assumed that the final position at the asset can be either at the surface or above the surface of the Moon. The selenographic distance between the initial and final points are the same as before, given as

$$\frac{D}{r_m} = \beta_s - \beta_p, \quad (4.61)$$

however,  $\beta_s$  is kept ambiguous.

First, equations for  $e \cos \beta_s$  and  $e \sin \beta_s$  are solved for using Equations (4.43) and (4.42), giving

$$e \cos \beta_s = 2 \frac{r_m}{r_s} \frac{v_p^2}{v_{esc}^2} \sin^2 \gamma_p - 1, \quad (4.62)$$

$$e \sin \beta_s = 2 \frac{r_m}{r_s} \frac{v_p^2}{v_{esc}^2} \sin \gamma_p \cos \gamma_p F(v_p, \gamma_p, r_s), \quad (4.63)$$

where

$$F(v_p, \gamma_p, r_s) = \pm \sqrt{1 + \frac{\frac{r_s}{r_m} - 1}{\cos^2 \gamma_p} \left( \frac{r_s}{r_m} + 1 - \frac{r_s/r_m}{v_p^2/v_{esc}^2} \right)}. \quad (4.64)$$

The sign of  $F$  is summarized by

$$sign(F) = \begin{cases} +, & \gamma_p > \gamma_{p,ap} \text{ (incoming below local horizon)} \\ -, & \text{otherwise (incoming above local horizon)} \end{cases}. \quad (4.65)$$

Plugging in the initial speed  $v_p$  (Equation (4.72)) into Equation (4.64), the sign of  $F$  becomes implicit in the equation and reads:

$$F(D, \gamma_p, r_s) = \left( \frac{r_s}{r_m} - 1 \right) \frac{\tan \gamma_p}{\tan \left( \frac{D}{2r_m} \right)} - \frac{r_s}{r_m}. \quad (4.66)$$

##### 4.4.2.1 Maximum Radial Distance $r_{max}$ vs. $v_p$ and $\gamma_p$

Note that the maximum radius by definition occurs at the apoapsis, or  $\beta_s = \pi$ , such that Equation (4.43) becomes (fixing the typo in Equation 16 of [Gault et al. \[1963\]](#))

$$\frac{r_{max}}{r_m} = \frac{1 + \sqrt{\left( \frac{2v_p^2}{v_{esc}^2} - 1 \right)^2 \sin^2 \gamma_p + \cos^2 \gamma_p}}{2 \left( 1 - \frac{v_p^2}{v_{esc}^2} \right)}, \quad (4.67)$$

which is also the solution to  $F(v_p, \gamma_p, r_s) = 0$  and solving for  $r_s$ , i.e.  $F(v_p, \gamma_p, r_{max}) = 0$ . When  $v_p \geq v_{esc}$ , the maximum radius is out at infinity and only the positive solution of  $F$  is used.

#### 4.4.2.2 Minimum Initial Speed $v_{p,min}$ vs. $\gamma_p$ and $r_s$

Solving for the speed when setting the discriminant of Equation (4.64) to zero, the minimum speed needed to hit the asset at a final radial distance  $r_s$  at an initial angle  $\gamma_p$  is given by

$$\frac{v_{p,min}^2}{v_{esc}^2} = \frac{2 \frac{r_s}{r_m} \left( \frac{r_s}{r_m} - 1 \right)}{2 \frac{r_s^2}{r_m^2} + \cos(2\gamma_p) - 1}, \quad (4.68)$$

which describes a *keep out zone* – if  $v_p < v_{p,min}$  for a given zenith angle  $\gamma_p$ , the ejecta will not reach the asset for all distances.

#### 4.4.2.3 Initial Zenith Angle to reach Apoapsis $\gamma_{p,ap}$ vs. $v_p$ and $r_s$

The initial zenith angle  $\gamma_{p,ap}$  required to reach an apoapsis at a radial distance  $r_s$  is given by (setting  $F = 0$  and solving for  $\gamma_{p,ap}$ )

$$\cos \gamma_{p,ap} = \sqrt{\left( \frac{r_s}{r_m} - 1 \right) \left[ \frac{r_s/r_m}{v_p^2/v_{esc}^2} - \left( \frac{r_s}{r_m} + 1 \right) \right]}. \quad (4.69)$$

#### 4.4.2.4 Initial Zenith Angle to reach Apoapsis $\gamma_{p,ap}$ vs. $D$ and $r_s$

Setting Equation (4.68) equal to Equation (4.72), replacing all the double angles with halved tangent angles, and solving for  $\gamma_{p,ap}$ , the equation reads

$$\tan \gamma_{p,ap} = \frac{\frac{r_s}{r_m} \tan \left( \frac{D}{2r_m} \right)}{\frac{r_s}{r_m} - 1}. \quad (4.70)$$

#### 4.4.2.5 Initial Speed $v_p$ vs. $D$ , $\gamma_p$ , and $r_s$

To arrive at the initial speed  $v_p$ , solve Equation (4.61) for  $\beta_s$  and take the cosine of both sides and multiply by  $e$ ,

$$\begin{aligned} e \cos \beta_s &= e \cos \left( \frac{D}{r_m} + \beta_p \right), \\ &= e \cos \beta_p \cos \left( \frac{D}{r_m} \right) - e \sin \beta_p \sin \left( \frac{D}{r_m} \right), \end{aligned} \quad (4.71)$$

and insert Equations (4.48), (4.49), and (4.62). After some algebra, the initial speed  $v_p$  is given by

$$\frac{v_p}{v_{esc}} = \frac{1}{\sqrt{\left[ \frac{\frac{r_m}{r_s} - \cos(\frac{D}{r_m})}{1 - \cos(\frac{D}{r_m})} \right] [1 - \cos(2\gamma_p)] + \sin(2\gamma_p) \cot \left( \frac{D}{2r_m} \right)}}. \quad (4.72)$$

It is clear that if  $r_s = r_m$ , Equation (4.51) is recovered.

#### 4.4.2.6 Distance $D$ vs. $v_p$ , $\gamma_p$ , and $r_s$

The distance equation, analogous to Equation (4.50), can be derived starting from Equation (4.71) and expanding the distance terms as

$$\cos\left(\frac{D}{r_m}\right) = \frac{1 - \tan^2\left(\frac{D}{2r_m}\right)}{1 + \tan^2\left(\frac{D}{2r_m}\right)}, \quad (4.73)$$

$$\sin\left(\frac{D}{r_m}\right) = \frac{2 \tan\left(\frac{D}{2r_m}\right)}{1 + \tan^2\left(\frac{D}{2r_m}\right)} \quad (4.74)$$

such that

$$e \cos \beta_s \left[ 1 + \tan^2\left(\frac{D}{2r_m}\right) \right] = e \cos \beta_p \left[ 1 - \tan^2\left(\frac{D}{2r_m}\right) \right] - e \sin \beta_p \left[ 2 \tan\left(\frac{D}{2r_m}\right) \right], \quad (4.75)$$

solving for  $\tan\left(\frac{D}{2r_m}\right)$  and simplifying (equivalent to solving Equation (4.72)),

$$\tan\left(\frac{D}{2r_m}\right) = \frac{\frac{v_p^2}{v_{esc}^2} \sin \gamma_p \cos \gamma_p \left(1 - \frac{r_m}{r_s} F\right)}{1 - \frac{v_p^2}{v_{esc}^2} \sin^2 \gamma_p \left(1 + \frac{r_m}{r_s}\right)}, \quad (4.76)$$

where  $F = F(v_p, \gamma_p, r_s)$  from Equation (4.64). Care must be taken on which sign to take in  $F$  for a closing solution (refer back to Equation (4.65)). The positive solution occurs when the ejecta is on its way up ( $\gamma_s > \pi/2$ ), before reaching the apoapsis, and the negative solution occurs on the way down ( $\gamma_s < \pi/2$ ), after passing the apoapsis. For  $r_s = r_m$  and using the negative sign of  $F$ , then  $F = -1$  and Equation (4.50) is retrieved.

Alternatively, if the separate expressions for  $F$  are set equal to each other and solved for the distance  $D$ , an equivalent equation for the distance can be written as

$$\tan\left(\frac{D}{2r_m}\right) = \frac{\left(\frac{r_s}{r_m} - 1\right) \tan \gamma_p}{\frac{r_s}{r_m} + F}, \quad (4.77)$$

where  $F = F(v_p, \gamma_p, r_s)$  as before. Note that if  $r_s = r_m$ , the equation for  $F$  degenerates to a constant (+1 or -1) and the distance cannot be ascertained from the equivalence made prior.

#### 4.4.2.7 Initial Zenith Angle $\gamma_p$ vs. $D$ , $v_p$ , and $r_s$

The initial zenith angle can be found similar to Section 4.4.1,

$$\cot \gamma_p = \frac{v_p^2}{v_{esc}^2} \cot\left(\frac{D}{2r_m}\right) \pm \sqrt{\frac{v_p^4}{v_{esc}^4} \cot^2\left(\frac{D}{2r_m}\right) + 2 \frac{v_p^2}{v_{esc}^2} \left( \frac{\frac{r_m}{r_s} - \cos\left(\frac{D}{r_m}\right)}{1 - \cos\left(\frac{D}{r_m}\right)} \right) - 1}, \quad (4.78)$$

where the positive solution is for  $\gamma_p < \gamma_{p,ap}$  and the negative solution is for  $\gamma_p > \gamma_{p,ap}$ .

#### 4.4.2.8 Minimum Initial Zenith Angle $\gamma_{p,min}$ vs. $D$ and $r_s$

Similar to the previous section, in order to find the minimum initial zenith angle  $\gamma_{p,min}$ , the initial speed approaches the escape speed  $v_p \rightarrow v_{esc}$  in Equation (4.78) and simplifying (taking the positive case),

$$\tan \gamma_{p,min} = \frac{\sin\left(\frac{D}{2r_m}\right)}{\cos\left(\frac{D}{2r_m}\right) + \sqrt{\frac{r_m}{r_s}}}. \quad (4.79)$$

When the distance is small  $D \ll r_m$ , the minimum angle becomes

$$\gamma_p \sim \frac{D}{4r_m} \left( \frac{2}{1 + \sqrt{\frac{r_m}{r_s}}} \right), \quad (4.80)$$

which equals Equation (4.55), and is exact, when  $r_s = r_m$ .

#### 4.4.2.9 Maximum Distance $D_{max}$ vs. $v_p$ and $r_s$

The maximum distance  $D_{max}$  can be solved similar as before, giving (positive case: direct path, negative case and modding the tangent argument by  $\pi$ : indirect path)

$$\tan\left(\frac{D_{max}}{2r_m}\right) = \pm \sqrt{\frac{\frac{v_p^2}{v_{esc}^2} \left[ 1 - \frac{r_s}{r_m} \left( 1 - \frac{v_p^2}{v_{esc}^2} \right) \right]}{\frac{r_s}{r_m} \left( 1 - \frac{v_p^2}{v_{esc}^2} \right) - \frac{v_p^2}{v_{esc}^2}}}. \quad (4.81)$$

#### 4.4.2.10 Minimum Initial Speed $v_{p,min}$ vs. $D$ and $r_s$

Looking at the discriminant of Equation (4.78) and setting to zero, the minimum initial speed to reach the asset is given by (different from Equation (4.68))

$$\frac{v_{p,min}^2}{v_{esc}^2} = + \tan\left(\frac{D}{2r_m}\right) \tan\left(\frac{\pi}{4} - \frac{D}{4r_m}\right) + \frac{\sec^2\left(\frac{D}{2r_m}\right)}{2} G(r_s, D), \quad (4.82)$$

where the perturbation from Equation (4.51) is

$$G(r_s, D) = 1 - \frac{r_m}{r_s} + 2 \sin\left(\frac{D}{2r_m}\right) \left[ \sqrt{1 - \left(1 - \frac{r_m}{r_s}\right) \left[ 1 - \frac{1 - \frac{r_m}{r_s}}{4 \sin^2\left(\frac{D}{2r_m}\right)} \right]} - 1 \right]. \quad (4.83)$$

If  $r_s = r_m$ , then  $G(r_s, D) = 0$  and Equation (4.57) is obtained.

#### 4.4.2.11 Optimal Initial Zenith Angle $\gamma_{p,opt}$ vs. $D$ and $r_s$

The optimal initial angle  $\gamma_{p,opt}$  is derived by inserting Equation (4.82) into Equation (4.78), giving

$$\cot \gamma_{p,opt} = \tan \left( \frac{\pi}{4} - \frac{D}{4r_m} \right) + \csc \left( \frac{D}{r_m} \right) G(r_s, D). \quad (4.84)$$

#### 4.4.2.12 Final Speed $v_s$ vs. $v_p$ and $r_s$

To find an equation for the final speed  $v_s$ , take  $r = r_s$  in Equation (4.39) and substitute Equation (4.41) for  $a$ , giving

$$\frac{v_s}{v_{esc}} = \sqrt{\frac{r_m}{r_s} + \frac{v_p^2}{v_{esc}^2} - 1}. \quad (4.85)$$

If  $r_s = r_m$ ,  $v_s = v_p$  is recovered.

#### 4.4.2.13 Final Zenith Angle $\gamma_s$ vs. $v_p$ , $\gamma_p$ , and $r_s$

To solve for the final zenith angle  $\gamma_s$ , start with Equation (4.44) and insert Equations (4.62) and (4.63) such that (Note the phase shift of  $\pi$  that introduces the extra minus sign<sup>16</sup> for the incoming angle at the asset)

$$\tan \gamma_s = \frac{1}{-F} \tan \gamma_p, \quad (4.86)$$

where  $F = F(v_p, \gamma_p, r_s)$  from Equation (4.64). If  $r_s = r_m$ , then<sup>17</sup>  $F = -1$  and  $\gamma_s = \gamma_p$  as expected.

#### 4.4.2.14 Final Radial Distance $r_s$ vs. $D$ , $v_p$ , and $\gamma_p$

The final radial distance  $r_s$  can also be solved for using Equation (4.72),

$$\frac{r_s}{r_m} = \frac{\frac{v_p^2}{v_{esc}^2} \sin^2 \gamma_p}{1 + \left( \frac{v_p^2}{v_{esc}^2} - 1 \right) \cos \left( \frac{D}{r_m} \right) - \frac{v_p^2}{v_{esc}^2} \cos \left( \frac{D}{r_m} - 2\gamma_p \right)}. \quad (4.87)$$

---

<sup>16</sup>The minus sign must be in the denominator for the arctan function to numerically map the quadrants properly.

<sup>17</sup>The  $F = 1$  case degenerates to the crater location and is a trivial case when  $r_s = r_m$ .

#### 4.4.2.15 Visualizing Ejecta in Phase Space

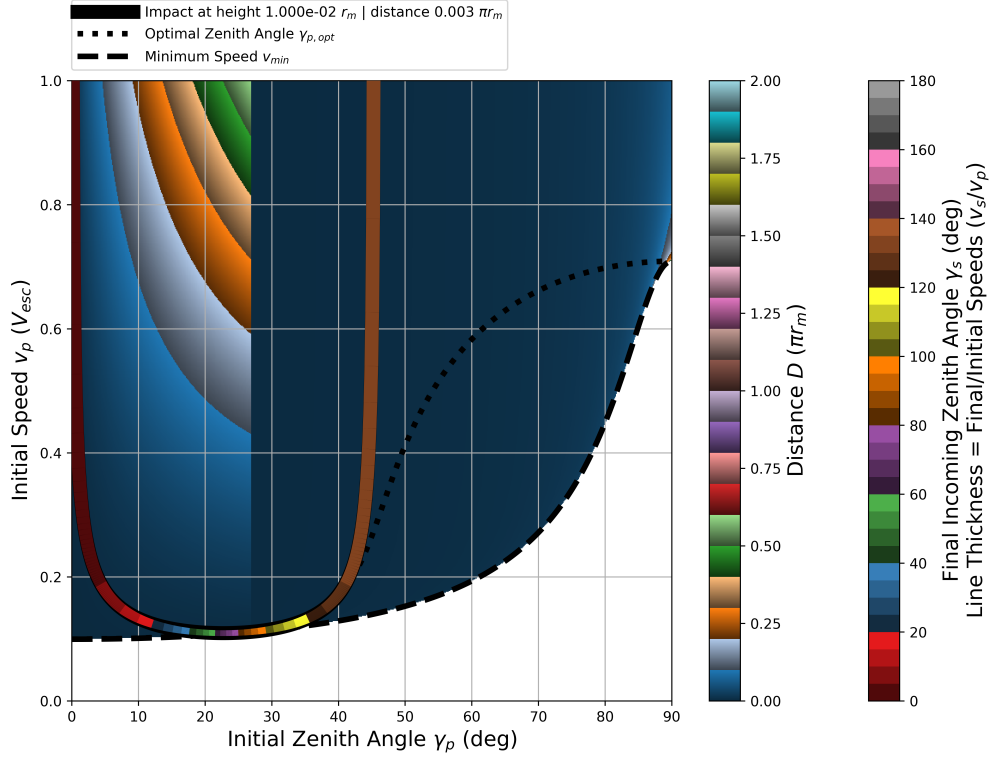


Figure 23: The initial speed  $v_p$  vs. initial zenith angle  $\gamma_p$  as a function of distance  $D$  is shown with a distance contour line at  $0.003\pi r_m$  with a point-asset altitude of  $0.01r_m$ . The contour line's color depicts the final incoming zenith angle  $\gamma_s$  where the thickness of the line gives the ratio of the final and initial speeds  $v_s/v_p$ . The intersection of the distance contour line and the black dotted line gives the optimal zenith angle  $\gamma_{p,opt}$  (Equation (4.69)), i.e. the slowest initial speed to reach the contour line distance of  $0.003\pi r_m$ . The black dashed line gives the minimum achievable initial speed  $v_{p,min}$  for a particular initial zenith angle (Equation (4.68)). The intersection of the distance contour line and  $v_{p,min}$  occurs when the final incoming zenith angle  $\gamma_s = 90^\circ$  (i.e., parallel to the local horizon) and marks a branch cut to another branch. The branch to the left of the branch cut are all ejecta hitting the point-asset above the local horizon, whereas the branch to the right are all ejecta hitting below the local horizon.

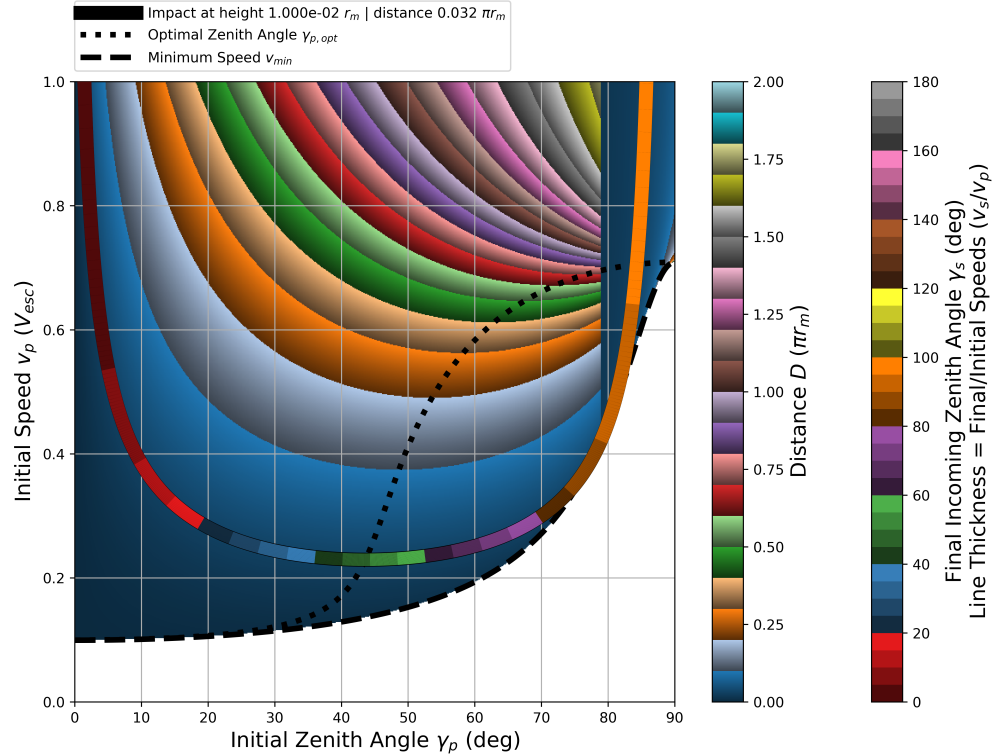


Figure 24: The initial speed  $v_p$  vs. initial zenith angle  $\gamma_p$  as a function of distance  $D$  is shown with a distance contour line at  $0.032\pi r_m$  with a point-asset altitude of  $0.01r_m$ . The contour line's color depicts the final incoming zenith angle  $\gamma_s$  where the thickness of the line gives the ratio of the final and initial speeds  $v_s/v_p$ . The intersection of the distance contour line and the black dotted line gives the optimal zenith angle  $\gamma_{p,opt}$  (Equation (4.69)), i.e. the slowest initial speed to reach the contour line distance of  $0.032\pi r_m$ . The black dashed line gives the minimum achievable initial speed  $v_{p,min}$  for a particular initial zenith angle (Equation (4.68)). The intersection of the distance contour line and  $v_{p,min}$  occurs when the final incoming zenith angle  $\gamma_s = 90^\circ$  (i.e., parallel to the local horizon) and marks a branch cut to another branch. The branch to the left of the branch cut are all ejecta hitting the point-asset above the local horizon, whereas the branch to the right are all ejecta hitting below the local horizon.

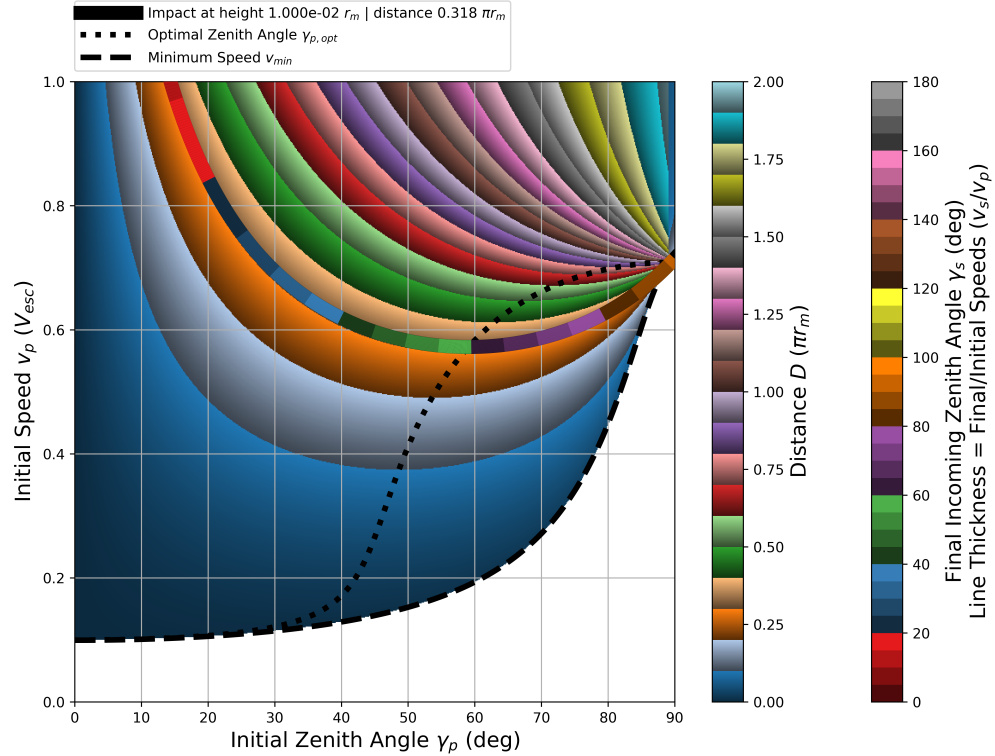


Figure 25: The initial speed  $v_p$  vs. initial zenith angle  $\gamma_p$  as a function of distance  $D$  is shown with a distance contour line at  $0.318\pi r_m$  with a point-asset altitude of  $0.01r_m$ . The contour line's color depicts the final incoming zenith angle  $\gamma_s$  where the thickness of the line gives the ratio of the final and initial speeds  $v_s/v_p$ . The intersection of the distance contour line and the black dotted line gives the optimal zenith angle  $\gamma_{p,opt}$  (Equation (4.69)), i.e. the slowest initial speed to reach the contour line distance of  $0.318\pi r_m$ . The black dashed line gives the minimum achievable initial speed  $v_{p,min}$  for a particular initial zenith angle (Equation (4.68)). The intersection of the distance contour line and  $v_{p,min}$  occurs when the final incoming zenith angle  $\gamma_s = 90^\circ$  (i.e., parallel to the local horizon) and marks a branch cut to another branch. The branch to the left of the branch cut are all ejecta hitting the point-asset above the local horizon, whereas the branch to the right are all ejecta hitting below the local horizon.

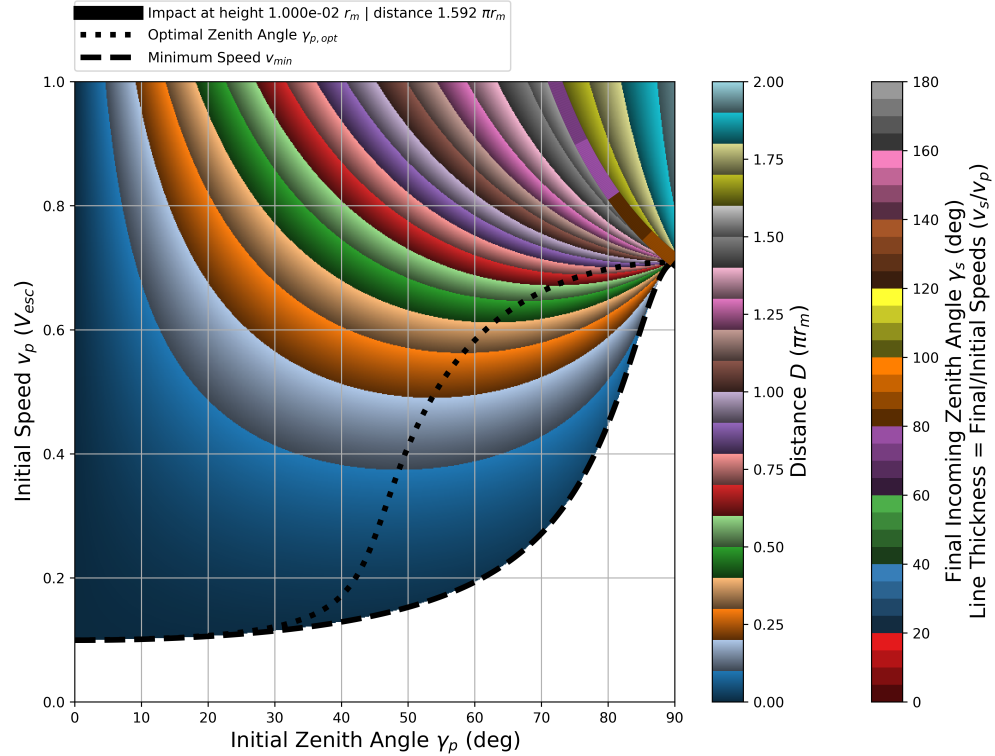


Figure 26: The initial speed  $v_p$  vs. initial zenith angle  $\gamma_p$  as a function of distance  $D$  is shown with a distance contour line at  $1.592\pi r_m$  with a point-asset altitude of  $0.01r_m$ . The contour line's color depicts the final incoming zenith angle  $\gamma_s$  where the thickness of the line gives the ratio of the final and initial speeds  $v_s/v_p$ . The intersection of the distance contour line and the black dotted line gives the optimal zenith angle  $\gamma_{p,opt}$  (Equation (4.69)), i.e. the slowest initial speed to reach the contour line distance of  $1.592\pi r_m$ . The black dashed line gives the minimum achievable initial speed  $v_{p,min}$  for a particular initial zenith angle (Equation (4.68)). The intersection of the distance contour line and  $v_{p,min}$  occurs when the final incoming zenith angle  $\gamma_s = 90^\circ$  (i.e., parallel to the local horizon) and marks a branch cut to another branch. The branch to the left of the branch cut are all ejecta hitting the point-asset above the local horizon, whereas the branch to the right are all ejecta hitting below the local horizon.

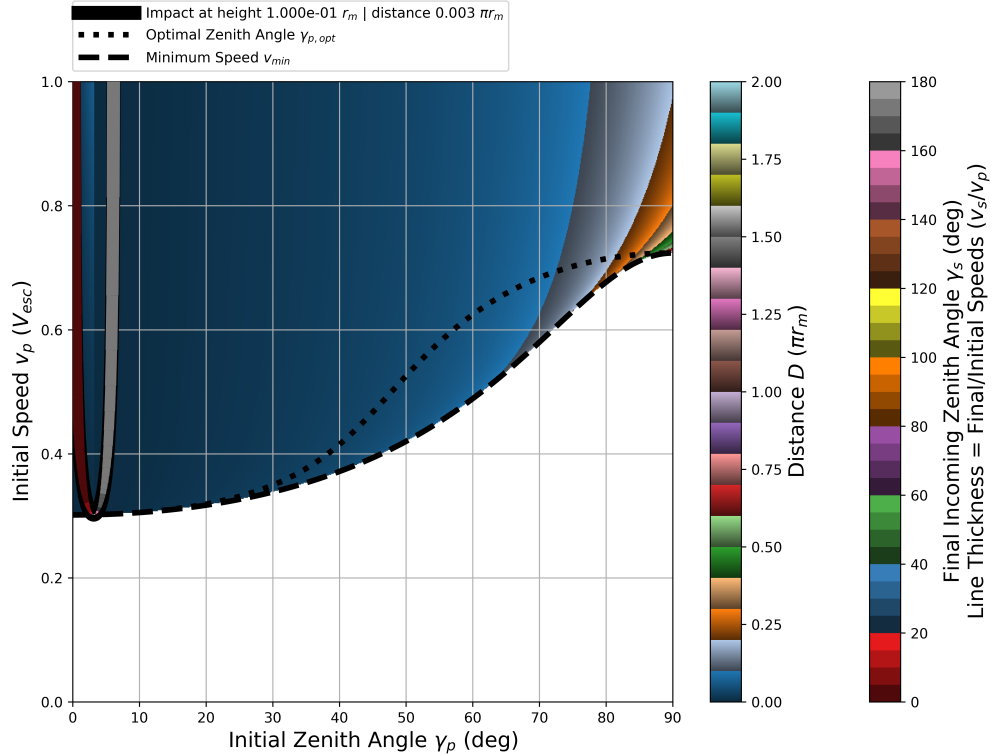


Figure 27: The initial speed  $v_p$  vs. initial zenith angle  $\gamma_p$  as a function of distance  $D$  is shown with a distance contour line at  $0.003\pi r_m$  with a point-asset altitude of  $0.1r_m$ . The contour line's color depicts the final incoming zenith angle  $\gamma_s$  where the thickness of the line gives the ratio of the final and initial speeds  $v_s/v_p$ . The intersection of the distance contour line and the black dotted line gives the optimal zenith angle  $\gamma_{p,opt}$  (Equation (4.69)), i.e. the slowest initial speed to reach the contour line distance of  $0.003\pi r_m$ . The black dashed line gives the minimum achievable initial speed  $v_{p,min}$  for a particular initial zenith angle (Equation (4.68)). The intersection of the distance contour line and  $v_{p,min}$  occurs when the final incoming zenith angle  $\gamma_s = 90^\circ$  (i.e., parallel to the local horizon) and marks a branch cut to another branch. The branch to the left of the branch cut are all ejecta hitting the point-asset above the local horizon, whereas the branch to the right are all ejecta hitting below the local horizon.

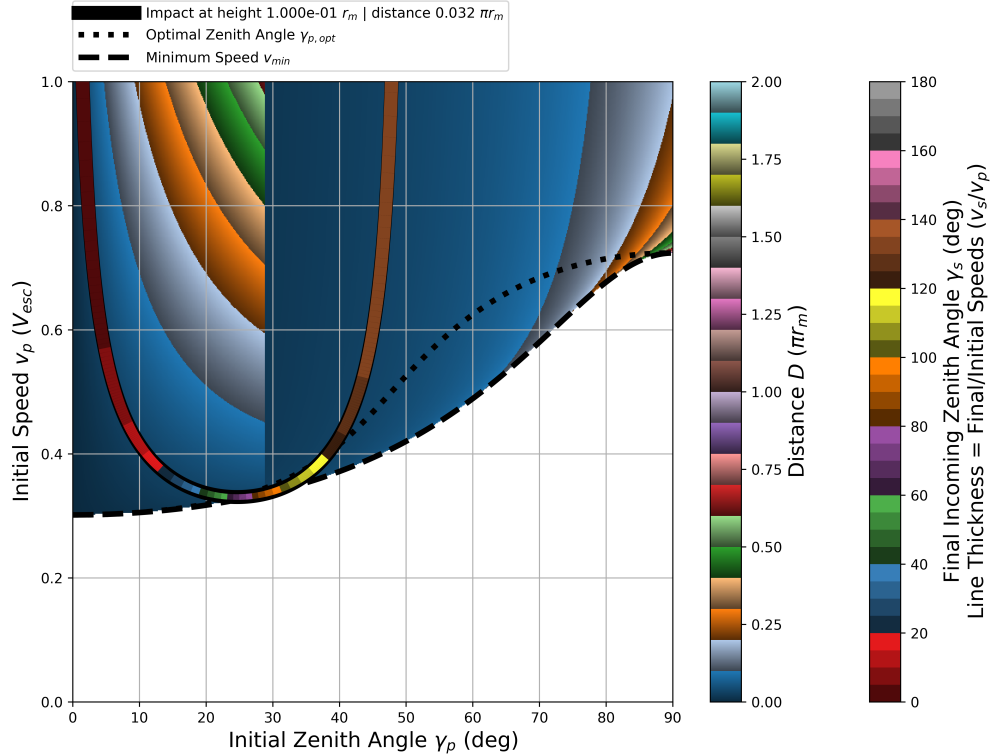


Figure 28: The initial speed  $v_p$  vs. initial zenith angle  $\gamma_p$  as a function of distance  $D$  is shown with a distance contour line at  $0.032\pi r_m$  with a point-asset altitude of  $0.1r_m$ . The contour line's color depicts the final incoming zenith angle  $\gamma_s$  where the thickness of the line gives the ratio of the final and initial speeds  $v_s/v_p$ . The intersection of the distance contour line and the black dotted line gives the optimal zenith angle  $\gamma_{p,opt}$  (Equation (4.69)), i.e. the slowest initial speed to reach the contour line distance of  $0.032\pi r_m$ . The black dashed line gives the minimum achievable initial speed  $v_{p,min}$  for a particular initial zenith angle (Equation (4.68)). The intersection of the distance contour line and  $v_{p,min}$  occurs when the final incoming zenith angle  $\gamma_s = 90^\circ$  (i.e., parallel to the local horizon) and marks a branch cut to another branch. The branch to the left of the branch cut are all ejecta hitting the point-asset above the local horizon, whereas the branch to the right are all ejecta hitting below the local horizon.

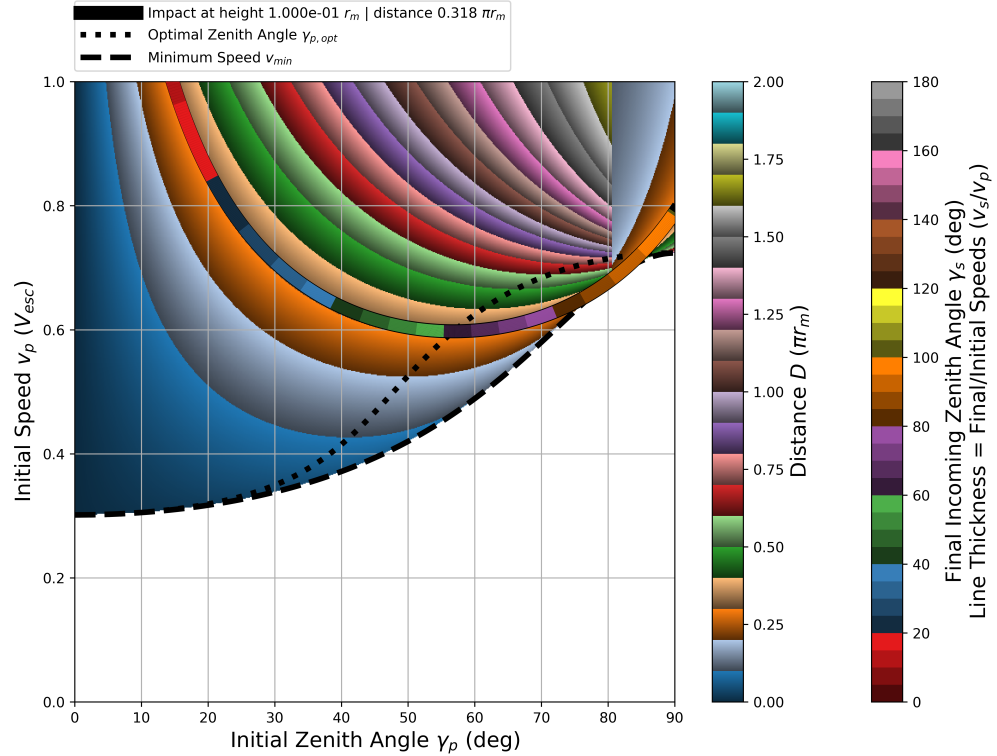


Figure 29: The initial speed  $v_p$  vs. initial zenith angle  $\gamma_p$  as a function of distance  $D$  is shown with a distance contour line at  $0.318\pi r_m$  with a point-asset altitude of  $0.1r_m$ . The contour line's color depicts the final incoming zenith angle  $\gamma_s$  where the thickness of the line gives the ratio of the final and initial speeds  $v_s/v_p$ . The intersection of the distance contour line and the black dotted line gives the optimal zenith angle  $\gamma_{p,opt}$  (Equation (4.69)), i.e. the slowest initial speed to reach the contour line distance of  $0.318\pi r_m$ . The black dashed line gives the minimum achievable initial speed  $v_{p,min}$  for a particular initial zenith angle (Equation (4.68)). The intersection of the distance contour line and  $v_{p,min}$  occurs when the final incoming zenith angle  $\gamma_s = 90^\circ$  (i.e., parallel to the local horizon) and marks a branch cut to another branch. The branch to the left of the branch cut are all ejecta hitting the point-asset above the local horizon, whereas the branch to the right are all ejecta hitting below the local horizon.

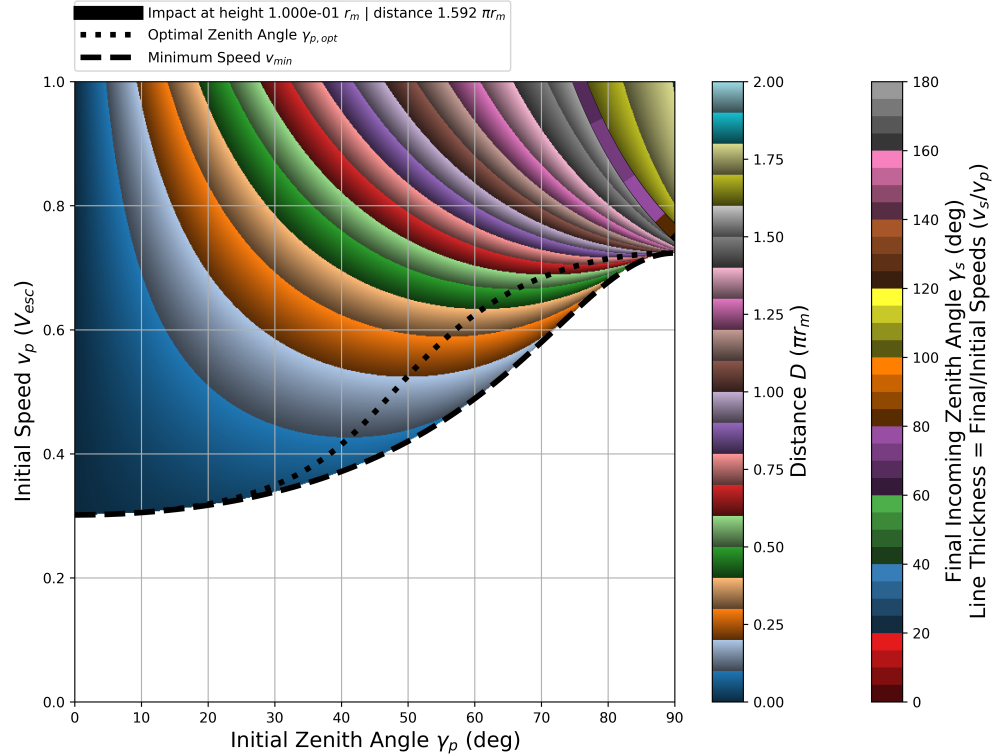


Figure 30: The initial speed  $v_p$  vs. initial zenith angle  $\gamma_p$  as a function of distance  $D$  is shown with a distance contour line at  $1.592\pi r_m$  with a point-asset altitude of  $0.1r_m$ . The contour line's color depicts the final incoming zenith angle  $\gamma_s$  where the thickness of the line gives the ratio of the final and initial speeds  $v_s/v_p$ . The intersection of the distance contour line and the black dotted line gives the optimal zenith angle  $\gamma_{p,opt}$  (Equation (4.69)), i.e. the slowest initial speed to reach the contour line distance of  $1.592\pi r_m$ . The black dashed line gives the minimum achievable initial speed  $v_{p,min}$  for a particular initial zenith angle (Equation (4.68)). The intersection of the distance contour line and  $v_{p,min}$  occurs when the final incoming zenith angle  $\gamma_s = 90^\circ$  (i.e., parallel to the local horizon) and marks a branch cut to another branch. The branch to the left of the branch cut are all ejecta hitting the point-asset above the local horizon, whereas the branch to the right are all ejecta hitting below the local horizon.

## 4.5 Azimuthal Field-of-View

The field-of-view (FOV) of the asset from the crater, in terms of the azimuth, must be understood by spherical geometry. If the asset is assumed to be a cylinder with the base parallel to the local horizon, then the effective radius of the cylinder  $a_i = c_i/1$  and the effective distance from the crater to the asset  $D_i$  is modified from the line-of-sight radius and distance  $a$  and  $D$ , respectively (see Figure 31). The center of the asset is at point  $\mathcal{O}$ .

There is a special case when the crater is within the asset's antipode projection (Figure 32). The effective radius  $a_i$  becomes  $a_i = (a_{0,i} + a_{1,i})/2$  with the effective distance  $D_i$ , not shown in the figure. Both the asset and asset antipode are superimposed on each other, also showing the crater  $\mathcal{C}$  and crater antipode  $\mathcal{C}_{antipode}$  points.

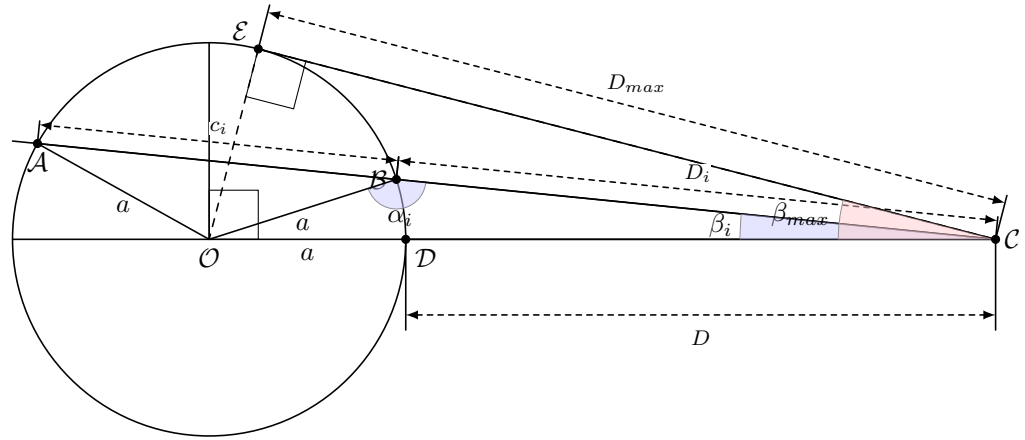


Figure 31: A bird's eye view of the asset (circle of radius  $a$ ) and the crater location (point  $\mathcal{C}$ ) projected on the surface of the Moon. The FOV the asset encompasses from the point of view of the crater is  $2\beta_{max}$ .

### 4.5.1 Maximum Azimuthal FOV

The FOV of the asset from the crater  $2\beta_{max}$  is given by

$$\sin \beta_{max} = \begin{cases} \frac{\sin a}{\sin(D+a)}, & \text{for } \sin(D+a) \geq \sin a \\ 1, & \text{for } \sin(D+a) < \sin a \end{cases} . \quad (4.88)$$

### 4.5.2 Effective Cylindrical Diameter

The effective cylindrical diameter  $c_i$  decreases as  $\beta_i$  increases, which is given by (using planar law of cosines, assuming  $a \ll r_m$ )

$$c_i = 2a|\cos \alpha_i|, \quad (4.89)$$

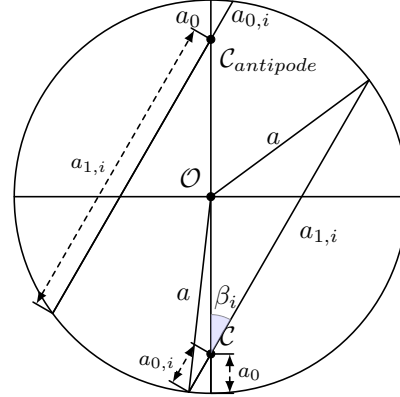


Figure 32: A bird's eye view of the asset (circle of radius  $a$ ) and the crater location (point  $C$ ) projected on the surface of the Moon. The special case shown occurs when the antipode of the crater is inside the asset and there is no restriction on the FOV angle  $\beta_i$ .

where the angle  $\alpha_i$  is given by (using the spherical law of sines)

$$\cos \alpha_i = -\sqrt{1 - \left( \frac{\sin \beta_i}{\sin a / \sin(D + a)} \right)^2}. \quad (4.90)$$

Using the special case shown in Figure 32, Equation (4.90) stays the same. Using the planar law of cosines, the effective diameter becomes

$$c_i = a_{0,i} + a_{1,i} = 2\sqrt{a^2 - (a - a_0)^2 \sin^2 \beta_i}. \quad (4.91)$$

and can be rewritten in the form shown in Equation (4.90). Note, that  $a - a_0 = D + a - \pi$  (all distances in units of  $r_m$ ).

#### 4.5.3 Effective Crater-to-Asset Distance

In general (Figure 31), the effective crater-to-asset distance can be derived by starting with using the spherical law of cosines for the angles  $\beta_i$  and  $\alpha_i$ ,

$$\cos a = \cos(D + a) \cos D_i + \sin(D + a) \sin D_i \cos \beta_i, \quad (4.92)$$

$$\cos(D + a) = \cos a \cos D_i + \sin a \sin D_i \cos \alpha_i. \quad (4.93)$$

First, eliminate  $\cos \beta_i$  by multiplying Equation (4.92) by  $\cos a$  and Equation (4.93) by  $-\cos(D + a)$  and adding, giving

$$\begin{aligned} \cos^2 a - \cos^2(D + a) &= \\ [\cos a \sin(D + a) \cos \beta_i - \sin a \cos(D + a) \cos \alpha_i] \sin D_i. \end{aligned} \quad (4.94)$$

Next, start with Equations (4.92) and (4.93) again and eliminate  $\sin D_i$  by multiplying Equation (4.92) by  $\sin a \cos \alpha_i$  and Equation (4.93) by  $-\sin(D + a) \cos \beta_i$  and adding, giving

$$\begin{aligned} \sin a \cos a \cos \alpha_i - \sin(D + a) \cos(D + a) \cos \beta_i &= \\ -[\cos a \sin(D + a) \cos \beta_i - \sin a \cos(D + a) \cos \alpha_i] \cos D_i. \end{aligned} \quad (4.95)$$

Finally, take Equation (4.94) and divide by Equation (4.95), giving

$$\tan D_i = \frac{\cos^2 a - \cos^2(D + a)}{\sin(D + a) \cos(D + a) \cos \beta_i - \sin a \cos a \cos \alpha_i}. \quad (4.96)$$

However, for the special case (Figure 32), the effective distance is simply

$$\begin{aligned} D_i &= \pi - a_{0,i} \\ &= \pi + (D + a - \pi) \cos \beta_i - \frac{c_i}{2}. \end{aligned} \quad (4.97)$$

## 4.6 Selenographic Distance & Bearing

Given two latitude-longitude points on a sphere,  $(\phi_1, \lambda_1)$  and  $(\phi_2, \lambda_2)$ , the distance and bearing can be computed following Chris Veness's webpage<sup>18</sup>.

The distance  $D$  is given by the equation

$$\tan\left(\frac{D}{2r_m}\right) = \sqrt{\frac{a}{1-a}}, \quad (4.98)$$

where  $a$  is given by

$$a = \sin^2(\Delta\phi/2) + \cos\phi_1 \cos\phi_2 \sin^2(\Delta\lambda/2), \quad (4.99)$$

for  $\Delta\phi = \phi_1 - \phi_2$  and  $\Delta\lambda = \lambda_1 - \lambda_2$ . Solving for the distance and simplifying,

$$D = 2r_m \arcsin(\sqrt{a}), \quad (4.100)$$

or

$$D = 2r_m \arccos(\sqrt{1-a}). \quad (4.101)$$

Other useful expressions involving trigonometric functions of  $D/r_m$  are

$$\sin(D/r_m) = 2\sqrt{a(1-a)}, \quad (4.102)$$

$$\cos(D/r_m) = 1 - 2a, \quad (4.103)$$

$$\tan(D/r_m) = \frac{2\sqrt{a(1-a)}}{1 - 2a}. \quad (4.104)$$

Equation (4.98) is the shortest distance between two coordinate points. For the long-distance, use

$$\tan\left(\pi - \frac{D}{2r_m}\right) = -\tan\left(\frac{D}{2r_m}\right) = -\sqrt{\frac{a}{1-a}}. \quad (4.105)$$

The initial bearing  $\theta$  (from due north) is given by the following equation (assuming the short-distance):

$$\tan \theta_{i(1,2)} = \frac{\sin \Delta\lambda \cos \phi_2}{\cos \phi_1 \sin \phi_2 - \sin \phi_1 \cos \phi_2 \cos \Delta\lambda}. \quad (4.106)$$

To find the final bearing (assuming the short-distance), swap  $\phi_1 \longleftrightarrow \phi_2$  and  $\lambda_1 \longleftrightarrow \lambda_2$  and reverse the angle such that

$$\theta_{f(1,2)} = (\theta_{i(2,1)} + \pi) \mod 2\pi. \quad (4.107)$$

In order to compute the initial and final bearing for the long-distance trajectory, add  $\pi$  and then mod by  $2\pi$  to Equations (4.106) and (4.107). In other words, swap initial and final bearings  $\theta_{i(1,2)} \longleftrightarrow \theta_{f(1,2)}$ .

<sup>18</sup><https://www.movable-type.co.uk/scripts/latlong.html>

The final latitude and longitude can also be obtained if the distance  $D$  and bearing  $\theta$  from the starting location are given. The latitude and longitude are given by

$$\phi_2 = \arcsin [\sin \phi_1 \cos(D/r_m) + \cos \phi_1 \sin(D/r_m) \cos \theta], \quad (4.108)$$

$$\lambda_2 = \lambda_1 + \arctan \left[ \frac{\sin \theta \sin(D/r_m) \cos \phi_1}{\cos(D/r_m) - \sin \phi_1 \sin \phi_2} \right]. \quad (4.109)$$

## 4.7 Coriolis Force

The Coriolis force on secondary ejecta may also affect the ground path. To estimate the strength of the Coriolis force, the greatest speed due to the rotation of the Moon is at the equator, given by

$$v_c = \frac{2\pi r_m}{T} = \frac{2\pi * 1737.1 \text{ km}}{27.322 \text{ days}} = 4.62 \text{ m/s}. \quad (4.110)$$

Therefore, the Coriolis force can be ignored if the ejecta speed  $v$  is greater than roughly  $\sim 10 - 15 \times v_c$ , or about 46 m/s to 70 m/s. This translates into ejecta distances less than 3 km, which at those small distances the Coriolis force should not cause an effect anyways. So in general, the conclusion is to ignore the Coriolis force all together.

To quantify this conclusion, the Rossby number is given by

$$R_o = \frac{v}{fL}. \quad (4.111)$$

If it is assumed that the ejecta angle of  $45^\circ$  is used, then plotting  $D$  as a function of  $v$  in Equation (4.50) shows that  $D \rightarrow L \sim v^2$  for  $v < v_{esc}$ . Taking the example above for  $v = 70 \text{ m/s}$ ,  $L = 3 \text{ km}$ , and  $f = 2T$  to solve for  $A$ , it is found that the Rossby number for secondary ejecta on the Moon is

$$R_o = \frac{A}{fv}, \quad (4.112)$$

where  $A = 1.63 \text{ m/s}^2$ <sup>19</sup>,  $f = 5.328 \times 10^{-6} \text{ rad/s}$ , and  $v$  is in units of m/s. In order to have  $R_o \sim 1$  (small  $R_o$  means the Coriolis forces cannot be ignored), the speed of  $v > 306 \text{ km/s}$  would be needed, which far exceeds the escape speed. The smallest  $R_o$  can ever be is  $R_o \sim 128$  when taking  $v \rightarrow v_{esc}$ . Therefore, the Coriolis force can be ignored.

## 5 Scaling Laws

The scaling laws used in this model are from [Housen and Holsapple \[2011\]](#), which assume point-source crater evolution that applies to the final crater size, the growth of the transient crater and the majority of the observable ejecta field.

---

<sup>19</sup>Curiously, this is basically the acceleration due to gravity on the Moon.

Depending on the size of the impact event, there are two separate cases: the strength regime and the gravity regime, discussed in Section 5.1. For smaller impacts, the strength regime dominates while for larger impacts, the gravity regime dominates. For materials that do not have a well defined strength (such as dry sand), the gravity regime dominates for all sizes of impacts.

## 5.1 Crater Size – Strength & Gravity Regime

The crater radius as determined by the [Housen and Holsapple \[2011\]](#) scaling laws is computed for both the strength and the gravity regime as the following:

$$R \left( \frac{\rho}{m} \right)^{1/3} = H_2 \left( \frac{\rho}{\delta} \right)^{\frac{1-3\nu}{3}} \left[ \frac{Y}{\rho U^2} \right]^{-\frac{\mu}{2}}, \quad (5.1)$$

for the strength regime with  $R$  the crater radius,  $\rho$  the target bulk density,  $m$  the impactor mass,  $\delta$  the impactor bulk density,  $Y$  the material strength (shear for granular targets and tensile for solid targets), and  $U$  the normal component<sup>20</sup> of the impactor speed. See Table 6 for various scaling law parameters, and

$$R \left( \frac{\rho}{m} \right)^{1/3} = H_1 \left( \frac{\rho}{\delta} \right)^{\frac{2+\mu-6\nu}{3(2+\mu)}} \left[ \frac{ga}{U^2} \right]^{-\frac{\mu}{2+\mu}}, \quad (5.2)$$

for the gravity regime with  $g = GM/r_m^2 = 1.625 \text{ m s}^{-2}$  the lunar surface gravity, and  $a$  the impactor radius.

## 5.2 Mass Ejected from Crater

The mass ejected from a crater by an impact can be summarized into two equations parameterized by the position from the crater center  $x$  as

$$\frac{v}{U} = C_1 \left[ \frac{x}{a} \left( \frac{\rho}{\delta} \right)^\nu \right]^{-\frac{1}{\mu}} \left( 1 - \frac{x}{n_2 R} \right)^p, \quad (5.3)$$

$$\frac{M}{m} = \frac{3k}{4\pi} \frac{\rho}{\delta} \left[ \left( \frac{x}{a} \right)^3 - n_1^3 \right], \quad (5.4)$$

for  $n_1 a \leq x \leq n_2 R$ , where  $v$  is the ejecta speed (see Figures 33 and 34), and  $M$  is the mass ejected at speeds equal to or greater than  $v$ .

The maximum speed occurs when  $x = n_1 a$ , or very close to ground zero, and is given by (see Figure 35)

$$\frac{v_{max}}{U} = C_1 \left[ n_1 \left( \frac{\rho}{\delta} \right)^\nu \right]^{-\frac{1}{\mu}} \left( 1 - \frac{n_1 a}{n_2 R} \right)^p. \quad (5.5)$$

If  $v_{max} \leq 0$ , then it is assumed no ejecta was created by the impact.

---

<sup>20</sup>See Section 5.2 of [Housen and Holsapple \[2011\]](#).

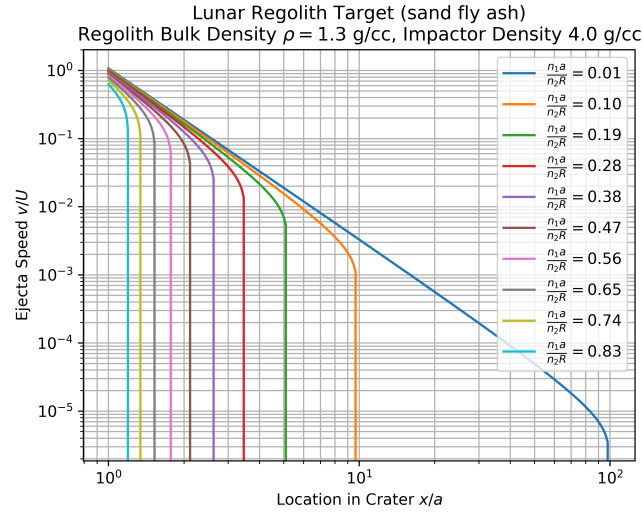


Figure 33: The ejecta speed  $v/U$  (Equation (5.3)) vs. location in the crater  $x/a$  for a lunar regolith target (using SFA in Table 6) with regolith surface bulk density  $\rho = 1.3$  g/cc and an impactor density of 4.0 g/cc (e.g., MEM high density population). Each curve has a set effective impactor to crater radius  $\frac{n_1 a}{n_2 R}$ .

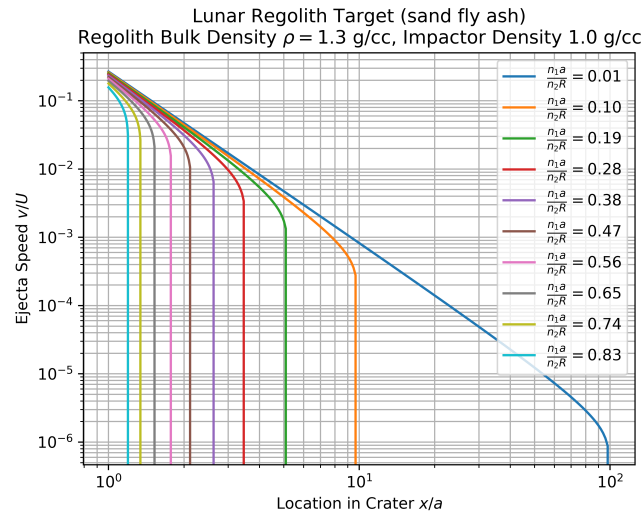


Figure 34: The ejecta speed  $v/U$  (Equation (5.3)) vs. location in the crater  $x/a$  for a lunar regolith target (using SFA in Table 6) with regolith surface bulk density  $\rho = 1.3$  g/cc and an impactor density of 1.0 g/cc (e.g., MEM low density population). Each curve has a set effective impactor to crater radius  $\frac{n_1 a}{n_2 R}$ .

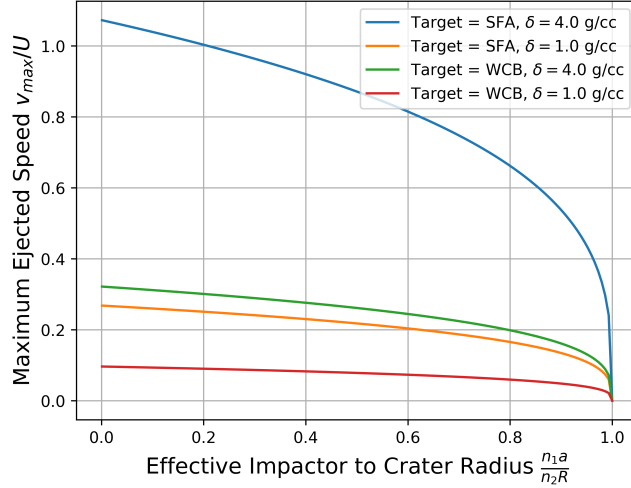


Figure 35: The ejecta speed  $v/U$  (Equation (5.3)) vs. effective impactor to crater radius  $\frac{n_1a}{n_2R}$  for a lunar regolith target (using SFA and WCB in Table 6) with regolith surface bulk density  $\rho = 1.3$  g/cc and an impactor density of 1.0 and 4.0 g/cc (e.g., MEM low and high density population).

The total mass ejected is given when  $x = n_2R$ ,

$$\frac{M_{tot}}{m} = \frac{3k}{4\pi} \frac{\rho}{\delta} \left[ \left( \frac{n_2R}{a} \right)^3 - n_1^3 \right]. \quad (5.6)$$

It is equivalent to say that if  $M_{tot} \leq 0$ , then no ejecta was created by the impact.

The ejecta speed  $v$  and mass of ejecta at speeds  $v$  or greater  $M$ , can also be written in terms of the maximum speed  $v_{max}$  and total ejected mass  $M_{tot}$  as

$$\frac{v}{v_{max}} = \left( \frac{x}{n_1a} \right)^{-\frac{1}{\mu}} \frac{\left( 1 - \frac{x}{n_2R} \right)^p}{\left( 1 - \left( \frac{n_1a}{n_2R} \right)^3 \right)^p}, \quad (5.7)$$

and

$$\frac{M}{M_{tot}} = \frac{\left( \frac{x}{n_2R} \right)^3 - \left( \frac{n_1a}{n_2R} \right)^3}{1 - \left( \frac{n_1a}{n_2R} \right)^3}. \quad (5.8)$$

### 5.2.1 Ejected Mass Distribution

The differential mass, or ejecta mass distribution, in terms of the speed can be computed using the chain rule as follows:

$$\frac{dM}{dv} = \frac{dM}{dx} \frac{dx}{dv} = \frac{dM}{dx} \left( \frac{dv}{dx} \right)^{-1}. \quad (5.9)$$

The first term can be calculated from Equation (5.4) such that

$$\frac{dM}{dx} = \frac{9k}{4\pi} \frac{\rho}{\delta} \left(\frac{x}{a}\right)^2 \frac{m}{a}, \quad (5.10)$$

and the second term from Equation (5.3), giving

$$\frac{dv}{dx} = -C_1 \left[ \frac{x}{a} \left( \frac{\rho}{\delta} \right)^\nu \right]^{-\frac{1}{\mu}} \left( 1 - \frac{x}{n_2 R} \right)^p \frac{1 + (\mu p - 1) \frac{x}{n_2 R}}{\mu \left( 1 - \frac{x}{n_2 R} \right)} \frac{U}{x}. \quad (5.11)$$

Therefore, the differential mass is found by taking Equation (5.10) divided by Equation (5.11) giving

$$\frac{dM}{dv} = -\frac{9k}{4\pi} \frac{\rho}{\delta} \left( \frac{x}{a} \right)^3 \frac{\mu \left( 1 - \frac{x}{n_2 R} \right)}{1 + (\mu p - 1) \frac{x}{n_2 R}} \frac{m}{v}. \quad (5.12)$$

### 5.3 Scaling Law Parameters

The various sets of parameters for different target materials are given in Table 3 of [Housen and Holsapple \[2011\]](#) with most of them copied here in Table 6, with undefined values filled in that are best represented by either solid, semi-solid, or fine material where applicable. If a material has zero strength, the crater scaling is automatically in the gravity regime and there is no strength regime (and no need for  $H_2$  to be defined).

Table 6: Summary of constants used in the [Housen and Holsapple \[2011\]](#) ejecta model.

Curve no.	C1	C2	C3	C4	C5	C6	C7	C8
Target	Water	Rock	WCB	Sand	Sand	GMS	SFA	PS
Porosity	~ 0	~ 0	20%	35 ± 5%	35 ± 5%	36%	45%	60%
$\mu$	0.55	0.55	0.46	0.41	0.41	0.45	0.4	0.35
$C_1$	1.5	1.5	0.18	0.55	0.55	1.0	0.55	0.6
$k$	0.2	0.3	0.3	0.3	0.3	0.5	0.3	0.32
$H_1$	0.68	0.68* <sup>1</sup>	0.5* <sup>2</sup>	0.59	0.59	0.8	0.59* <sup>3</sup>	0.59* <sup>3</sup>
$H_2$	—	1.2	0.38	—	—	—	0.4	0.81
$n_{2,G}$	1.5	1.5	1.3* <sup>3</sup>	1.3	1.3	1.3	1.2* <sup>2</sup>	1.2* <sup>2</sup>
$p$	0.5	0.5	0.3	0.3	0.3	0.3	0.3	0.2
$Y$ (MPa)	0	30	0.45	0	0	0	$4 \times 10^{-3}$	$2 \times 10^{-3}$

Note: WCB = weakly cemented basalt, GMS = glass micro-spheres, PS = perlite/sand mixture, SFA = sand/fly ash. All cases shown in this table used:  $\nu = 0.4$ ,  $n_1 = 1.2$ ,  $n_{2,S} = 1$ ,  $g = 9.81 \text{ m/s}^2$ .

\*1 from water, \*2 no value given, \*3 from sand.

The average regolith porosity from 0 – 60 cm is  $46 \pm 2\%$  (see Table 1), so the set of parameters that define SFA (sand/fly ash) are adopted. For a higher fidelity strength, Equation (2.11) can be used instead of  $Y = 4 \text{ kPa}$ .

## 6 Numerical Methods

### 6.1 Asset Collision Algorithm

In this lunar ejecta model, the asset is assumed to be cylindrical in shape with the cylinder's symmetry axis normal to the lunar surface. The asset can sit on the surface of the Moon or have any height above the surface,  $h_{sb}$  such that

$$h_{sb} = r_s - r_m. \quad (6.1)$$

The height (or length) of the asset itself is defined to be  $l_s$ , so that the height of the top of the asset from the lunar surface is given by

$$h_{st} = h_{sb} + l_s. \quad (6.2)$$

The radius of the cylinder is defined to be  $a_s$ .

In order to uniformly<sup>21</sup> generate ejecta that originates from a crater and will hit the asset, there are bounding points that define the extent of the minimum and maximum ejecta speed ( $v_{min,\gamma_p}$  and  $v_{max,\gamma_p}$ ) for a given ejecta zenith and azimuth angle. It is assumed that for speeds  $v_p$  such that  $v_{min,\gamma_p} \leq v_p \leq v_{max,\gamma_p}$ , the  $(v_p, \gamma_p)$  pair gives ejecta that will hit the asset. The question then becomes, where?

Given the ejecta speed  $v_p$ , zenith angle  $\gamma_p$ , selenographic distance to the near side of the asset  $D$ , in addition to the asset height above the lunar surface and the size, the height  $r_s$  and distance  $D_s$  at which the ejecta hits the asset is needed. To know which surface the ejecta hits (top, side, bottom), the state of the ejecta at the distance  $D$  is needed, specifically the height  $r_s(D)$  using Equation (4.87). To decide which surface of the asset is hit by the ejecta, the following logic can be used:

- If  $r_s(D) > h_{st}$ , then  $sign(F) = -1$ ,  $r_s = h_{st}$ , and  $D_s = D(v_p, \gamma_p, r_s)$  (hitting the top),
- Else if  $r_s(D) < h_{sb}$ , then  $sign(F) = +1$ ,  $r_s = h_{sb}$ , and  $D_s = D(v_p, \gamma_p, r_s)$  (hitting the bottom),
- Else
  - If  $\gamma_p > \gamma_{p,ap}(r_s(D))$  (Equation (4.69)), then  $sign(F) = -1$ ,  $r_s = r_s(D)$ , and  $D_s = D$  (hitting the side above the local horizon),
  - Else  $sign(F) = +1$ ,  $r_s = r_s(D)$ , and  $D_s = D$  (hitting the side below the local horizon).

For computing both  $F$  and  $D$ , the conditionally defined height  $r_s$  and sign of  $F$  should be used.

Examples of valid ejecta from a crater that hits various asset sizes are shown in Figures 36, 37, and 37 for asset altitudes of  $0r_m$ ,  $0.01r_m$ , and  $0.1r_m$ , respectively. For each figure, the asset properties are ( $a = 0.01r_m$ ,  $h = 0.2r_m$ ) for the left column, ( $a = 0.01r_m$ ,  $h = 0.02r_m$ ) for the center column, and ( $a = 0.1r_m$ ,  $h = 0.02r_m$ ) for

---

<sup>21</sup>A constant probability density in the speed-zenith-azimuth phase space.

the right column. The crater-to-asset distance varies for the rows, where row 1 is  $D = 0.002r_m$ , row 2 is  $D = 0.02r_m$ , row 3 is  $D = 0.2r_m$ , and row 4 is  $D = 2.0r_m$ .

For an asset on the surface of the Moon (Figure 36), there are no ejecta that hit the bottom of the asset – which is to be expected. When a crater is close to the asset (rows 1 and 2 of Figure 36), most of the ejecta hits the asset at the side and occurs for all speeds line-of-site ejecta that are able to reach the bottom edge of the asset.

In general, the further away the crater is from the asset, the more ejecta will hit the top of the asset. For close craters and the higher the asset altitude<sup>22</sup>, the more ejecta will hit the bottom of the asset.

---

<sup>22</sup>Also, for an asset above the surface of the Moon, several sample points need to be chosen at the bottom surface. The higher the asset, the more points that are needed.

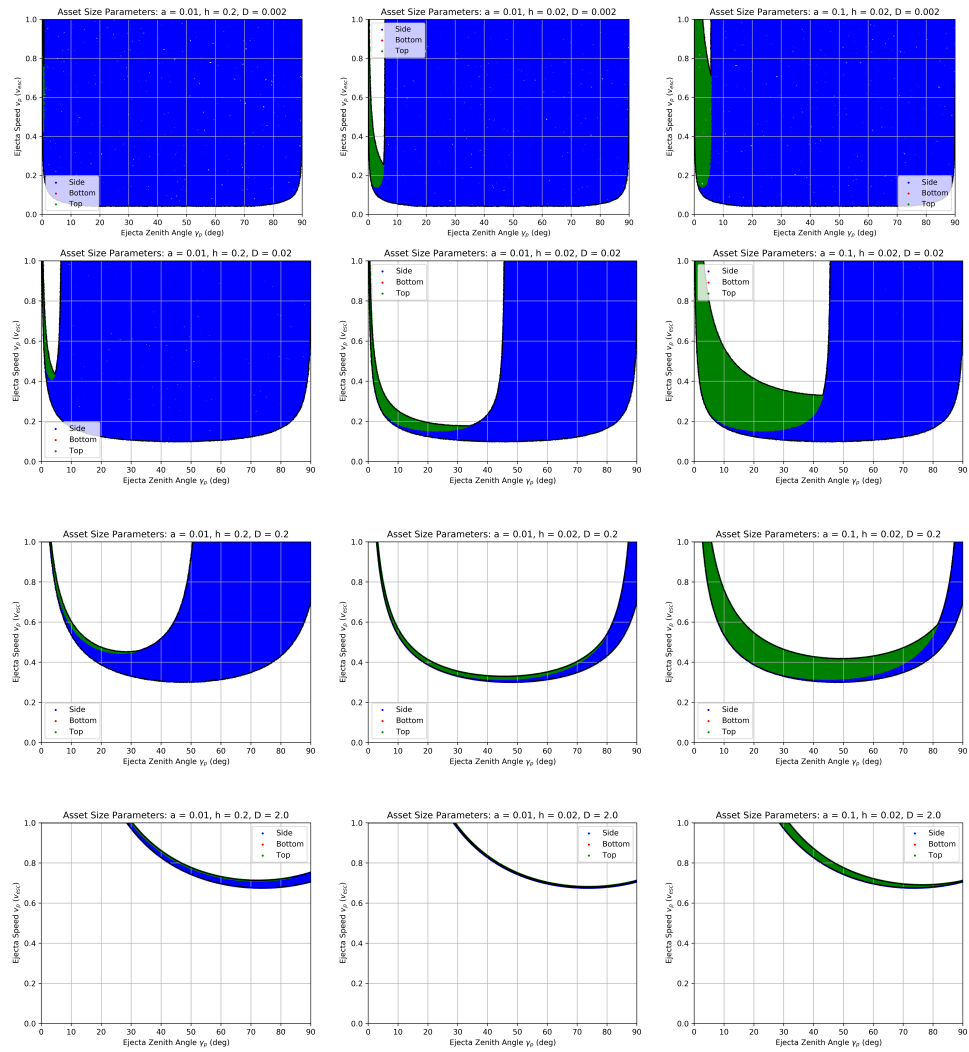


Figure 36: A matrix of plots showing the ejecta hitting a cylindrical asset (in a plane intersecting the cylinder's symmetry axis) on the surface for various asset sizes and crater-to-asset distances. Each plot gives three colors for the ejecta hitting the side (blue), bottom (red), and the top (green) as a function of initial ejecta speed  $v_p$  vs. initial ejecta zenith angle  $\gamma_p$ .

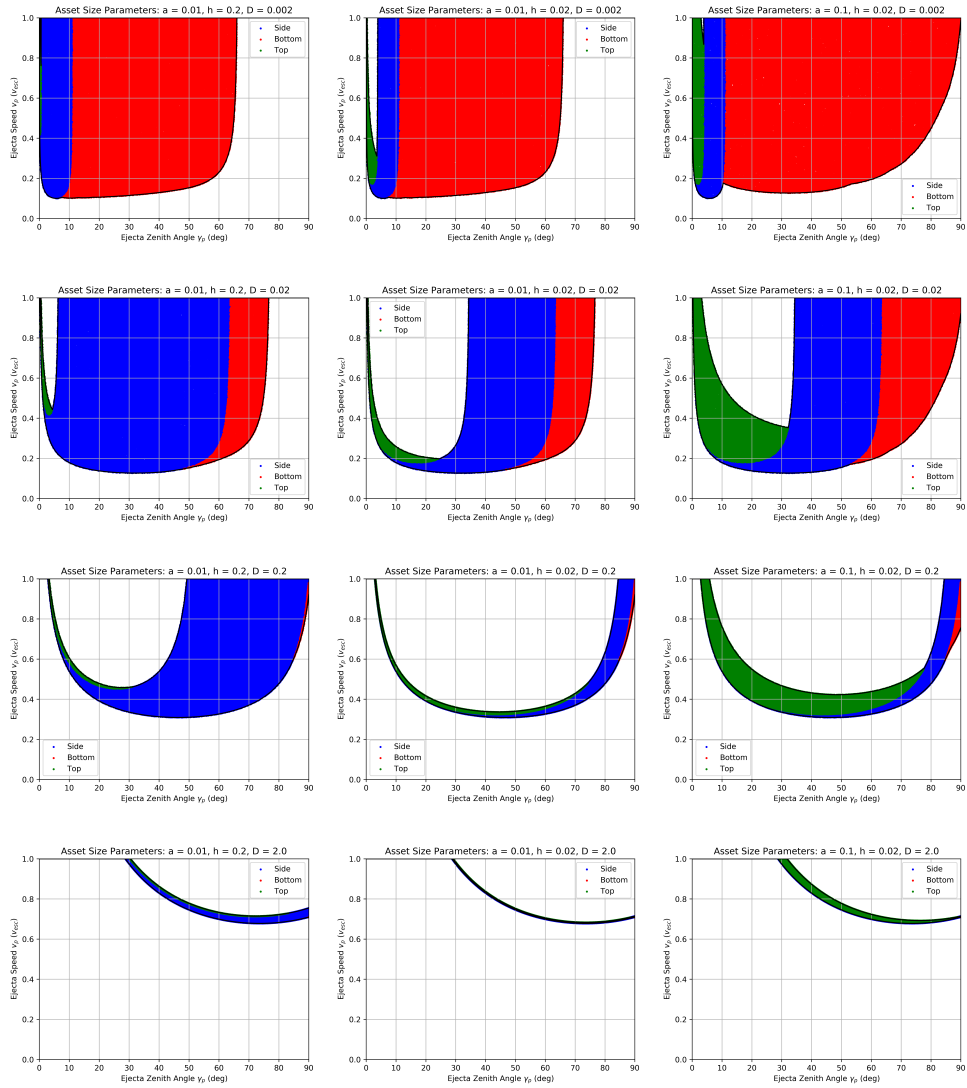


Figure 37: A matrix of plots showing the ejecta hitting a cylindrical asset (in a plane intersecting the cylinder's symmetry axis) with a height above the surface of  $0.01r_m$  for various asset sizes and crater-to-asset distances. Each plot gives three colors for the ejecta hitting the side (blue), bottom (red), and the top (green) as a function of initial ejecta speed  $v_p$  vs. initial ejecta zenith angle  $\gamma_p$ .

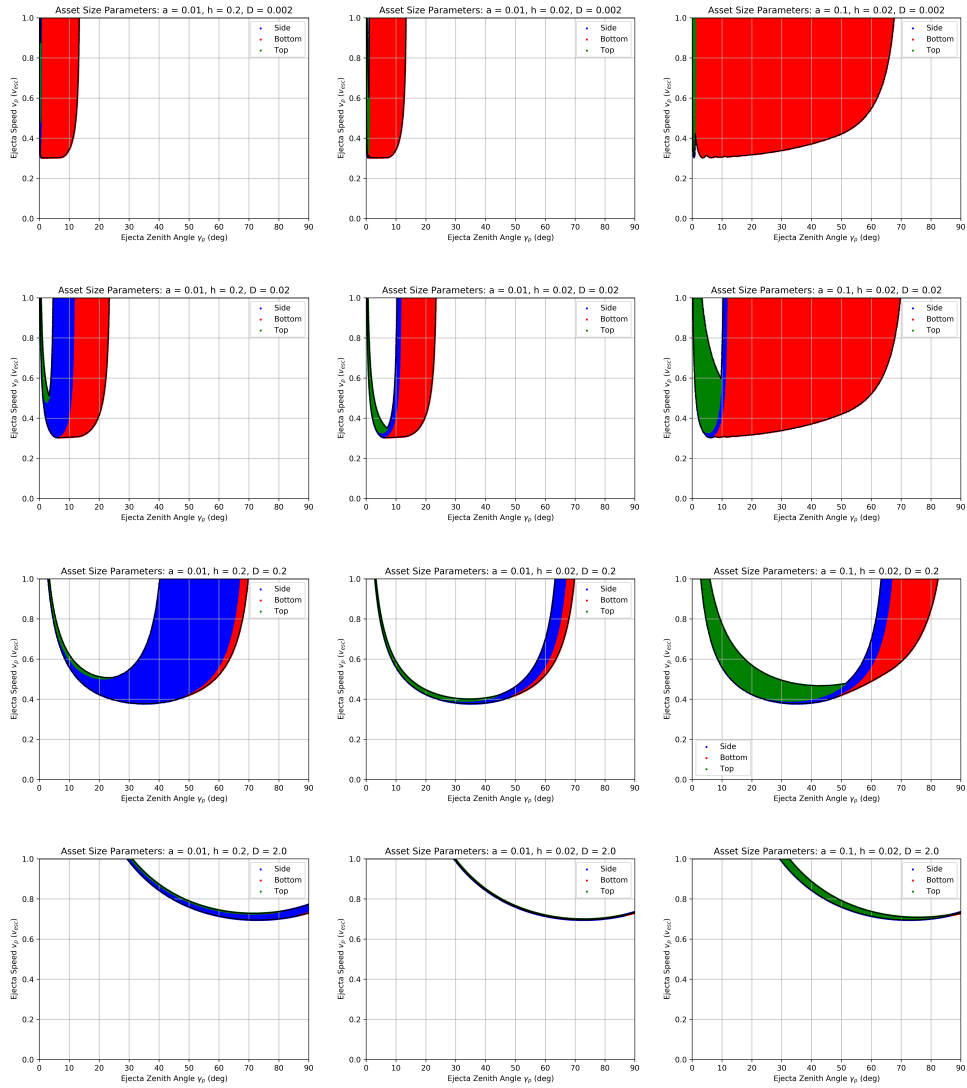


Figure 38: A matrix of plots showing the ejecta hitting a cylindrical asset (in a plane intersecting the cylinder's symmetry axis) with a height above the surface of  $0.1r_m$  for various asset sizes and crater-to-asset distances. Each plot gives three colors for the ejecta hitting the side (blue), bottom (red), and the top (green) as a function of initial ejecta speed  $v_p$  vs. initial ejecta zenith angle  $\gamma_p$ .

## 6.2 Ejecta Speed-Zenith-Azimuth Sampling Algorithm

There are two integration techniques that will be combined in order to sample the ejecta speed-zenith phase space, importance sampling [e.g., Section 9.7 of [Kroese et al., 2011](#)] and stratified sampling [e.g., Section 9.5 of [Kroese et al., 2011](#)].

In general, let  $I$  be the integral given by

$$I = \int g(x)dx. \quad (6.3)$$

Using importance sampling, the integral  $I$  can be approximated as

$$I \sim \frac{1}{n} \sum_{i=1}^n \frac{g(x_i)}{f_{\hat{x}}(x_i)}, \quad (6.4)$$

where  $f_{\hat{x}}(x_i)$  is a probability distribution function close to  $g(x)$ .

The integral  $I$  can also be approximated using stratified sampling as

$$I \sim \sum_{j=1}^{N_1} \frac{\text{vol}(M_j)}{N_{0,j}} \sum_{i=1}^{N_{0,j}} g(x_{ij}), \quad (6.5)$$

where each subdomain  $M_j$  has a volume  $\text{vol}(M_j)$ .

Combining the two integration techniques, the integral  $I$  can be written as

$$I \sim \sum_{j=1}^{N_1} \frac{\text{vol}(M_j)}{N_{0,j}} \sum_{i=1}^{N_{0,j}} \frac{g(x_{ij})}{f_{\hat{x}}(x_{ij})}. \quad (6.6)$$

### 6.2.1 Approximating Ejected Mass Fraction

In the case of computing the fraction of total ejecta  $M$  that hits the asset from a particular crater  $\mathcal{C}$ , the integral  $I$  will be assigned as  $M$  such that

$$M(\mathcal{C}) = \frac{1}{2\pi} \int_{\mathcal{R}(v_p, \gamma_p; \beta_i), \Phi(\beta_i)} d\beta_i d\gamma_p dv \frac{dM(v_p, \gamma_p)}{dv} F(\gamma_p) G(\beta_i - \beta_{imp}), \quad (6.7)$$

where examples of the region  $\mathcal{R}(v_p, \gamma_p; \beta_i)$  are shown in Figures 36, 37, and 38,  $\frac{dM(v_p, \gamma_p)}{dv}$  is the differential of the total ejecta mass (i.e., Equation (5.12)),  $F(\gamma_p)$  is the ejecta zenith distribution (see Section 4.1.2), and  $G(\beta_i - \beta_{imp})$  is the ejecta azimuth distribution (see Section 4.1.3) with  $\beta_{imp}$  as the impactor azimuth.

The speed-zenith subdomain  $M_j$  is broken up into  $d\gamma_{p,j}$  segments, such that the corresponding  $dv_{p,j}$  segments are within a maximum delta sizes, i.e.

$$d\gamma_{p,j} = \gamma_{p,j+1} - \gamma_{p,j} \leq d\gamma_{p,max}, \quad (6.8)$$

$$dv_{p,j} = v_{p,j,max} - v_{p,j,min} \leq dv_{p,max}. \quad (6.9)$$

Two consecutive segments define a trapezoidal area given by four points,  $(\gamma_{p,j}, v_{p,j,min})$ ,  $(\gamma_{p,j}, v_{p,j,max})$ ,  $(\gamma_{p,j+1}, v_{p,j+1,min})$ , and  $(\gamma_{p,j+1}, v_{p,j+1,max})$ , such that the area is given by

$$\text{Area}(M_j) = \frac{1}{2} (dv_{p,j} + dv_{p,j+1}) d\gamma_{p,j}. \quad (6.10)$$

The area  $\text{Area}(M_j)$  also defines where the speed-zenith points will be sampled for the  $j$ -th region. A separate check must be done to make sure that speed-zenith point is valid since there is a linear interpolation done from the  $i$ -th segment to the  $i + 1$ -th segment.

The azimuthal region  $\Phi(\beta_i)$  is defined by  $\beta_{max}$  given in Equation (4.88). The effective height of the cylindrical asset does not change as a function of azimuth. However, the effective radius does, so a sampling weight is introduced to prefer the larger effective radii. A cumulative distribution function  $F_{\hat{\Phi}}$  is generated by the effective radius as a function of crater-to-asset distance  $D_i$ , asset radius  $a_i = c_i/2$ , and azimuth offset from direct line-of-sight from crater to asset  $\beta_i$  (see Figure 31). The corresponding probability distribution function is given by  $f_{\hat{\Phi}}$ , which is used in sampling the azimuth in addition to the weight.

Therefore, the fraction of total ejecta  $M$  can be approximated as

$$M(C) \sim \frac{1}{2\pi N_2} \sum_{k=1}^{N_2} \frac{G(\beta_k - \beta_{imp})}{f_{\hat{\Phi}}(x_k)} \sum_{j=1}^{N_1} \frac{\text{vol}(M_j)}{N_{0,j}} \sum_{i=1}^{N_{0,j}} \frac{\frac{dM(v_{p,ij}, \gamma_{p,ij})}{dv} F(\gamma_{p,ij})}{f_{\hat{\mathcal{R}}}(x_{ij})}. \quad (6.11)$$

The sum over  $i$  handles the samples for a given subdomain of the speed-zenith grid (uniform in  $\mathcal{R}$ ), the sum over  $j$  is for each subdomain of the speed-zenith grid for a given azimuth, and the sum over  $k$  is for each sampled azimuth with a weight of  $f_{\hat{\Phi}}(x_k)$  in  $\Phi(\beta_k)$ . Note that  $x_{ij}$  means a particular sample of the initial speed  $v_{p,i}$  and zenith  $\gamma_{p,j}$ , and  $x_k$  is a particular sample of the initial azimuth  $\beta_k$ .

## 7 Secondary Environment at Asset

### 7.1 Numerical Results

#### 7.1.1 Latitude-Longitude Dependence

#### 7.1.2 Speed Distribution

#### 7.1.3 Angular Distribution

#### 7.1.4 Ejecta Size Distribution

### 7.2 Analytical Results

### 7.3 Benchmark Verification

## References

- Bierhaus, E., A. S. McEwen, S. Robbins, K. Singer, L. Dones, M. Kirchoff, and J.-P. Williams, Secondary craters and ejecta across the solar system: Populations and effects on impact-crater-based chronologies, *Meteoritics & Planetary Science*, 53(4), 638–671, 2018.
- Brown, P., R. Spalding, D. O. ReVelle, E. Tagliaferri, and S. Worden, The flux of small near-earth objects colliding with the earth, *Nature*, 420(6913), 294, 2002.
- Buhl, E., F. Sommer, M. H. Poelchau, G. Dresen, and T. Kenkmann, Ejecta from experimental impact craters: Particle size distribution and fragmentation energy, *Icarus*, 237, 131–142, 2014.
- Carrier, W. D., Lunar soil grain size distribution, *The moon*, 6(3-4), 250–263, 1973.
- Carrier III, W. D., Particle size distribution of lunar soil, *Journal of Geotechnical and Geoenvironmental Engineering*, 129(10), 956–959, 2003.
- Cour-Palais, B. G., Meteoroid environment model 1969 (near earth to lunar surface), nasa sp-8013, *National Aeronautics and Space Administration, Washington, DC*, 1969.
- Gault, D. E., and J. A. Wedekind, Experimental studies of oblique impact, in *Lunar and Planetary Science Conference Proceedings*, vol. 9, pp. 3843–3875, 1978.
- Gault, D. E., E. M. Shoemaker, and H. J. Moore, *NASA TN D-1767 Spray ejected from the lunar surface by meteoroid impact*, National Aeronautics and Space Administration, 1963.
- Grün, E., H. Zook, H. Fechtig, and R. Giese, Collisional balance of the meteoritic complex, *Icarus*, 62(2), 244–272, 1985.
- Hartmann, W. K., Impact experiments: 1. ejecta velocity distributions and related results from regolith targets, *Icarus*, 63(1), 69–98, 1985.
- Heiken, G. H., D. T. Vaniman, and B. M. French, *Lunar Sourcebook, a user's guide to the Moon*, Cambridge University Press, 1991.
- Housen, K. R., and K. A. Holsapple, Ejecta from impact craters, *Icarus*, 211(1), 856–875, 2011.
- Koschny, D., and E. Grün, Impacts into ice–silicate mixtures: Ejecta mass and size distributions, *Icarus*, 154(2), 402–411, 2001.
- Kroese, D. P., T. Taimre, and Z. I. Botev, *Handbook of monte carlo methods*, John Wiley & Sons, 2011.
- Miller, A., Esabase2 debris release 10.0 technical description, *Tech. Rep. 1.7*, ESA, 2017.

- Moorhead, A. V., Osma/meo/lunar-001, *Tech. rep.*, NASA, 2020.
- Moorhead, A. V., A. Kingery, and S. Ehlert, Nasa's meteoroid engineering model 3 and its ability to replicate spacecraft impact rates, *Journal of Spacecraft and Rockets*, pp. 1–17, 2019.
- Moorhead, A. V., W. J. Cooke, and D. E. Moser, The 2021 meteor shower activity forecast for the lunar south pole, *Tech. rep.*, NASA, MEO, 2020.
- O'Keefe, J. D., and T. J. Ahrens, Impact and explosion crater ejecta, fragment size, and velocity, *Icarus*, 62(2), 328–338, 1985.
- Pierazzo, E., and H. Melosh, Understanding oblique impacts from experiments, observations, and modeling, *Annual Review of Earth and Planetary Sciences*, 28(1), 141–167, 2000.
- Rival, M., and J. Mandeville, Modeling of ejecta produced upon hypervelocity impacts, *Space debris*, 1(1), 45–57, 1999.
- Sachse, M., J. Schmidt, S. Kempf, and F. Spahn, Correlation between speed and size for ejecta from hypervelocity impacts, *Journal of Geophysical Research: Planets*, 120(11), 1847–1858, 2015.
- Shuvalov, V., Ejecta deposition after oblique impacts: An influence of impact scale, *Meteoritics & Planetary Science*, 46(11), 1713–1718, 2011.
- Singer, K. N., B. L. Jolliff, and W. B. McKinnon, Lunar secondary craters and estimated ejecta block sizes reveal a scale-dependent fragmentation trend, *Journal of Geophysical Research: Planets*, 125(8), e2019JE006313, 2020.
- Slyuta, E., Physical and mechanical properties of the lunar soil (a review), *Solar System Research*, 48(5), 330–353, 2014.
- Vickery, A., Size-velocity distribution of large ejecta fragments, *Icarus*, 67(2), 224–236, 1986.
- Zook, H. A., The problem of secondary ejecta near the lunar surface., in *Transactions of the 1967 National Symposium on Saturn V/Apollo and Beyond*, vol. I, pp. EN–8, 1967.